



ScuDo
Scuola di Dottorato ~ Doctoral School
WHAT YOU ARE, TAKES YOU FAR



Doctoral Dissertation
Doctoral Program in Physics (32nd cycle)

Dynamical transitions in driven diffusive models

Davide Botto

* * * * *

Supervisors

Prof. Alessandro Pelizzola, Supervisor
Dr. Marco Pretti Co-supervisor

Doctoral Examination Committee:

Prof. A.B., Referee, University of ...
Prof. C.D., Referee, University of ...
Prof. E.F., University of ...
Prof. G.H., University of ...
Prof. I.J., University of ...

Politecnico di Torino
December 23, 2019

This thesis is licensed under a Creative Commons License, Attribution - Noncommercial-NoDerivative Works 4.0 International: see www.creativecommons.org. The text may be reproduced for non-commercial purposes, provided that credit is given to the original author.

Declaration

I hereby declare that, the contents and organisation of this dissertation constitute my own original work and does not compromise in any way the rights of third parties, including those relating to the security of personal data. ¹

.....

Davide Botto
Turin, December 23, 2019

¹This dissertation is presented in partial fulfillment of the requirements for Ph.D. degree in the Graduate School of Politecnico di Torino (ScuDo).

Summary

Driven diffusive models are an attractive research topic for the study of nonequilibrium steady states and for the potential applications to biological and vehicular traffic problems. A reference model in this class is the Totally Asymmetric Simple Exclusion Process (TASEP), for which many exact results have been obtained in the last decades. In this PhD thesis we investigate the relaxation dynamics of two extensions of the TASEP, namely the TASEP with Langmuir kinetics (TASEP-LK) and a TASEP with local interactions called the Antal-Schütz (AS) model. We are mainly interested in studying the dynamical transition, which is characterized by a singularity in the slowest relaxation rate of the system toward the steady state, though not accompanied by any change in the steady state properties. This transition was discovered and exactly located in the phase diagram for the TASEP, it separates one or more *slow* phases, where the relaxation rate depends on a control parameter, from a *fast* phase where the rate reaches a maximum and becomes constant.

Our investigations are based on three different approaches, which provide consistent pictures for both models: the first one corresponds to the mean-field like (cluster) approximations, which reproduce the exact static phase diagram of the TASEP and yield dynamical transition lines in good qualitative agreement with the exact ones. The second method is the modified Domain Wall Theory (mDWT), which is a heuristic correction of the slowest relaxation rate of the DWT in the fast phase and is exact by construction for the TASEP. The last approach consists in computing the exact slowest relaxation rate at finite size and then extrapolating the results to the infinite size limit with the Bulirsch-Stoer (BST) algorithm. It was applied to pure TASEP and gave very accurate results.

As regards the cluster approximations, we develop a mean-field theory for the TASEP-LK with equal (balanced) attachment/detachment rates. This theory predicts the onset of a dynamical transition and allows one to derive analytical bounds for the slowest relaxation rate, becoming tight in the infinite size limit. Then, we extend the analysis to the unbalanced case, where a new type of dynamical transition occurs, showing similarities with first order equilibrium transitions. For the AS model we move to a pair approximation, which reproduces the exact bulk current-density relation and consequently the location of most static transitions. Also this

model exhibits dynamical transitions, moreover two slow phases are observed when the interactions are strongly attractive. We further investigate the full dynamics of the system in the slow and fast phases, showing that the pair approximation is in good agreement with kinetic Monte Carlo simulations. We observe that the whole dynamics is independent of the control parameter in the fast phase.

Acknowledgements

First of all, I would like to sincerely thank my supervisors Profs. Alessandro Pelizzola and Marco Pretti for their guidance, their support and patience during my PhD. They have introduced me to the research topic of this thesis, raising enthusiasm and providing smart intuitions.

I'm also very grateful to Marco Zamparo for making himself available and for the fruitful discussions we had. He is giving important contributions about the mathematical aspects of this research field.

I would also like to acknowledge Federica Gerace, Serena Fazzini and Fabio Lingua for their help and for their friendship. A special thank for the suggestions and the nice time spent together goes also to all the PhD students who have worked with me in the same office during these three years: Andrea, Angelo, Anna, Elisa, Jacopo, Lucrezia, Mirko.

Last, but not least, I'm extremely grateful to my family for always supporting and encouraging me.

Contents

List of Tables	X
List of Figures	XI
Introduction	XIV
I State of the Art and theoretical background	1
1 Driven diffusive models	3
1.1 Asymmetric Simple Exclusion Processes	3
1.2 Steady state and dynamical properties of the TASEP	4
1.3 Possible extensions of the TASEP	7
1.3.1 TASEP with Langmuir kinetics	7
1.3.2 Antal-Schütz model	8
2 Cluster mean-field approximations	13
2.1 Introduction and motivation	13
2.2 Mean-field steady state properties of the TASEP-LK	16
2.2.1 The balanced case	17
2.2.2 The unbalanced case	18
2.3 Pair approximation for the AS model	21
3 The Domain Wall Theory	27
3.0.1 Similarity transformation for Jacobi matrices	30
4 Monte Carlo and numerical techniques	33
4.1 Kinetic Monte Carlo: the Gillespie algorithm	33
4.2 Computing the exact slowest relaxation rate for finite size systems	35
4.3 The Bulirsch-Stoer extrapolation method	36

II	Our contribution	41
5	Dynamical transitions in the TASEP-LK: mean-field approach	43
5.1	Steady state and relaxation in mean-field	43
5.2	The balanced case	45
5.2.1	Properties of steady state density profile	49
5.2.2	Relaxation rates	54
5.3	The unbalanced case	59
5.3.1	New features of the dynamical transition	62
6	Complementary results for the TASEP-LK	69
6.1	mDWT for the TASEP-LK	69
6.2	BST extrapolation for the TASEP-LK	71
7	Dynamical transitions in the AS model	75
7.1	Pair approximation approach to the relaxation	75
7.2	The repulsive case	76
7.3	The attractive case	81
7.4	Full dynamics of the model	85
8	Reflections upon the physical meaning of the dynamical transition	91
8.1	Discussion of methods	91
8.2	Physically relevant aspects	93
	Conclusions and prospects	99
A	Time evolution equations of the marginal cluster probabilities	101
A.1	Pure TASEP	101
A.2	AS model	102
B	Proofs of analytical results in chapter 5	105
B.1	Bounds for the density and current profiles	105
B.1.1	Proof of Theorem 1	106
B.1.2	Proof of Corollary 1	110
B.2	Asymptotic bounds for the slowest relaxation rate (balanced case) .	110
B.2.1	Proof of Corollary 2	110
B.2.2	Proof of Lemma 3	111
B.2.3	Proof of Lemma 5	112
B.2.4	Proof of Lemma 6	113
B.2.5	Proof of Lemma 8	119
B.3	Asymptotic bounds for the slowest relaxation rate (unbalanced case)	120
B.3.1	Upper bounds	120
B.3.2	Lower bounds	122

B.3.3 Proof of statement (B.126)	126
Bibliography	129

List of Tables

8.1	Fit parameters of the components of the eigenvector corresponding to λ_1 (mean-field) for the TASEP. Different α values.	95
-----	---	----

List of Figures

1.1	Static (a) and dynamical (b) phase diagrams of the TASEP.	5
1.2	Exact slowest relaxation rate of the TASEP as a function of α for $\beta = 0.2$	7
1.3	Repulsive case $\eta = 0.1$ and $\theta = 1$. Bulk current-density relation (a) and static phase diagram (b).	10
1.4	Attractive case $\eta = 1$ and $\theta = 0.1$. Bulk current-density relation (a) and static phase diagram (b).	11
2.1	Exact and mean-field density profiles for the TASEP. HD (a) and MC (b) phases.	14
2.2	Phase diagram of the TASEP with mean-field and exact dynamical transition lines.	15
2.3	First eigenvalues of the mean-field relaxation matrix of the TASEP. $N = 100$, $\beta = 0.2$	15
2.4	Phase diagram of the TASEP-LK balanced.	19
2.5	Density and current profiles of the TASEP-LK balanced in the LD-HD coexistence region.	19
2.6	Density and current profiles of the TASEP-LK balanced in the LD-MC-HD coexistence region.	20
2.7	Phase diagram of the TASEP-LK unbalanced.	20
2.8	Density and current profiles of the TASEP-LK unbalanced in the MC phase.	21
2.9	Density profile of the TASEP-LK unbalanced in the HD phase: numerical and analytical results.	22
2.10	Density profile of the AS model in the fourth phase: pair approximation and kinetic Monte Carlo results.	25
3.1	Schematic illustration of a domain wall.	27
3.2	Modified Domain Wall Theory solution for the TASEP.	30
5.1	Phase diagram of the TASEP-LK balanced with the mean-field dynamical transition lines.	45
5.2	Plots of the function $f(x; \alpha, q_0)$ as a function of the variable x at different α values.	47

5.3	Difference between the finite-size slowest relaxation rate and its infinite-size limit as a function of N for the TASEP.	49
5.4	Difference between the finite-size slowest relaxation rate and its infinite-size limit as a function of N for the TASEP-LK balanced.	50
5.5	Density profiles of TASEP-LK and pure TASEP, with β adjusted in order to have the same boundary layer: mean-field	51
5.6	Density profiles of TASEP-LK and pure TASEP, with β adjusted in order to have the same boundary layer: KMC simulations	52
5.7	Smallest eigenvalues of the relaxation matrix of the TASEP-LK unbalanced at low betas.	62
5.8	Smallest eigenvalues of the relaxation matrix of the TASEP-LK unbalanced at high betas.	63
5.9	Eigenvector corresponding to λ_1 for the TASEP-LK unbalanced at high betas: slow and fast phases.	64
5.10	HD phase region for the TASEP-LK unbalanced.	65
5.11	Difference between the finite-size slowest relaxation rate and its infinite-size limit as a function of N for the TASEP-LK unbalanced: low betas.	67
5.12	Difference between the finite-size slowest relaxation rate and its infinite-size limit as a function of N for the TASEP-LK unbalanced: high betas.	67
6.1	Density profile at two different times close to the steady state for the TASEP-LK, $\Omega_A = 0.4$, $\Omega_D = 0.1$, $\alpha = 0.3$, $\beta = 0.1$. Mean-field and KMC simulations results	70
6.2	Example of the slowest relaxation rate given by the mDWT for the TASEP-LK. Top curve: $\beta < 1 - l$, bottom curve: $\beta > 1 - l$	71
6.3	Stability of the BST extrapolation of a finite size sequence with scaling exponents σ greater or smaller than one.	72
6.4	Example picture of numerical evidences explained in the text. Solid line: ξ_N as a function of $\hat{\lambda}^{(\infty)}$, dashed line: pole in the last extrapolant.	73
6.5	Comparison between mDWT and BST results as a function of α for the slowest relaxation rate of the TASEP-LK. Top curve: $\beta < 1 - l$, bottom curve: $\beta > 1 - l$	74
6.6	Comparison between mDWT and BST results as a function of β in the fast phase.	74
7.1	Low lying part $(\lambda_1, \dots, \lambda_9)$ of the spectrum of the pair approximation relaxation matrix.	76
7.2	Phase diagram of the AS model for strong repulsive interactions.	77
7.3	Slowest relaxation rates (three methods) of the AS model as a function of ρ_L for $\eta = 0.8$, $\theta = 1$	78
7.4	Slowest relaxation rates (three methods) of the AS model for $\eta = 0.5$, $\theta = 1$	78

7.5	Slowest relaxation rates (three methods) of the AS model for $\eta = 0.1, \theta = 1$.	79
7.6	Slowest relaxation rates (three methods) of the AS model as a function of η/θ in the slow phase.	80
7.7	Slowest relaxation rates (three methods) of the AS model as a function of η/θ in the fast phase.	80
7.8	Steady state current as a function of ρ'_R (a) and slowest relaxation rate as a function of the current (b). Strongly repulsive case.	81
7.9	Slowest relaxation rates (three methods) as a function of ρ'_R . Strongly repulsive (a) and weakly repulsive (b) cases.	81
7.10	Phase diagram of the AS model in the weakly attractive case.	82
7.11	Slowest relaxation rates (three methods) as a function of ρ_L for $\eta = 1, \theta = 0.5$.	82
7.12	Portion of the phase diagram of the AS model for strongly attractive interactions.	83
7.13	Slowest relaxation rates (three methods) as a function of ρ_R' in the strongly attractive case.	84
7.14	Last extrapolant of λ_1 as a function of σ .	84
7.15	Last extrapolant of λ_1 as a function of ρ_L for the TASEP.	85
7.16	Last extrapolant of λ_1 as a function of ρ_R' .	86
7.17	Full dynamics of the density profile in the slow phase.	87
7.18	Full dynamics of the density profile in the fast phase.	87
7.19	Full dynamics of the current profile in the fast phase.	88
7.20	Full dynamics of the density profile in the fast phase for strongly repulsive interactions and small values of ρ_R' .	89
8.1	Dynamics of the density profile for the TASEP-LK in the slow phase.	94
8.2	Components of the eigenvector corresponding to λ_1 (mean-field) for the TASEP after dividing by the exponential decay.	95
8.3	Eigenvector corresponding to λ_1 of the symmetric relaxation matrix for the TASEP.	96
8.4	Components of the eigenvector corresponding to λ_1 (pair approximation) for the AS model	97
8.5	Eigenvector corresponding to λ_1 (densities) for the AS model after dividing by the exponential decay.	97

Introduction

Driven lattice gases are inspired by molecular transport processes and vehicular traffic, but they are introduced also to study nonequilibrium steady states, which lack a well founded theory as that developed for equilibrium ones. In this research line of nonequilibrium statistical physics, the Asymmetric Simple Exclusion Processes (ASEPs) have become paradigmatic models because of the availability of many exact results obtained in the last decades about both the static and dynamical properties. In fact, a dynamical phase transition, i.e. a transition in the relaxation dynamics to the steady state, was discovered and exactly located in the phase diagram for some models in this class. This transition does not coincide with any change in the steady state properties and is pointed out by a singularity in the slowest relaxation rate of the system.

The purpose of this PhD thesis is to investigate the dynamical transitions in two models derived from the ASEPs class, namely the Totally Asymmetric Simple Exclusion Process with Langmuir kinetics (TASEP-LK) and the Antal-Schütz (AS) model, for which a complete exact solution is not available. For this reason, we tackle the problem with different analytical and numerical methods: cluster mean-field approximations, the modified Domain Wall Theory (mDWT), kinetic Monte Carlo simulations and the Bulirsch-Stoer (BST) extrapolation of exact finite size results.

The thesis is organized as follows: in the first part, corresponding to chapters 1-4, we provide a review of the state of the art on driven diffusive models and on the analytical and numerical tools adopted in our research activity. The second part (chs. 5-8) is devoted to our contribution. We briefly outline below the content of each single chapter:

- Chapter 1 introduces the ASEPs, then it reviews the steady state properties of the TASEP and explains what the slowest relaxation rate and the dynamical transition are. Finally, it introduces the two generalisations of the TASEP that have been investigated in this thesis: the TASEP-LK and the AS model.
- Chapter 2 motivates the application of cluster mean-field like approximations, in particular the ordinary mean-field and the pair approximation, to driven diffusive models, based on known results for the TASEP. Then, it introduces

the mean-field theory for the TASEP-LK and the pair approximation for the AS model, summarizing the steady state properties.

- Chapter 3 describes the Domain Wall Theory (DWT) and provides a derivation of the slowest relaxation rate within this approach. Finally, it introduces the modified Domain Wall Theory (mDWT), which is exact by construction for the TASEP.
- In Chapter 4 we give an overview of the numerical methods employed in this thesis, namely the kinetic Monte Carlo, the computation of the exact finite size slowest relaxation rate and the Bulirsch-Stoer (BST) extrapolation method.
- Chapter 5 presents our results about the dynamical transitions in the TASEP-LK within a mean-field approximation. It contains a formal derivation of asymptotic bounds for the slowest relaxation rate in the infinite size limit.
- Chapter 6 contains complementary results about the dynamical transitions in the TASEP-LK, obtained by the mDWT and the BST extrapolation of exact finite size results. In this chapter we make two conjectures, supported by numerical evidences, respectively about the exactness of the mDWT for the TASEP-LK and about the scaling exponent of the slowest relaxation rate.
- Chapter 7 presents our results about the dynamical transitions in the AS model, obtained by three methods: the pair approximation, the mDWT and the BST extrapolation.
- Chapter 8 is a sum up of the work done in the thesis. The first part contains a discussion of the approach and the techniques adopted in this thesis, compared to previous results about the TASEP dynamical transition. The second one restates the properties of the dynamical transition that are relevant for achieving a physical understanding of this phenomenon and gives some additional observations supported by numerical evidences.

Summary of the main results of the thesis

A general result of the thesis is the evidence of a robustness of the dynamical transition, which does not show a strong dependence on the specific driven diffusive model under consideration. In addition, we are going to see that new features of this phenomenon emerge in the two models studied in this work. While for the TASEP the slowest relaxation rate is discontinuous in the second derivative at the dynamical transition, a new kind of transition, characterized by a discontinuity in the first derivative of the slowest relaxation rate, occurs in a portion of the dynamical phase diagram for the TASEP-LK with different attachment/detachment rates.

Another new behaviour is observed in the AS model, where the slowest relaxation rate undergoes two transitions under strongly attractive interactions.

Since a complete exact solution is not available for these two extensions of the TASEP, an important aspect of this work is that we tackle the problem with different approaches. One method is given by cluster mean-field like approximations (mean-field and pair), that have been applied to the TASEP in [1]: in the following chapters we are going to see that these techniques allow to extract the significant physical properties of driven diffusive models, concerning both the steady state and the relaxation dynamics. Then, we adopt and extend two other methods, that are the mDWT and the BST extrapolation of exact finite size results: the first is a heuristic strategy based on the Domain Wall Theory [2] that is exact by construction for pure TASEP, the second is an efficient algorithm to extrapolate sequences of finite size results to the thermodynamic limit. The latter approach was applied in [3] to determine the slowest relaxation rate of pure TASEP and gave very accurate results. The relevant point is that the results for the long time dynamical behaviour of both models obtained by these approaches are consistent.

A last remark about the main results is that we have observed some common properties which may contribute to giving a physical interpretation of the dynamical transition, left as an open problem in [4]. In particular, we understood that the dynamical transition is characterized by the competition between two different relaxation modes, driven respectively by the boundary layer (slow phase) and by the system bulk properties (fast phase). Then, we observed that the slow phases are located close to coexistence regions in the phase diagram: this aspect, together with the study of the full relaxation dynamics, allows to make a loose analogy between the slow phases and the metastability regions in equilibrium phase diagrams. Moreover, within the cluster approximations, we observed a change in the structure of the eigenvector corresponding to the mean-field/pair approximation slowest relaxation rate at the dynamical transition.

Part I

State of the Art and theoretical background

Chapter 1

Driven diffusive models

1.1 Asymmetric Simple Exclusion Processes

Driven diffusive models are an active research topic in nonequilibrium statistical physics and, among them, a paradigmatic role is played by the Asymmetric Simple Exclusion Processes (ASEPs), which are inspired by biological and vehicular traffic phenomena. The reference model, also called Partially Asymmetric Simple Exclusion Process (PASEP, see [2]), consists of a one dimensional lattice: each node can be occupied by at most one particle and particles jump to empty nearest-neighbours on the two sides with different rates. When the hopping is completely biased in one direction, the model is called Totally Asymmetric Simple Exclusion Process (TASEP): in the next section we concentrate on this particular case.

In a system with open boundaries, where particles are injected and extracted with given rates, the behaviour of the bulk of the system at stationarity depends strongly on these boundary rates and characterizes the phase diagram of the model. Many steady state properties of this class of models, such as the phase diagrams and the stationary density profiles, are known exactly (see [5, 6, 7, 8]).

Another important aspect is the study of the relaxation dynamics to the steady-state: a *dynamical* transition, corresponding to a singularity in the relaxation rate and not coinciding with any change in the steady state properties, was discovered for the pure TASEP and exactly located in the phase diagram by de Gier and Essler in [9]. In this work, they determined the asymptotic behaviour in the infinite size limit of the slowest relaxation rate (called *gap* by the authors), which determines the behaviour of the model at long times, close to the steady state. Then, these results have been generalized to the partially asymmetric case in [2]. In general terms, the dynamical transition separates a region of the phase diagram where the relaxation rate depends only on the parameter fixing the steady state bulk density from one or more regions where the rate depends also on another control parameter. For the ASEPs, these parameters are the injection/extraction rate. We remark that this transition is purely dynamical, because it does not coincide with any change

in the steady state properties; in the next section we describe it in more detail for the TASEP.

Given the exact results concerning both the steady state and the relaxation, the ASEP's have become paradigmatic models in the investigation of one dimensional transport.

Two important references on driven diffusive models are [10] and [11]. The former is an instructive review on ASEP's in the context of nonequilibrium statistical physics, their mathematical properties and the possible generalizations to model biological transport. The latter is a book which starts from the same framework and focuses on models for vehicular traffic.

1.2 Steady state and dynamical properties of the TASEP

The TASEP was proposed in the sixties (see [12]) as a model for mRNA translation. In this case, particles can hop only in one direction from an occupied node to the adjacent one with unit rate, if the latter is empty. We label lattice nodes from left to right by $n = 1, \dots, N$ and we introduce the occupation numbers $\nu_n^t \in \{0,1\}$, where $\nu_n^t = 1$ if node n is occupied by a particle at time t and $\nu_n^t = 0$ if it is empty. Considering $k + 1$ consecutive nodes, we denote by $P_n^t[\nu_n \nu_{n+1} \dots \nu_{n+k}]$ the probability that, at time t , the occupation numbers of nodes from n to $n + k$ take values ν_n, \dots, ν_{n+k} respectively. The occupation probability of the site n at time t (the local density) is denoted by $p_n(t) = P_n^t[1] = \langle \nu_n^t \rangle$, steady state local densities are time-independent and are denoted by p_n . The probability current $J_n(t)$ from node n to $n + 1$ coincides with the joint probability $P_n^t[10]$ of having the former site occupied and the latter empty, because of the unitary hopping rate.

In the system with open boundaries, particles are injected at site 1 with rate ρ_L , if this is empty, and are extracted at site N with rate $1 - \rho_R$, if the latter is occupied. One can equivalently consider a system in contact with two reservoirs of fixed densities that inject and extract particles with rate one, thus we introduce two auxiliary nodes $n = 0$, $n = N + 1$ and write

$$p_0 = \rho_L, \tag{1.1}$$

$$p_{N+1} = \rho_R. \tag{1.2}$$

We now open a parenthesis on notation: in the literature on TASEP, the injection rate is usually denoted by α , whereas the extraction rate by β . We choose to adopt the notation with left and right boundary densities for conformity with the AS model, presented in section 1.3.2. Thus, concerning the TASEP and the TASEP with Langmuir kinetics described below, one has that $\rho_L = \alpha$ and $\rho_R = 1 - \beta \equiv \beta'$. Here we also introduce the notation $x' \equiv 1 - x$, that will be used in the following

to write more compact formulae.

The TASEP has an important property concerning the steady state distribution:

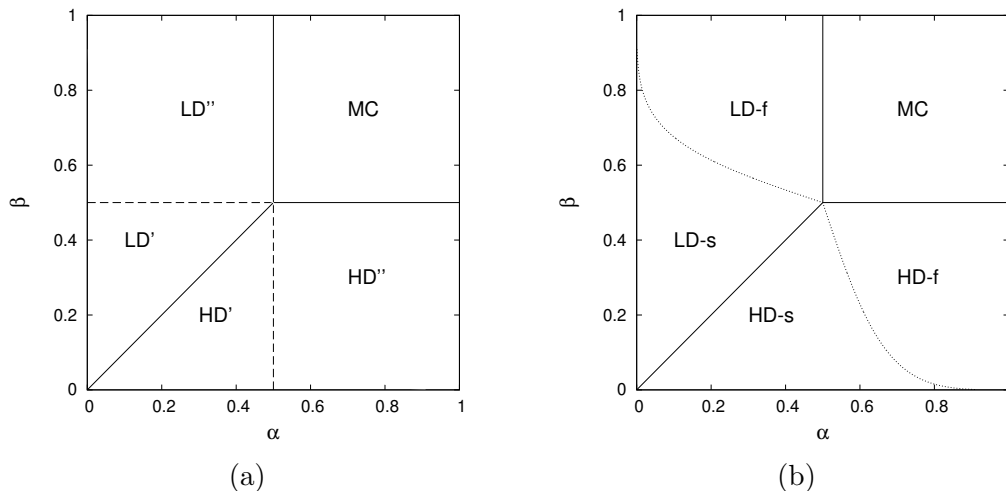


Figure 1.1: Static (a) and dynamical (b) phase diagrams of the TASEP. The static transitions are denoted by thick solid lines. The static phases are the high-density (HD), characterized by bulk density $q = \beta'$ and current $J = \beta\beta'$, the low-density (LD), with $q = \alpha$ and $J = \alpha\alpha'$, and the maximal current (MC), where $q = 1/2$ and $J = 1/4$. The letters “s” and “f” denote respectively the slow and the fast dynamical phases. Thick dashed lines at $\alpha = 1/2$ and $\beta = 1/2$ correspond to subphase boundaries: they separate a region (HD'/LD') in which the approach of the density profile to the bulk value is purely exponential, from one (LD''/HD'') characterized by an additional power-law correction. The dynamical transition lines are denoted by thin dotted lines.

for periodic boundary conditions and in the open boundary case with $\alpha = \beta'$, the stationary distribution is equivalent to the equilibrium distribution of a non-interacting lattice gas. We give a sketch of the proof of this property at the end of this chapter, considering a generalization of the TASEP (see section 1.3.2), for which the equivalent equilibrium distribution is that of a one dimensional Ising model with nearest-neighbours interactions.

The steady state of the system with open boundaries was solved exactly in the 1990s (see [5] and references therein). The static phase diagram, reported in figure 1.1a, consists of three regions (phases), characterized by the value of the uniform current and by the bulk density, which is the limiting value of the local density far from the boundaries: the high-density (HD), the low-density (LD) and the maximal current (MC) phases. The high-density phase occurs for $\beta < 1/2$ and $\alpha > \beta$, the current is equal to $J = \beta\beta'$ and the bulk density $q = \beta' > 1/2$ extends up to the right boundary. From the injection side, the density approaches its bulk value with an exponential decay (HD' region), which has additional power law

corrections for $\alpha \geq 1/2$ (HD" region). Since the latter transition, indicated by a dashed line in figure 1.1a, involves a finite portion of the system, it is called *subphase* transition. The TASEP is symmetric under the particle-hole transformation $\alpha \leftrightarrow \beta$ and $\nu_n' \leftrightarrow \nu_{N+1-n}$, thus the LD phase is closely related to the HD one: for $\alpha < 1/2$ and $\beta > \alpha$, the current is $J = \alpha\alpha'$ and the bulk density $q = \alpha < 1/2$ extends to the left boundary, whereas, on the right side, the density approaches its bulk value exponentially (LD' region) with power-law corrections for $\beta \geq 1/2$ (LD" region). These two phases coexist along the line $0 < \alpha = \beta < 1/2$, where the densities α and $1 - \alpha$ are connected by a linear profile. The MC phase is characterized by $J = 1/4$ and $q = 1/2$, the approach to the bulk value from both sides is power law. These transitions can be called *static*, as they affect the steady state properties. As mentioned before, the dynamical transition in the TASEP was studied exactly by De Gier and Essler [9, 13, 2] and then observed numerically by Proeme et al. in [4]. The slowest relaxation rate can be defined as follows. We denote by $x = \{\nu_1^t, \dots, \nu_N^t\}$ a configuration of the lattice at time t , the system can jump from this state to a different one y with rate $\mathcal{W}_{x \rightarrow y}$. The probability $P^t[x]$ of having at time t a given configuration x of the lattice nodes satisfies the master equation

$$\dot{P}^t[y] = \sum_x W_{y,x} P^t[x], \quad (1.3)$$

where $W_{y,x}$ are the elements of the transition matrix, defined as [14]

$$\mathbf{W} = \begin{cases} W_{y,x} = \mathcal{W}_{x \rightarrow y}, & x \neq y \\ W_{x,x} = -\sum_{z \neq x} \mathcal{W}_{x \rightarrow z}. \end{cases} \quad (1.4)$$

The slowest relaxation rate (or spectral gap) is the largest nonzero eigenvalue of the transition matrix. Since the nonzero eigenvalues have negative real parts and the largest one is real, its inverse changed of sign is the longest relaxation time. De Gier and Essler employed the Bethe ansatz to diagonalize the transition matrix of a PASEP with open boundary conditions, for arbitrary values of hopping and injection/extraction rates. Then, for the special case of the TASEP, they determined the asymptotic behaviour of the slowest relaxation rate in the infinite size limit. The functional form of this quantity characterizes the phases of the dynamical phase diagram shown in figure 1.1b. In the regions corresponding to the LD and the HD phases, the spectral gap remains finite in the $N \rightarrow \infty$ limit. This implies a finite correlation length and an exponential relaxation to the steady state. These regions are further divided in subphases, that can be called *slow* (HD-s, LD-s) and *fast* (HD-f, LD-f) for reasons that will be clear below, by the dynamical transition lines (denoted by thin dotted lines in figure 1.1b), corresponding to a singularity in the slowest relaxation rate. Considering the HD phase, for each value of β there is a critical value of the injection rate

$$\alpha_c(\beta) = \left[1 + \left(\frac{\beta}{\beta'} \right)^{1/3} \right]^{-1}, \quad (1.5)$$

such that for $\alpha > \alpha_c(\beta)$ the gap is independent of α . For $\alpha < \alpha_c(\beta)$, it depends on both α and β . The gap vanishes along the LD-HD coexistence line as a power law of the inverse of the system size with exponent 2 and in the whole MC phase with exponent $3/2$. Despite being exactly located in the phase diagram, the dynamical transition was not completely understood from the physical point of view, which was left as an open question in [9].

From now on, we change of sign the transition or, in the following, the approximate relaxation matrix and we study the smallest nonzero eigenvalue. In figure 1.2 we show the exact gap of the TASEP as a function of α for $\beta = 0.2$, this example clarifies the choice of the adjectives *slow* and *fast* for the two regimes: for $\alpha < \alpha_c(\beta)$, the relaxation rate depends on the injection rate and is increasing. At $\alpha_c(\beta)$ the gap reaches a maximum and becomes independent of this control parameter.

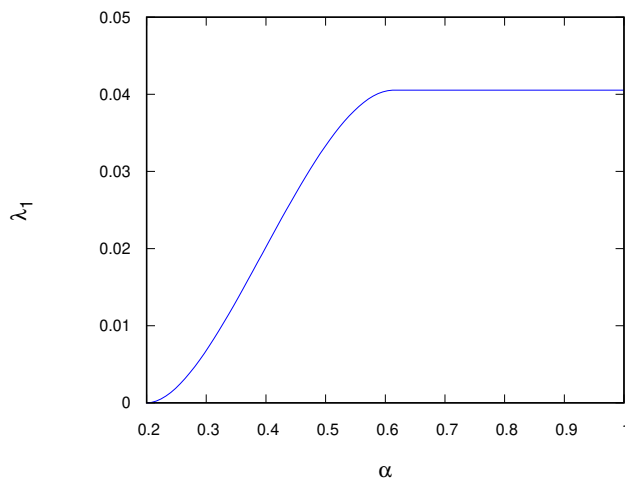


Figure 1.2: Exact slowest relaxation rate λ_1 of the TASEP as a function of α for $\beta = 0.2$. The critical injection rate is $\alpha_c(\beta) \simeq 0.6135$.

1.3 Possible extensions of the TASEP

1.3.1 TASEP with Langmuir kinetics

The TASEP with Langmuir kinetics (TASEP-LK) is a generalization of the TASEP in which particles can also bind to an empty node or unbind from an occupied one at given rates. We denote the local attachment/detachment rates by ω_A and ω_D respectively: in order to establish a competition between the hopping process and the Langmuir kinetics in the large N limit, they have to scale as the

inverse of the size. In the following, we will use the definitions

$$\omega_A \equiv \frac{\Omega_A}{N+1}, \quad \omega_D \equiv \frac{\Omega_D}{N+1},$$

where $\Omega_{A,D}$ are the global attachment/detachment rates, which are fixed. This is a physically interesting case, in which particles can remain on the lattice long enough to visit a finite fraction of it and give a collective behaviour [15]. The dynamical rules of the TASEP-LK in the bulk of the lattice (sites $n = 2, \dots, N-1$) do not conserve the number of particles, as a consequence the steady state current is no longer uniform.

This model was first introduced in [16] as a simplified description of a specific financial market, but it finds applications also in other very different contexts, such as biophysics and vehicular traffic modelling (see [17, 15] and references therein). In the original formulation, the Langmuir kinetics concerns the sites $n = 2, \dots, N-1$, in our investigation we include also the sites 1 and N : this does not alter the physics of the model, since we are adding to the injection and extraction rates a quantity that goes to zero for $N \rightarrow \infty$.

An exact solution is not available for the TASEP-LK, whose steady state phase diagram has been studied at a mean-field level [17, 15], supporting the results with Monte Carlo simulations. Such mean-field results are described in section 2.2, discussing separately the balanced case ($\omega_A = \omega_D = \omega$) and the unbalanced one. Then, in chapter 5, we present our investigation of the dynamical transition.

1.3.2 Antal-Schütz model

As previously mentioned, a possible application of driven lattice gases with open boundaries is to model the traffic flow of cars on a road segment between two junctions. In order to build a more realistic model for this purpose, Antal and Schütz proposed in [18] a TASEP in which the hopping rate depends on the occupation state of the next-nearest neighbour node in the direction of motion, yielding short-range interactions. If the site n is occupied and the site $n+1$ is empty, the possible transitions are

$$101 \rightarrow 011 \quad \text{with rate } \eta, \tag{1.6}$$

$$100 \rightarrow 010 \quad \text{with rate } \theta. \tag{1.7}$$

Thus, the probability current from node n to node $n+1$ at time t can be written as

$$\begin{aligned} J_n^t &= \left\langle \nu_n^t \nu_{n+1}^t \left[\eta \nu_{n+2}^t + \theta \nu_{n+2}^t \right] \right\rangle \\ &= \eta P_n^t[101] + \theta P_n^t[100], \quad n = 1, \dots, N-2. \end{aligned} \tag{1.8}$$

When $\eta < \theta$ the interaction is repulsive, whereas the case $\eta > \theta$ corresponds to an attractive interaction. The TASEP dynamics is obtained in the special case

$\eta = \theta = 1$. Actually this model is a particular case of a class of driven diffusive systems previously introduced by Katz, Lebowitz and Spohn (KLS) in [19] and shares with several of them the property of equivalence of the steady state distribution with the equilibrium one for a 1D Ising model with nearest neighbours interactions mentioned above (section 1.2), generalizing that of pure TASEP. In this case, the problem with open boundaries requires a particular choice, called *bulk-adapted* and explained in the following, of the injection and extraction rates, with $\rho_L = \rho_R = q$ as before. Under this hypothesis, the exact bulk current-density relation is given by

$$J(q) = \theta q \left[1 + \frac{\sqrt{1 - 4qq'(1 - \frac{\eta}{\theta})} - 1}{2q'(1 - \frac{\eta}{\theta})} \right]. \quad (1.9)$$

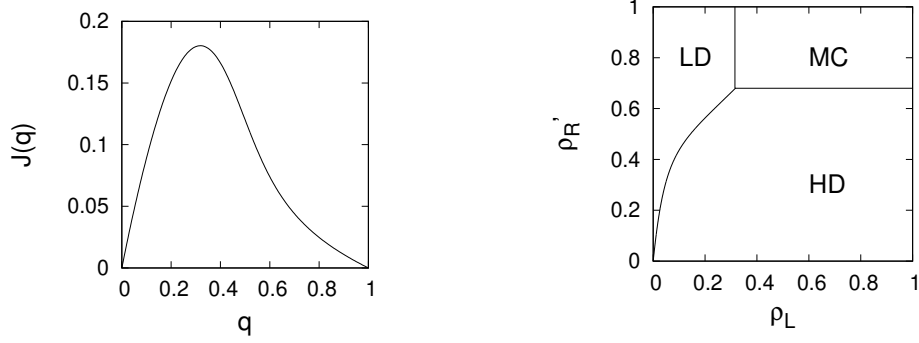
In this case, defining the boundary conditions for an open system requires some more care. One can consider the coupling of a semi-infinite lattice at site 1 with a reservoir of fixed density $q = \rho_L$: in general, the interaction of the particles with the boundary is different from the interactions that they have among themselves in the bulk, this gives rise to a boundary layer starting at ρ_L and approaching an effective boundary density $q = \rho_-$. Such boundary layer is non-universal, because it depends on the coupling mechanism and on the kind of particle interaction. The same argument holds for an effective boundary density ρ_+ , when coupling a semi-infinite lattice at site N with a reservoir of constant density $q = \rho_R$. Thus, the bulk behaviour of the system in the steady state is determined by ρ_- and ρ_+ . The bulk-adapted rates are defined in such a way that they would satisfy $\rho_L = \rho_-$ and $\rho_R = \rho_+$ for a semi-infinite system, as a consequence the relations between correlators and densities at the boundaries are the same as in the bulk. Here we give their expression in terms of the current-density relation (1.9) (see [18]), then, in the next chapter, we reobtain these results within the pair approximation. At the left boundary, the injection rate depends on the occupation of node 2: α_1 (respectively α_2) is the injection rate when the latter node is occupied (respectively empty). Imposing the condition of a uniform density $q = \rho_L$ for a semi-infinite system $n = 1, 2, \dots, \infty$ in the steady state, they are defined as

$$\alpha_1 = \eta \left[1 - \frac{J(\rho_L)}{\theta \rho_L} \right], \quad \alpha_2 = \theta \left[1 - \frac{J(\rho_L)}{\theta \rho_L} \right]. \quad (1.10)$$

At the right boundary, the hopping from site $N - 1$ and the extraction from site N need to be specified, the corresponding rates are denoted by β_1 and β_2 respectively. Imposing again the condition that a uniform density $q = \rho_R$ is obtained in the steady state of a semi-infinite lattice $n = -\infty, \dots, N - 1, N$, the boundary rates are given by

$$\beta_1 = \frac{J(\rho_R)}{\rho_R'} \left[1 - \frac{J(\rho_R)}{\theta \rho_R} \right]^{-1}, \quad \beta_2 = \frac{J(\rho_R)}{\rho_R}. \quad (1.11)$$

With this choice for the boundary conditions, the exact static phase diagram of the model is predicted by the theory of boundary induced phase transitions (see [20]). At fixed values of η and θ , the parameters of the phase diagram are ρ_L and ρ_R' ; figure 1.3 (b) shows an example for the repulsive case ($\eta = 0.1$ and $\theta = 1$),

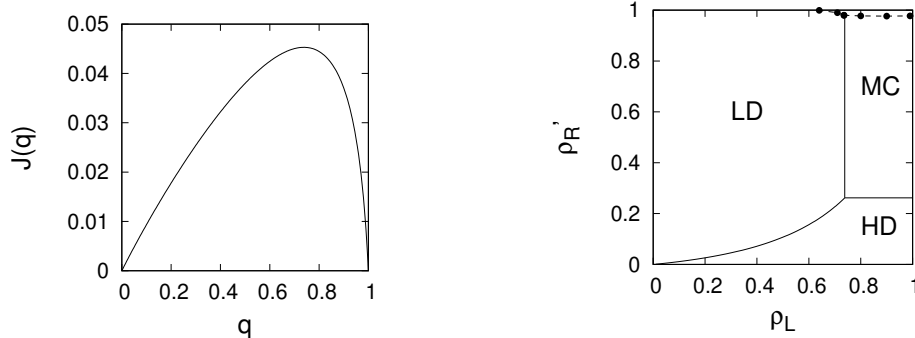


(a) Bulk current-density relation (1.9).

(b) Static phase diagram.

Figure 1.3: AS model, repulsive case $\eta = 0.1$ and $\theta = 1$.

the corresponding current-density function is reported on the left. As for pure TASEP, the phase diagram of the AS model consists of the HD, LD and MC phase regions. In the LD phase the steady state has a bulk density equal to ρ_L extending to the left with a boundary layer on the right side, whereas in the HD phase the bulk density ρ_R extends to the right with a boundary layer on the left. The coexistence line separating the low and the high density phases is given by the condition $J(\rho_L) = J(\rho_R)$, the bulk density profile jumps discontinuously from ρ_L to ρ_R . The transition between the LD and the HD phases predicted by driven diffusive models reproduces an experimental finding in [21] from an analysis of traffic data collected on a German highway: considering a section where the number of lanes is reduced, the transition between the free flow and the congested traffic regimes is signalled by a sudden decrease in the average velocity (and thus an increase in the local density), while the flow of cars (the current) remains practically constant. The MC phase is characterized by the bulk density q^* , corresponding to the maximum in the current-density plot, with boundary layers at both ends. The transitions to this phase from the LD and the HD phases are continuous in the bulk density and are given by the conditions $\rho_L = q^*$ and $\rho_R = q^*$ respectively. In the presence of strongly attractive interactions, i.e. for η sufficiently larger than θ , Antal and Schütz predicted the appearance of a fourth phase in the region at large ρ_L and ρ_R close to zero. This phenomenon was observed within a mean-field approximation of the model and was then confirmed by Monte Carlo simulations. The stationary density profile of this phase has a central bulk region with two boundary layers as the maximal current one, however the bulk density is not equal to any of the



(a) Bulk current-density relation (1.9).

(b) Static phase diagram.

Figure 1.4: AS model, attractive case $\eta = 1$ and $\theta = 0.1$. The boundaries of the HD^{IV} phase were determined by kinetic Monte Carlo simulations (see 4.1).

boundary densities, it is independent of ρ_L and depends on ρ_R as in the HD phase (for this reason, we will denote the fourth phase by HD^{IV}). The transition (called *reentrant* by the authors) to this phase is discontinuous from the LD phase and continuous from the MC one.

In the next chapter (see section 2.3) we shall see a suitable approximation for this model, that reproduces the bulk current-density relation (1.9) and the location of most static phase transitions. Then, in chapter 7 we shall present our research contribution about the existence of dynamical transitions in this model.

We note that recently dynamical transitions have been observed for a 1D KLS model in [22].

We conclude this section with a derivation [23] of the property mentioned above about the steady state distribution of several models in the KLS class (including the TASEP as a particular case), focusing on the AS model. The (dimensionless) Hamiltonian of the lattice gas is given by

$$H(x) = V \sum_n \nu_n \nu_{n+1}, \quad (1.12)$$

where V is the nearest-neighbour interaction: $V > 0$ (respectively $V < 0$) for repulsive (resp. attractive) interactions. We denote the hopping rates by $\Gamma(\nu_{n+2})$: if they satisfy the relation

$$\Gamma(1) = \Gamma(0)e^{-V}, \quad (1.13)$$

the steady state distribution of the system is equivalent to the equilibrium Boltzmann distribution for a lattice gas with the above Hamiltonian.

Recalling the master equation (1.3), for this process the transition rates can be written as

$$\mathcal{W}_{x \rightarrow y} = \sum_n \nu_n \nu_{n+1} \delta_{y,x(n,n+1)} \Gamma(\nu_{n+2}), \quad (1.14)$$

where the configuration $x^{(n,n+1)}$ has the occupations ν_n and ν_{n+1} interchanged and all the others equal. Substituting (1.14) into the master equation, in the steady state one obtains

$$0 = \sum_n \left[\nu'_n \nu_{n+1} P[x^{(n,n+1)}] - \nu_n \nu'_{n+1} P[x] \right] \Gamma(\nu_{n+2}). \quad (1.15)$$

Using the hypothesis $P[x] \propto \exp[-H(x)]$, it is possible to write

$$\frac{P[x^{(n,n+1)}]}{P[x]} = \exp[-V(\nu_{n+1} - \nu_n)(\nu_{n-1} - \nu_{n+2})]. \quad (1.16)$$

Plugging this into the master equation, one gets

$$0 = \sum_n \left[\nu'_n \nu_{n+1} e^{-V(\nu_{n+1} - \nu_n)(\nu_{n-1} - \nu_{n+2})} - \nu_n \nu'_{n+1} \right] \Gamma(\nu_{n+2}). \quad (1.17)$$

Now we introduce the frequencies for the possible sequences of the occupation numbers $\{\nu_{n-1}, \nu_n, \nu_{n+1}, \nu_{n+2}\}$: for example, the frequency of the sequence $\{0,0,1,0\}$ is $F_{0010} = \sum_n \nu'_{n-1} \nu'_n \nu_{n+1} \nu'_{n+2}$. The equation (1.17) becomes

$$\begin{aligned} 0 = & \left[F_{0010} - F_{0100} \right] \Gamma(0) + \left[F_{1010} e^{-V} - F_{1100} \right] \Gamma(0) + \\ & + \left[F_{0011} e^V - F_{0101} \right] \Gamma(1) + \left[F_{1011} - F_{1101} \right] \Gamma(1). \end{aligned} \quad (1.18)$$

Using the identity $\nu'_n \equiv 1 - \nu_n$, one can express the eight frequencies in terms of six irreducible quantities: $F_{11} = \sum_n \nu_{n-1} \nu_n$, $F_{1_{-}1} = \sum_n \nu_{n-1} \nu_{n+1}$, $F_{111} = \sum_n \nu_{n-1} \nu_n \nu_{n+1}$, $F_{1_{-}11} = \sum_n \nu_{n-1} \nu_{n+1} \nu_{n+2}$, $F_{11_{-}1} = \sum_n \nu_{n-1} \nu_n \nu_{n+2}$ and $F_{1111} = \sum_n \nu_{n-1} \nu_n \nu_{n+1} \nu_{n+2}$. Rewriting the square brackets in (1.18) and collecting the terms corresponding to each irreducible frequency, one arrives at

$$\begin{aligned} 0 = & F_{11} [\Gamma(0) - e^V \Gamma(1)] + F_{1_{-}1} [\Gamma(1) - e^{-V} \Gamma(0)] + \\ & + (F_{111} + F_{11_{-}1}) [e^{-V} \Gamma(0) + e^V \Gamma(1) - \Gamma(0) - \Gamma(1)] + \\ & + F_{1111} [\Gamma(0) - e^{-V} \Gamma(0) + \Gamma(1) - e^V \Gamma(1)]. \end{aligned} \quad (1.19)$$

We observe that this equation is satisfied for all configurations x if the rates obey to eq. (1.13). This condition holds for the AS model, where $e^{-V} = \eta/\theta = \Gamma(1)/\Gamma(0)$.

Chapter 2

Cluster mean-field approximations

2.1 Introduction and motivation

The basic idea of the cluster mean-field like approximations is to express the probability distribution of a lattice model as a suitable product of local marginals. We motivate this assumption with an application to the TASEP: we consider a cluster of $k + 1$ consecutive nodes and use the same notation introduced in 1.2 for the probability associated to the occupation numbers at time t . At the boundaries we introduce two auxiliary nodes acting as reservoirs and we assume that

$$P_0^t[1\nu_1 \dots \nu_n] \equiv \alpha P_1^t[\nu_1 \dots \nu_n], \quad (2.1)$$

$$P_n^t[\nu_n \dots \nu_N 0] \equiv \beta P_n^t[\nu_n \dots \nu_N], \quad n = 1, \dots, N. \quad (2.2)$$

One can write exact time evolution equations for the probability marginals. For single site clusters one obtains

$$\dot{P}_n^t[1] = \dot{p}_n(t) = P_{n-1}^t[10] - P_n^t[10] = J_{n-1}(t) - J_n(t), \quad n = 1, \dots, N, \quad (2.3)$$

where $P_n^t[10] \equiv J_n^t$ as already mentioned. The evolution of the latter two-node probabilities depends on three-node marginals (see the end of this section)

$$\dot{P}_n^t[10] = P_{n-1}^t[100] + P_n^t[110] - P_n^t[10], \quad n = 1, \dots, N - 1. \quad (2.4)$$

Proceeding in this way, an infinite hierarchy of equations depending at each step on larger cluster marginals is obtained. The cluster approximations are introduced to close this set of equations. The simplest approximation is the mean-field one and corresponds to completely neglecting the correlations between adjacent nodes

$$P_n^t[\nu_n \nu_{n+1}] = P_n^t[\nu_n] P_{n+1}^t[\nu_{n+1}]. \quad (2.5)$$

Apart from the subphase boundaries, the mean-field approximation of the TASEP

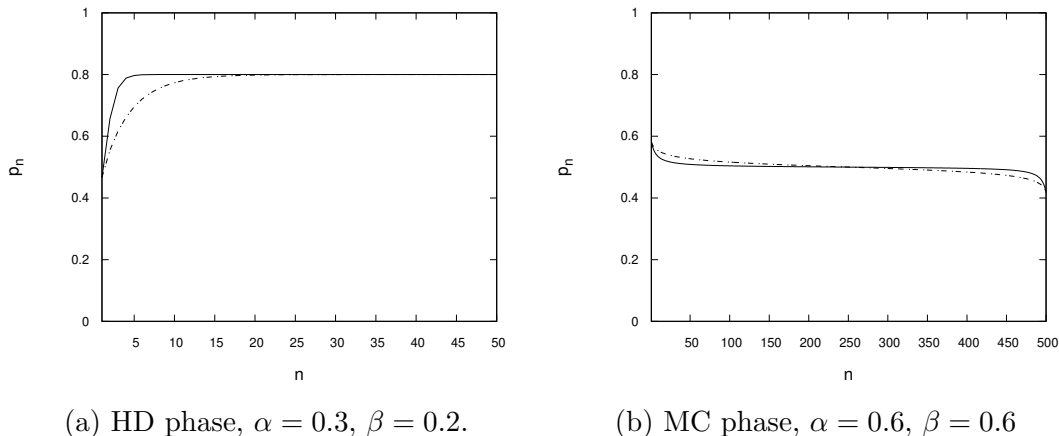


Figure 2.1: Exact (dash-dotted line) and mean-field (solid line) density profiles for the TASEP.

reproduces the exact static phase diagram [5]. In figure 2.1 we show the mean-field profile, denoted by a solid line, together with the exact one (dashed dotted line) in the HD ($\alpha = 0.3$, $\beta = 0.2$) and in the MC phase ($\alpha = 0.6$, $\beta = 0.6$): one can see that the approximation reproduces the correct bulk value. Moreover, recently in [1] it was shown that this approximation gives a dynamical transition line in good qualitative agreement with the exact one. In figure 2.2 we show the approximate dynamical transition line together with the exact one in the TASEP phase diagram. The mean-field theory for the TASEP reveals also a qualitative change in the spectrum of the relaxation matrix at the dynamical transition. In the fast phase ($\alpha > \alpha_c(\beta)$), the eigenvalues seem to tend to a continuous band in the infinite size limit. The smallest eigenvalue λ_1 , which corresponds to the relevant relaxation mode when the system approaches the steady state, is constant and joins the band in the fast phase, whereas it detaches from the rest of the spectrum in the slow phase. We report an example of the bottom part of the spectrum of the mean-field relaxation matrix in figure 2.3, for a lattice of $N = 100$ nodes and at $\beta = 0.2$.

A more accurate approximation can be obtained by taking into account the correlations between adjacent nodes, assuming that, at any time t , the marginals with three or more sites factor as

$$P_n^t[\nu_n \nu_{n+1} \dots \nu_{n+k-1}] = \frac{\prod_{l=n}^{n+k-2} P_l^t[\nu_l \nu_{l+1}]}{\prod_{l=n+1}^{n+k-2} P_l^t[\nu_l]}. \quad (2.6)$$

This approximation is exact for the 1D Ising model at equilibrium (see [24] and references therein), thus, recalling the property explained in section 1.3.2, it reproduces the location of most static phase transitions for a system with bulk-adapted

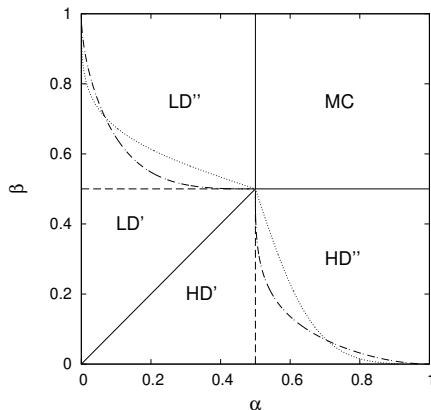


Figure 2.2: Phase diagram of the TASEP. The exact dynamical transition is indicated by the dotted line in the HD'' and LD'' regions, the dash-dotted line corresponds to the mean-field one.

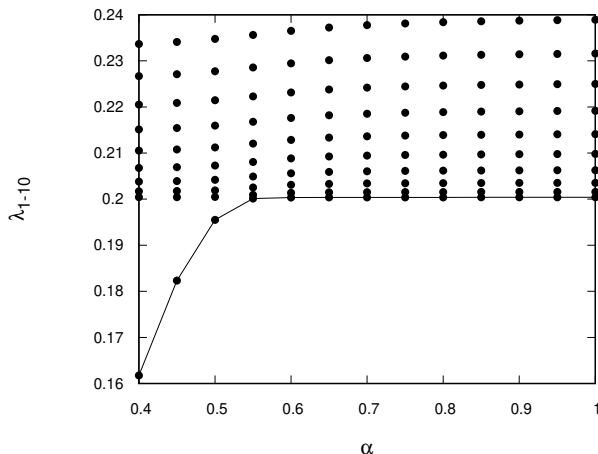


Figure 2.3: The first 10 eigenvalues of the mean-field relaxation matrix of the TASEP as a function of α , for $N = 100$ and $\beta = 0.2$. The line connecting the values of λ_1 is a guide for the eye.

boundary rates.

Focusing on one-dimensional systems, the authors of the work in [25] discuss a class of (n, m) cluster approximation methods, where n is the cluster size and m the degree of overlap, and observe that the $(n, n - 1)$ case is the most accurate one. The pair approximation corresponds to the $(2, 1)$ scheme of this work.

In the second part of the thesis we present how these two approximate methods have been used to investigate the dynamical transitions in the TASEP-LK and in the AS model.

We conclude this section observing that an easy way to write the dynamical equations for the marginal cluster probabilities consists in writing all the possible transitions leading to the desired configuration and departing from it. As an example, with reference to the time evolution equations for the local currents (2.4), the transitions leading to the configuration with node n occupied and node $n + 1$ empty are $(\nu_{n-1} = 1, \nu_n = 0, \nu_{n+1} = 0) \rightarrow (\nu_{n-1} = 0, \nu_n = 1, \nu_{n+1} = 0)$ and $(\nu_n = 1, \nu_{n+1} = 1, \nu_{n+2} = 0) \rightarrow (\nu_n = 1, \nu_{n+1} = 0, \nu_{n+2} = 1)$, then the system can depart from this configuration if the particle on site n jumps to the adjacent one. In appendix A we show in detail the derivation of the same result from the master equation and we generalize it for the AS model.

In this chapter we describe the cluster approximations for the TASEP-LK and the AS model. The former model has no interactions apart from hard core exclusions (no more than one particle on each site), thus the ordinary mean-field theory is accurate. The latter model exhibits correlations in the steady state, thus we adopt the pair approximation, which, under the choice mentioned in section 1.3.2 for the boundary conditions, reproduces the exact bulk current-density relation and consequently the location of almost all static transitions.

2.2 Mean-field steady state properties of the TASEP-LK

The static phase diagram of the TASEP-LK has been investigated at a mean-field level in [15] by Parmeggiani, Franosch and Frey, who claim its exactness on the basis of Monte Carlo simulations, as was proven for pure TASEP. Using the notation introduced in 1.2, we describe the mean-field theory for the model. The time evolution equations for the local densities are given by

$$\dot{p}_n(t) = J_{n-1}(t) - J_n(t) + \omega_A p'_n(t) - \omega_D p_n(t), \quad n = 1, \dots, N. \quad (2.7)$$

Introducing the mean-field approximation and recalling the boundary conditions (1.1) and (1.2), one has the following current-density relation

$$J_n(t) \equiv p_n(t) p'_{n+1}(t), \quad n = 0, \dots, N. \quad (2.8)$$

In the steady state, the equations (2.7) with the assumption (2.8) can be written in the form

$$p_n (p_{n+1}' + \omega_D) = (p_{n-1} + \omega_A) p_n', \quad n = 1, \dots, N. \quad (2.9)$$

In section 5.1 we shall see that the latter equations can be solved by expressing them in a fixed-point scheme and that they admit a unique solution in which all the local densities are strictly between zero and one (see [26] for the details of the derivation). We give a remark on the *bulk solution*: in [15], this is the solution

of a first order differential equation in the hydrodynamic limit, but it has also an important physical meaning, because it is related to the behaviour of the current in the system, which is not influenced by the boundary layers. Thus, the bulk profile intervenes both in the static and in the dynamical phase transitions.

In the following, we describe the mean-field steady state properties of the model in the balanced ($\omega_A = \omega_D$) and the unbalanced ($\omega_A \neq \omega_D$) cases separately. We note that the particle-hole symmetry for the TASEP-LK is modified taking into account that also the attachment of a particle can be viewed as the detachment of a vacancy and viceversa, thus the model is symmetric under the transformation $\alpha \leftrightarrow \beta$, $\nu_n' \leftrightarrow \nu_{N+1-n}$ (which at the mean-field level becomes $p_n' \leftrightarrow p_{N+1-n}$) and $\omega_A \leftrightarrow \omega_D$. For this reason, the discussion of the unbalanced version can be restricted to the case $\omega_A > \omega_D$. In this context, we introduce the density of the Langmuir isotherm, which will appear frequently in the steady state and then in the dynamical properties of the model: it is the value of the density reached at the equilibrium condition between the attachment and the detachment of particles in the Langmuir kinetics

$$l = \frac{\Omega_A}{\Omega_A + \Omega_D}. \quad (2.10)$$

The name comes from the equation proposed by Irving Langmuir to describe the variation at fixed temperature in the adsorption of gaseous molecules on a surface with active sites as a function of the pressure. In the following we will call it Langmuir density.

2.2.1 The balanced case

In figure 2.4 we show the static phase diagram for $\Omega = (N + 1)\omega = 0.2$ (recall that ω scales as the inverse of the size, so that Ω is of order 1). The main new feature with respect to the phase diagram of the pure TASEP is the presence of parameter regions where the pure phases (HD, LD, MC) coexist and in one case (LD-HD region) they are separated by a stable and localized domain wall. This entails a shrinking of the HD and LD pure-phase regions: the pure HD phase is defined by the following inequalities on the model parameters

$$1/2 > \Omega \geq 0, \quad (2.11)$$

$$1/2 - \Omega > \beta > 0, \quad (2.12)$$

$$\alpha > \beta + \Omega. \quad (2.13)$$

In the large N limit, the density profile is almost completely described by a bulk solution being a linear function of the node index n with slope ω and satisfying the right-boundary condition (1.2). Unless one chooses $\alpha = (\beta + \Omega)'$, resulting in a completely linear profile, the mismatch with the left-boundary condition (1.1) gives rise to a *boundary layer*, such that the local density approaches exponentially the

bulk solution, with the characteristic length of the exponential remaining finite as N grows to infinity. Even if the bulk density is no longer constant as it was for the TASEP, the HD phase is again characterized by bulk values greater than $1/2$. The current profile has its maximum value at the left boundary and is strictly decreasing. In section 5.2.1 we present a formal derivation of the mean-field solution for the density and current profiles in the HD phase. The LD phase is delimited by analogous inequalities obtained by exchanging α with β ¹, the density profile has a linear bulk with slope ω matching the left boundary condition and a boundary layer on the right. In the MC phase, the profile has a central bulk with density $1/2$ and two boundary layers. In the balanced case, the Langmuir density coincides with the maximal current one.

We note that pure HD and LD phases exist only if $\Omega < 1/2$ and their displacement with respect to the pure TASEP ones can be obtained by the mapping $\beta \mapsto \beta + \Omega$ (for the HD) and $\alpha \mapsto \alpha + \Omega$ (for the LD). In chapter 5 we will see that such a mapping plays a central role in the change of several properties from the pure TASEP to the symmetric TASEP-LK. The LD and the HD phases are separated from each other and from the MC one by two-phase coexistence regions (LD-HD, LD-MC, HD-MC), which are in turn contiguous to a three-phase coexistence area (LD-MC-HD). In the density profile of the LD-HD coexistence region, one observes a domain wall that connects the low and the high density bulk solutions, we show an example in figure 2.5a. This corresponds to a kink in the current profile (figure 2.5b): the strict monotonicity of the latter profile entails the localization of the domain wall. The coexistences with the MC phase are characterized by the presence of a region of density $1/2$, which is connected to the bulk profile of the coexisting phase (figure 2.6a) without discontinuities. Across all the transition lines, the density profile evolves continuously from one phase to the other.

2.2.2 The unbalanced case

In figure 2.7 we show the static phase diagram for $\Omega_A = 0.2$ and $\Omega_D = 0.1$. As mentioned before for the particle-hole transformation, it is no more symmetric with respect to the line $\beta = \alpha$. Between the LD phase on the left side and the HD and MC phases on the right side, there are two-phase coexistence regions, where the coexisting phases are separated by a stable and localized domain wall in the steady state: the coexistence is between the low- and the high density phases for $\beta < 1/2$, between the low-density and the maximal current phases for $\beta \geq 1/2$, the transition is denoted by a dotted line. Increasing Ω_A , the pure LD phase progressively disappears.

In the HD (respectively in the LD) phase, the bulk density profile depends only

¹In this case $\omega_A = \omega_D$, so that the model symmetry is the same as that of pure TASEP.

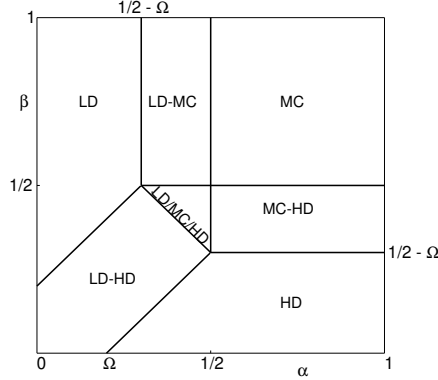
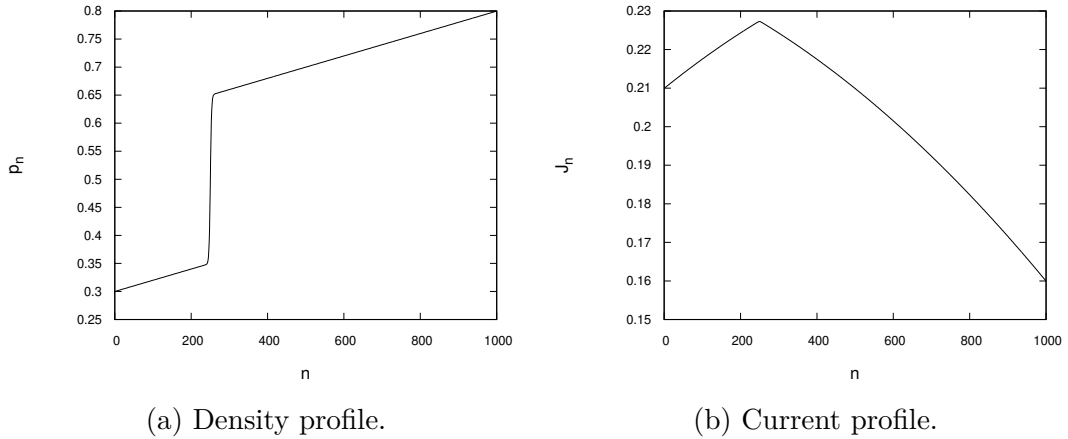


Figure 2.4: Static phase diagram of the TASEP-LK in the balanced case ($\Omega = 0.2$). The pure phases are separated by coexistence regions (LD-HD, LD-MC, MC-HD and LD/MC/HD).



(a) Density profile.

(b) Current profile.

Figure 2.5: LD-HD coexistence region for the TASEP-LK balanced, $\alpha = 0.3$, $\beta = 0.2$, $\Omega = 0.2$.

on the extraction (respectively the injection) rate and extends to the right (resp. left) boundary. The bulk profile of the MC phase is independent of α and β . At odds with the pure TASEP and the balanced case of the TASEP-LK, it is no more uniform: the density reaches the value $1/2$ (and the current the maximum value $1/4$) at the right boundary (see figures 2.8a, 2.8b). This profile evolves continuously into the HD one for $\beta < 1/2$, the transition is denoted by a dashed line in figure 2.7. The right borders of the coexistence regions, indicated by a solid line, are given by those values of α for which the domain wall reaches the left end of the system, leaving the steady state in the HD or in the MC phase, depending on the value of the extraction rate. If one decreases α starting from the coexistence regions, the

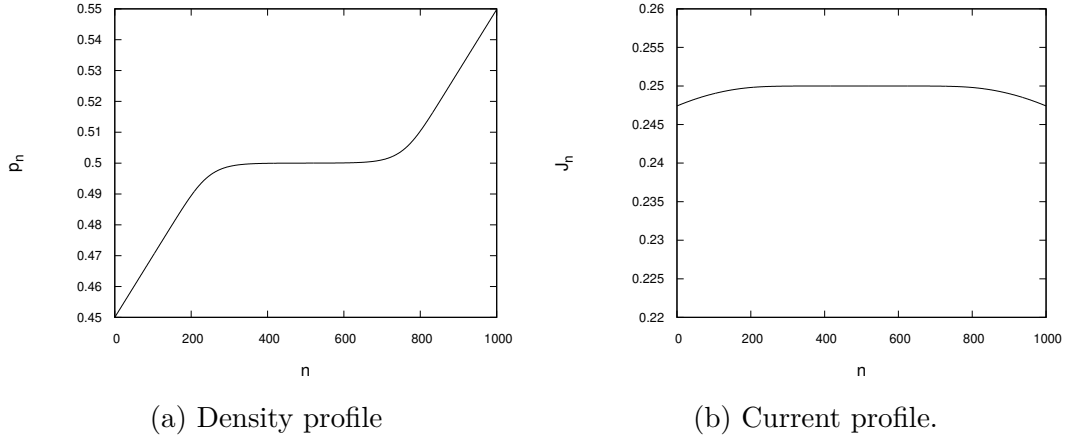
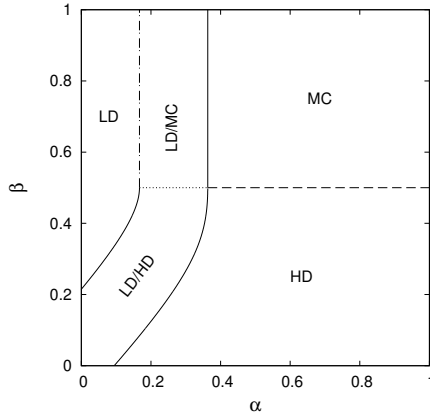

 Figure 2.6: Three-phases coexistence region, $\alpha = 0.45, \beta = 0.45, \Omega = 0.2$.


Figure 2.7: Phase diagram of the TASEP-LK in the unbalanced case ($\Omega_A = 0.2$ and $\Omega_D = 0.1$). The two-phases coexistence regions LD/HD and LD/MC are delimited by a dotted line at $\beta = 1/2$, the borders with the LD phase are given by the α values such that the domain wall separating the coexisting phases reaches the right boundary: the domain wall amplitude decreases with increasing β and vanishes while reaching the right end of the system for $\beta \geq 1/2$, the transition is denoted by a dashed dotted line. The dashed line at $\beta = 1/2$ denotes a continuous transition in the density profile between the HD and MC phase regions.

domain wall moves to the right and leaves the steady state in the LD when arriving at the boundary. Moving along this transition line, it was observed that the domain wall amplitude decreases with increasing β and vanishes continuously at $\beta = 1/2$. For greater values of the extraction rate, the domain wall amplitude vanishes while reaching the right boundary, the transition is denoted by a dash-dotted line.

Focusing on the high-density phase, the stationary profile approaches the bulk

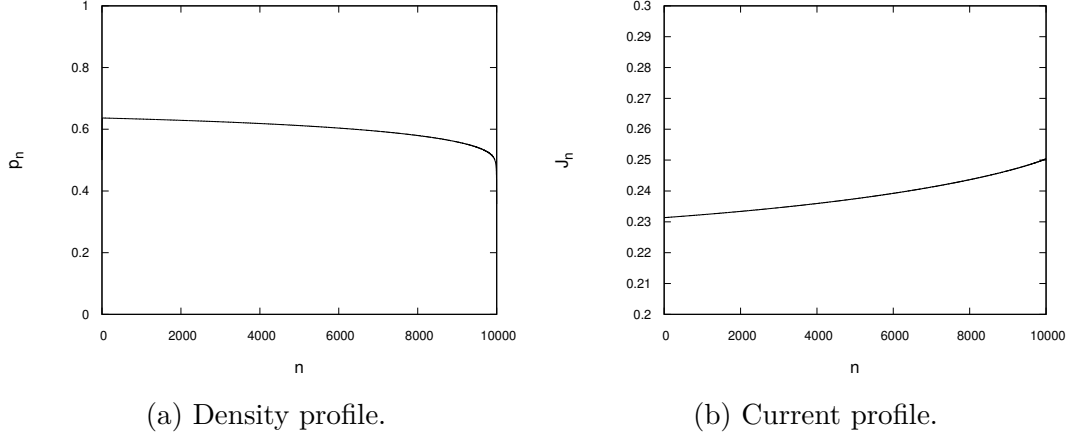


Figure 2.8: MC phase for the TASEP-LK unbalanced, $\alpha = 0.5$, $\beta = 0.7$, $\Omega_A = 0.2$, $\Omega_D = 0.1$.

exponentially and can be computed by solving numerically the mean-field equations (2.9) with the boundary conditions (1.1) and (1.2). There exists also an analytical expression for the bulk profile in terms of the real 0-branch of the Lambert W function [27], which is valid in the $N \rightarrow \infty$ limit; for this case we do not have an analytical form for the bulk density profile at finite size. However, as one can see from figure 2.9, this expression is accurate even for rather small N . One can observe that for $\beta' > l$, the bulk profile is completely above the Langmuir density and increasing, whereas for $\beta' < l$ it is all below l and decreasing. For $\beta' = l$ this profile is constant on the value of the Langmuir density. The details on the analytic solution for the asymptotic bulk density profile are given in chapter 5.

2.3 Pair approximation for the AS model

To develop the pair approximation for the AS model, one can express the two-node marginal $P_n^t[\nu_n \nu_{n+1}]$, $n = 1, \dots, N-1$ in terms of three parameters: we choose the two local densities $p_n(t)$, $p_{n+1}(t)$ and the pair probability $C_n(t) = P_n^t[10]$, the remaining two-node marginals are

$$P_n^t[00] = 1 - p_{n+1}(t) - C_n(t), \quad (2.14)$$

$$P_n^t[01] = p_{n+1}(t) - p_n(t) + C_n(t), \quad (2.15)$$

$$P_n^t[11] = p_n(t) - C_n(t). \quad (2.16)$$

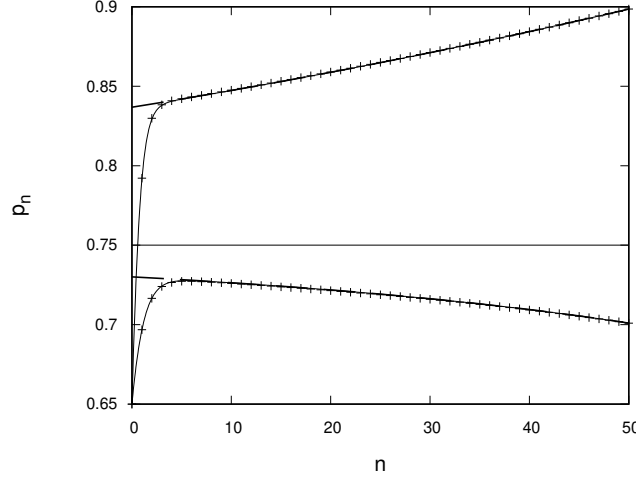


Figure 2.9: Steady state local density profile p_n for a lattice of $N = 50$ nodes and the following parameter values: $\Omega_A = 0.3$, $\Omega_D = 0.1$, $\alpha = 0.65$, $\beta = 0.1$ (upper curve) and $\beta = 0.3$ (lower curve). The numerical results are denoted by the symbols, whereas the solid and dashed lines denote respectively the full analytical expression and the bulk term. The thin horizontal line corresponds to the Langmuir density (2.10).

Applying the factorization (2.6) to (1.8), the current can then be expressed as a function of p_n^t and $C_n(t)$. The currents at the boundaries are

$$J_0(t) = \alpha_1 P_1^t[01] + \alpha_2 P_1^t[00], \quad (2.17)$$

$$J_{N-1}(t) = \beta_1 P_{N-1}^t[10], \quad (2.18)$$

$$J_N(t) = \beta_2 p_n(t) \quad (2.19)$$

We can thus write the dynamical equations for the local densities

$$\dot{p}_n(t) = J_{n-1}(t) - J_n(t), \quad n = 1, \dots, N. \quad (2.20)$$

We now write the time evolution equations for the two-node expectations, it is understood that the k -node marginals with $k \geq 3$ must factor according to (2.6). In the interior of the lattice ($n = 2, \dots, N - 3$) we get (see appendix A for a derivation)

$$\dot{C}_n(t) = \theta P_{n-1}^t[100] + \eta P_n^t[1101] + \theta P_n^t[1100] - J_n(t) \quad (2.21)$$

and at the boundaries we have

$$\dot{C}_1(t) = \alpha_2 P_1^t[00] + \eta P_1^t[1101] + \theta P_1^t[1100] - J_1(t), \quad (2.22)$$

$$\dot{C}_{N-2}(t) = \theta P_{N-3}^t[100] + \beta_1 P_{N-2}^t[110] - J_{N-2}(t), \quad (2.23)$$

$$\dot{C}_{N-1}(t) = \theta P_{N-2}^t[100] + \beta_2 P_{N-1}^t[11] - J_{N-1}(t). \quad (2.24)$$

This approach can be viewed as an extension of the Markov chain approach to kinetics (MCAK) introduced for a model in the KLS class (see [23] and references therein): the latter approximation assumes that, at any time, the correlators $C_n(t)$ are related to the local densities in the same way as they do in the steady state. The continuity equation (2.20) implies a uniform current in the steady state ($J_{n-1} = J_n = J$), therefore we look for a bulk solution (sufficiently far from the boundaries) where the densities and the two-node correlators are position independent. Using the condition $\dot{C}_n(t) = 0$ together with the expression (1.8) for the current in (2.21) and dropping all the indices, we get

$$\begin{aligned} 0 &= \eta P[1101] + \theta P[1100] - \eta P[101] \\ &= \theta P[1100] - \eta P[0101]. \end{aligned} \quad (2.25)$$

Applying the factorization (2.6) and using the expressions for correlators (2.14) - (2.16), we have

$$0 = \theta \frac{(q - C) C (q' - C)}{qq'} - \eta \frac{C^3}{qq'}.$$

We solve with respect to C , obtaining the solutions

$$C_{\pm} = \frac{1 \pm \sqrt{1 - 4qq'(1 - \eta/\theta)}}{2(1 - \eta/\theta)}. \quad (2.26)$$

The solution C_+ is non-negative only if $\eta < \theta$, but even in this case it must be rejected. Indeed we note that in this limit the correlators have the property

$$\begin{aligned} P[01] + P[00] &= 1 - q, \\ P[10] + P[00] &= 1 - q, \end{aligned} \quad (2.27)$$

that implies $P[01] = P[10] < 1/2$. For fixed $0 < \eta < \theta$, the solution C_+ is always greater than $1/2$. For the minimum in $q = 1/2$, we have

$$C_+^{min} - \frac{1}{2} = \frac{1 + \sqrt{\frac{\eta}{\theta}}}{2\left(1 - \frac{\eta}{\theta}\right)} - \frac{1}{2} = \frac{\sqrt{\frac{\eta}{\theta}}}{2\left(1 - \sqrt{\frac{\eta}{\theta}}\right)} > 0.$$

The current corresponding to the bulk solution $C = C_-$ is

$$\begin{aligned} J(q) &= \eta \frac{P[10]P[01]}{q'} + \theta \frac{P[10]P[00]}{q'} \\ &= \eta \frac{C^2}{q'} + \theta \frac{C(q + C)'}{q'} \\ &= \theta q \left(1 - \frac{C}{q'}\right). \end{aligned} \quad (2.28)$$

Substituting the expression for C , it is easy to see that this result is equivalent to (1.9): the bulk current-density relation in the pair approximation is exact. As was mentioned in section 1.3.2, this property comes from the equivalence between the steady state distribution of the AS model and the equilibrium distribution of a 1D Ising model with nearest neighbours interactions, under a suitable choice for the boundary conditions.

Now, we derive the expressions for the bulk-adapted rates: we consider the conditional probability of having the node n occupied given the configuration $\{\nu_{n+1} = 0, \nu_{n+2}\}$ in the steady state of a bulk system with density q , $P[1|0\nu_{n+2}] = P[10\nu_{n+2}]/P[0\nu_{n+2}]$. To write the injection rates (1.10), we weight the hopping rates with the probabilities of having the left auxiliary node occupied given the configuration $\{\nu_1 = 0, \nu_2\}$, in a semi-infinite lattice with density $q = \rho_L$: for $\nu_2 = 1$ we have

$$\alpha_1 = \eta P[1|01] = \eta \frac{P[101]}{P[01]} = \eta \frac{C}{1 - \rho_L} = \eta \left(1 - \frac{J(\rho_L)}{\theta \rho_L}\right), \quad (2.29)$$

whereas for $\nu_2 = 0$ we get

$$\alpha_2 = \theta P[1|00] = \theta \frac{P[100]}{P[00]} = \theta \frac{C}{1 - \rho_L} = \theta \left(1 - \frac{J(\rho_L)}{\theta \rho_L}\right). \quad (2.30)$$

As far as the hopping from node $N - 1$ to node N is concerned, we weight the hopping rates η and θ with the conditional probabilities of having the auxiliary node $N + 1$ occupied and empty respectively, given the configuration $\{\nu_{N-1} = 1, \nu_N = 0\}$ in a semi-infinite lattice with density $q = \rho_R$

$$\beta_1 = \eta P[1|01] + \theta P[0|01] = \eta \frac{P[101]}{P[01]} + \theta \frac{P[100]}{P[01]} = \frac{J(\rho_R)}{C}, \quad (2.31)$$

where the order of the nodes in the conditional probabilities is reversed. Doing the same reasoning for the conditional probabilities of the configuration of the auxiliary nodes $\{\nu_{N+1} = 0, \nu_{N+2}\}$ given $\nu_N = 1$, the extraction rate from node N is given by

$$\beta_2 = \eta P[10|1] + \theta P[00|1] = \eta \frac{P[101]}{\rho_R} + \theta \frac{P[100]}{\rho_R} = \frac{J(\rho_R)}{\rho_R}. \quad (2.32)$$

Inserting the bulk-adapted rates with $\rho_L = \rho_R = q$ into the boundary currents (2.19), by simple algebra we realize that $J_0 = J_{N-1} = J_N = J(q)$ and, from the equations (2.22)-(2.24), we obtain $\dot{C}_1(t) = \dot{C}_{N-2}(t) = \dot{C}_{N-1}(t) = 0$. The pair approximation with this choice for the boundary rates yields a steady state with the exact bulk current-density relation at any finite size N , as a consequence it reproduces the exact location of most static phase transitions. As mentioned in 1.3.2, for strongly attractive interactions, a fourth phase behaving as a high-density is found in the corner of the phase diagram at large ρ_L and small ρ_R . This phenomenon is reproduced by the pair approximation: the bulk density \bar{q}^{IV} of the $\overline{\text{HD}}^{\text{IV}}$ phase is

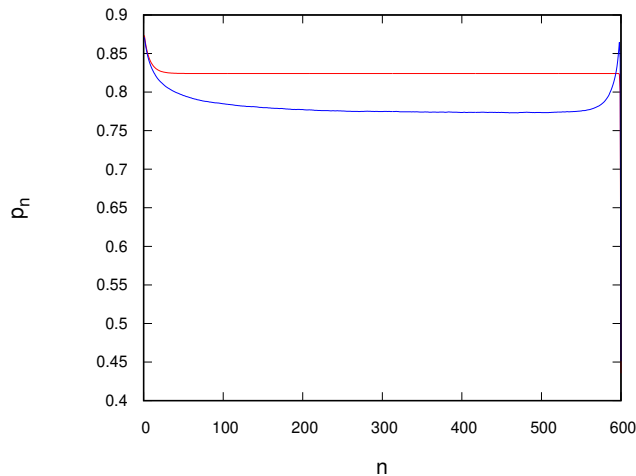


Figure 2.10: Density profile in the fourth phase ($\eta = 1$, $\theta = 0.1$) predicted by the pair approximation (red line) and by the kinetic Monte Carlo simulation (blue line), $\rho_L = 0.9$, $\rho_R = 0.0005$.

slightly larger than that of the MC phase q^* and depends only on ρ_R , the transition between the $\overline{\text{HD}}^{\text{IV}}$ and the MC phase is continuous as a function of the bulk density and is given by the condition $\bar{q}^{\text{IV}} = q^*$, whereas the transition between the fourth phase and the LD one is discontinuous and given by the condition $J(\bar{q}^{\text{IV}}) = J(\rho_L)$. Since \bar{q}^{IV} is neither equal to the boundary densities nor to p^* , we cannot expect the density profile of the $\overline{\text{HD}}^{\text{IV}}$ phase, and as a consequence the phase boundaries, to be exact: in figure 2.10 we show a comparison between the approximate profile obtained by evolving the dynamical equations (2.20)-(2.21) and the profile given by the kinetic Monte Carlo (for the details of this simulation technique see section 4.1).

Chapter 3

The Domain Wall Theory

The Domain Wall Theory (DWT) [3, 28] is a simplified approach to describe the long time relaxational dynamics of driven diffusive models. For the TASEP, it reproduces the static phase boundaries and the exact slowest relaxation rate in a portion of the phase diagram. The DWT is a coarse graining approach which reduces the collective dynamics to the motion of a single coordinate, the position of an interface between two domains with constant densities ρ_L and ρ_R . At the microscopic level, the wall is described as a random walker that hops to the left with rate D_L and to the right with rate D_R , but cannot leave the system because of the fixed boundary densities. The hopping rates are obtained by equating the

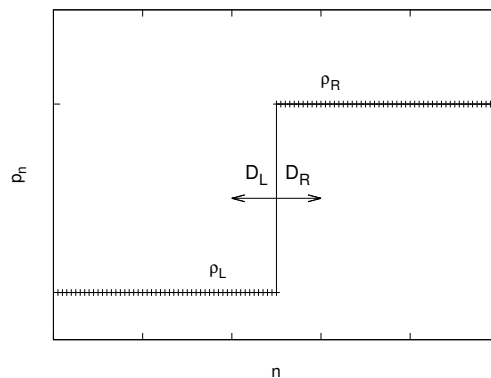


Figure 3.1: Schematic illustration of a domain wall at site n separating a homogeneous region of low density ρ_L from a domain of high-density ρ_R . The wall jumps one node to the left with rate D_L and to the right with rate D_R

mass fluxes into and out of the wall. Assuming that $\rho_R > \rho_L$ as in figure 3.1, we have

$$D_{L,R} = \frac{J(\rho_{L,R})}{\rho_R - \rho_L}. \quad (3.1)$$

When the two currents are different, the random walk is biased with mean velocity

$$v_s = D_R - D_L = \frac{J(\rho_R) - J(\rho_L)}{\rho_R - \rho_L}; \quad (3.2)$$

if this velocity is negative, the bulk of the system reaches the high-density ρ_R in the steady state, otherwise it relaxes to the low-density ρ_L . A discontinuous transition in the bulk density occurs when $J(\rho_L) = J(\rho_R)$: in this case the system shows a coexistence of the low- and high-density phases.

Considering a system of N sites, we identify the position of the domain wall with a lattice site n : the set $\{n + 1, \dots, N\}$ has density ρ_R , while $\{1, \dots, n - 1\}$ has density ρ_L . When $n = 1$, the system is in the high-density phase, while $n = N$ corresponds to the low-density phase. One studies the domain wall dynamics in the bulk of a large system, for $\rho_L < 1/2$ and $\rho_R > 1/2$, under the assumption that all sites have the same values for the hopping rates. As previously mentioned, since the boundary densities are fixed, the domain wall can never leave the system: the site $n = 1$ has zero left hopping rate and right hopping rate D_R , whereas the site $n = N$ has left hopping rate D_L and zero right hopping rate. The dynamics for the probability distribution of the position of the interface is described by the following master equation:

$$\begin{cases} \dot{P}_1(t) = D_L P_2(t) - D_R P_1(t), & (3.3a) \\ \dot{P}_n(t) = D_L P_{n+1}(t) + D_R P_{n-1}(t) - (D_L + D_R) P_n(t), & (3.3b) \\ \dot{P}_N(t) = D_R P_{N-1}(t) - D_L P_N(t), & (3.3c) \end{cases}$$

where $n = 2, \dots, N - 1$. One can now consider an equivalent form by including the sites $n = 1$ and $n = N$ in (3.3b) and replacing (3.3a) and (3.3c) with the boundary conditions

$$D_L P_1(t) = D_R P_0(t), \quad (3.4)$$

$$D_L P_{N+1}(t) = D_R P_N(t), \quad \forall t. \quad (3.5)$$

The coefficient matrix of this system of ordinary differential equations is tridiagonal and quasi-Toeplitz (apart from the elements corresponding to the sites $n = 1$ and $n = N$, it has the Toeplitz property). This matrix has N real eigenvalues, because it can be transformed into a similar symmetric one, exploiting the fact that the off-diagonal elements never change sign; we describe the similarity transformation at the end of the chapter. A general solution has the form

$$P_n(t) = \sum_{\lambda \in \{\lambda_1, \dots, \lambda_N\}} P_n^{(\lambda)} e^{-\lambda t} \quad (3.6)$$

Plugging (3.6) into (3.3b), one obtains a system of second order difference equations for the amplitudes $P_n^{(\lambda)}$ and studies the solutions of the associated characteristic

equation. When this equation admits two distinct solutions ξ and ψ , the amplitudes are given by

$$P_n^{(\lambda)} = A\xi^n + B\psi^n$$

and, using the boundary conditions (3.4) and (3.5), one arrives at the system

$$\begin{cases} A(\xi^N - \psi^N)(D_R - D_L\xi) = 0 \\ B(\xi^N - \psi^N)(D_R - D_L\psi) = 0 \end{cases} \quad (3.7)$$

The possible solutions are $A \neq 0, B = 0$ and $\xi = \frac{D_R}{D_L}$ or $A = 0, B \neq 0$ and $\psi = \frac{D_R}{D_L}$. The stationary probability distribution, corresponding to $\lambda = 0$, has the form

$$P_n \propto \left(\frac{D_R}{D_L}\right)^n. \quad (3.8)$$

In the degenerate case with two real coincident solutions $\xi = \psi = \zeta$, the amplitudes are written in the form

$$P_n^{(\lambda)} = A\zeta^n + Bn\zeta^n,$$

but, from the boundary conditions, it turns out that $B = 0$. The characteristic equation has solutions $\zeta = \sqrt{\frac{D_R}{D_L}}$, which do not satisfy the boundary conditions. Then, one considers the case in which the characteristic equation has two complex conjugate solutions $\xi = re^{i\phi}$ and $\psi = re^{-i\phi}$ ($A \neq 0$ and $B \neq 0$). Solving the equation $\xi^N = \psi^N$, it turns out that $\phi = k\pi/N$ with $k \in \mathbb{Z}$, but the values $\phi = 0$ and $\phi = \pi$ correspond to the cases with coincident solutions $\xi = \psi = r = \sqrt{\frac{D_R}{D_L}}$ and $\xi = \psi = -r$ respectively, which have been rejected. Thence, the independent valid solutions are for $k = 1, \dots, N - 1$. Plugging them into the characteristic equation, one derives the relaxation spectrum

$$\lambda_k = D_L + D_R - 2\sqrt{D_L D_R} \cos\left(\frac{k\pi}{N}\right). \quad (3.9)$$

Thus, in the infinite size limit, the slowest relaxation rate is

$$\lambda_{DWT} = D_L + D_R - 2\sqrt{D_L D_R}. \quad (3.10)$$

This quantity is finite for a biased random walk and goes to zero along the coexistence line ($D_L = D_R$, critical slowing down).

The DWT rate turns out to be exact for pure TASEP in the *slow* phases, i.e. in the HD-s and LD-s regions of the phase diagram in figure 1.1b, and the dynamical transition corresponds to the maximum rate, but, for $\alpha > \alpha_c(\beta)$, the rate detaches from the exact solution. De Gier and Essler [2] proposed a Modified Domain Wall Theory, which amounts to taking the DWT rate in the *slow* phase and the maximum rate in the *fast* one (see figure 3.2): this is a heuristic strategy and, for this

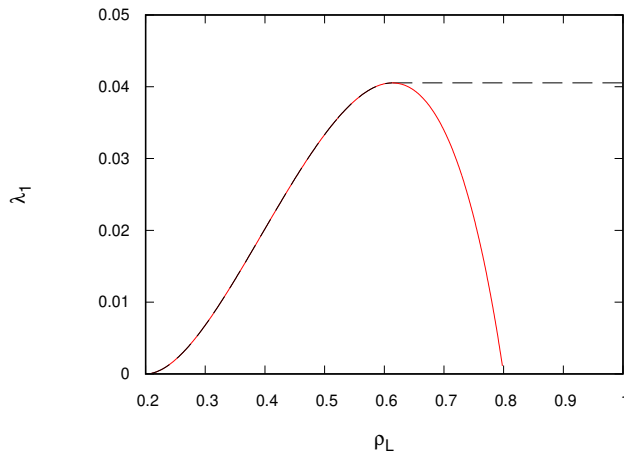


Figure 3.2: DWT rate (red line) and mDWT solution (black dashed line) for the TASEP at $\rho_R = 1 - \beta = 0.8$, as a function of $\rho_L = \alpha$. The critical injection rate $\alpha_c(\beta) \simeq 0.6135$ is exact.

model, it is exact by construction.

This approach is used in chapter 7, together with the pair approximation and the Bulirsch-Stoer extrapolation of exact finite size results, to investigate the dynamical transitions in the AS model. In section 6.1 we present a generalization of the mDWT to the TASEP-LK.

3.0.1 Similarity transformation for Jacobi matrices

We illustrate the similarity transformation for the coefficient matrix of the master equation in (3.3a)-(3.3c). We will see again this symmetrization in section 5.1, when dealing with the mean-field relaxation matrix of the TASEP-LK. We start from the eigenvalue equation for $n = 2, \dots, N - 1$

$$D_L P_{n+1}(t) + D_R P_{n-1}(t) - (D_L + D_R) P_n(t) = \lambda P_n(t) \quad (3.11)$$

and we define

$$\tilde{P}_n(t) \equiv P_n(t) \left(\sqrt{\frac{D_L}{D_R}} \right)^{n-1}, \quad (3.12)$$

Plugging this into (3.11), we get

$$\sqrt{D_L D_R} \tilde{P}_{n+1}(t) + \sqrt{D_L D_R} \tilde{P}_{n-1}(t) - (D_L + D_R) \tilde{P}_n(t) = \lambda \tilde{P}_n(t). \quad (3.13)$$

Doing the same for nodes $n = 1$ and $n = N$, we obtain

$$\sqrt{D_L D_R} \tilde{P}_2(t) - D_R \tilde{P}_1(t) = \lambda \tilde{P}_1(t) \quad (3.14)$$

$$\sqrt{D_L D_R} \tilde{P}_{N-1}(t) - D_L \tilde{P}_N(t) = \lambda \tilde{P}_N(t) \quad (3.15)$$

More in general we can say that this symmetrization can be applied to Jacobi matrices, that are tridiagonal matrices whose off-diagonal elements are all of the same sign. In such a case, the factor $(\sqrt{D_L/D_R})^{n-1}$ is replaced by a product of sub-diagonal elements.

Chapter 4

Monte Carlo and numerical techniques

In this chapter we introduce the Monte Carlo and numerical methods employed in our research activity: the kinetic Monte Carlo, the computation of the exact slowest relaxation rate at finite size and the Bulirsch-Stoer extrapolation of the results to the $N \rightarrow \infty$ limit.

4.1 Kinetic Monte Carlo: the Gillespie algorithm

The *Stochastic Simulation Algorithm* developed by Gillespie [29] is an efficient Monte Carlo technique to simulate continuous time Markov processes. The basic idea of this algorithm is to draw at random both the time of the next transition and which of the possible states is taken instead of trying a movement at each step and rejecting or accepting it: for each pair of generated random numbers a new state is selected, this is a direct generation method with 100% efficiency.

We consider the dynamics of a system which can take discrete states labeled by integers x, y, \dots . The system can go from the state x to a different state y with rate $\mathcal{W}_{x \rightarrow y}$, so that the total probability that the system leaves the current state x in the next Δt is $\Delta t \sum_{y \neq x} \mathcal{W}_{x \rightarrow y} = \Delta t \mathcal{W}_{x \rightarrow \bullet}$. We divide the interval $[0, t]$ into n sub-intervals $\Delta t = t/n$, the probability $P_x^s(t)$ that the system remains in the same state after t units of time is equal to

$$P_x^s(t) = \left(1 - \frac{t}{n} \mathcal{W}_{x \rightarrow \bullet}\right)^n \xrightarrow{\Delta t \rightarrow 0} \exp(-t \mathcal{W}_{x \rightarrow \bullet}).$$

Therefore, the probability that the system leaves the current state before time t , that is the cumulative distribution of the time until the next transition, is given by

$$\mathcal{F}_x(t) = 1 - \exp(-t \mathcal{W}_{x \rightarrow \bullet}); \quad (4.1)$$

the distribution of leaving times is exponential with parameter $\mathcal{W}_{x \rightarrow \bullet}$,

$$P_x(t) = \mathcal{W}_{x \rightarrow \bullet} \exp(-t\mathcal{W}_{x \rightarrow \bullet}). \quad (4.2)$$

We illustrate the structure of the algorithm for a generic Markovian stochastic system:

1. initialization ($t = 0$): define the initial condition x (e.g. empty lattice);
2. draw two random numbers ξ_1 and ξ_2 from a uniform distribution in the interval $(0,1]$;
3. time of the next transition

$$\tau = -\frac{1}{\mathcal{W}_{x \rightarrow \bullet}} \ln \xi_1; \quad (4.3)$$

4. choice of the new state y with probability $\frac{\mathcal{W}_{x \rightarrow y}}{\mathcal{W}_{x \rightarrow \bullet}}$: it is the integer for which

$$\sum_{k=1}^{y-1} \mathcal{W}_{x \rightarrow k} < \xi_2 \mathcal{W}_{x \rightarrow \bullet} \leq \sum_{k=1}^y \mathcal{W}_{x \rightarrow k};$$

5. updating: update the state of the system ($x := y$) and the rates of the corresponding transition processes, increment time by τ ($t := t + \tau$), then go to step 2.

Considering the TASEP dynamics for a lattice of N sites, we recall the occupation numbers $\nu_n^t \in \{0,1\}$ introduced in 1.2. We denote by $x = \{x_1 = \nu_1^t, \dots, x_N = \nu_N^t\}$ and $y = \{y_1 = \nu_1^{t+\tau}, \dots, y_N = \nu_N^{t+\tau}\}$ the lattice configurations at two subsequent times. We have $N + 1$ possible processes:

- particle entering the lattice at site 1 with rate $W_{y,x}^0 = \alpha(1 - \nu_1^t)$;
- $N - 1$ hopping processes with rates $W_{y,x}^n = \nu_n^t(1 - \nu_{n+1}^t)$, $1 \leq n \leq N - 1$;
- particle leaving the lattice at site N with rate $W_{y,x}^N = \beta\nu_N^t$.

After choosing the new state, we have to update the lattice configuration and the rates of the transition processes according to the selected move. Also the rates of the processes involving the neighbouring sites change: as an example, if a hopping process from site n to the adjacent one is chosen, then $\nu_n^{t+\tau} = 0, \nu_{n+1}^{t+\tau} = 1$. The updated rates are $W_{y,x}^{n-1} = \nu_{n-1}^{t+\tau}$, $W_{y,x}^n = 0$ and $W_{y,x}^{n+1} = 1 - \nu_{n+2}^{t+\tau}$.

4.2 Computing the exact slowest relaxation rate for finite size systems

In order to compute the exact slowest relaxation rate for finite size systems, we introduce the reduced transition matrix: it is obtained from the matrix of the transition rates after eliminating the zero eigenvalue, which corresponds to the steady state. This manipulation reduces the computational cost of finding the slowest relaxation rate, that is the smallest nonzero eigenvalue of the transition matrix changed of sign. To compute this quantity, we adopt an iterative Arnoldi algorithm [30] that is implemented in the Matlab routine `eigs()`, or alternatively in the ARPACK package [31]: it can compute a small subset of eigenvalues of large sparse matrices (i.e. with most of the entries equal to zero) according to a selection criterion, such as the largest/smallest magnitude or real part.

Considering a lattice of N sites, we have 2^N possible states: in a binary encoding, $x = 0$ is the configuration with all the sites being empty and $x = 2^N - 1$ is the state with all the sites being occupied. The action of the reduced transition matrix for this system is the result of removing the first row and subtracting the first column, which correspond respectively to the transitions to and from the completely empty configuration. We recall the master equation (1.3) for the probability $P^t[x]$ of having a given configuration x of the lattice nodes at time t

$$\dot{P}^t[y] = \sum_x W_{y,x} P^t[x],$$

The transition matrix (1.4) introduced in section 1.2 satisfies the properties

$$W_{y,x} \geq 0, \quad x \neq y, \tag{4.4}$$

$$\sum_y W_{y,x} = 0, \quad \forall x. \tag{4.5}$$

The second one comes from the conservation of probability and shows that the matrix \mathbf{W} has a left eigenvector $\mathbf{v} = (1, 1, \dots)$ with zero eigenvalue. Henceforth, there exists also a right eigenvector \mathbf{w} with the same eigenvalue. Each eigenvector with this property is a time independent solution of the master equation and all its components are either negative or positive. Choosing the normalization in order to have positive components, one obtains the probability distribution of the system in the steady state, which is unique. All the other eigenvalues have negative real parts and their corresponding eigenvectors have a sum of the components equal to zero. Denoting eigenvector components by δP_x (since they can be regarded as perturbations over the steady state), we can thus write

$$\sum_x W_{y,x} \delta P_x = \lambda \delta P_y, \quad \lambda \neq 0. \tag{4.6}$$

Then, summing over y

$$\sum_x \left(\sum_y W_{y,x} \right) \delta P_x = \lambda \sum_y \delta P_y = 0 \quad (4.7)$$

and hence

$$\sum_y \delta P_y = 0. \quad (4.8)$$

In the master equation we assume $y \neq 0$, we separate the transitions from the configuration with all the sites empty

$$\sum_x W_{y,x} \delta P_x = W_{y,0} \delta P_0 + \sum_{x \neq 0} W_{y,x} \delta P_x;$$

for the property (4.8) we have

$$\delta P_0 = - \sum_{x \neq 0} \delta P_x, \quad (4.9)$$

we substitute into the master equation and we obtain

$$\begin{aligned} \sum_x W_{y,x} \delta P_x &= -W_{y,0} \sum_{x \neq 0} \delta P_x + \sum_{x \neq 0} W_{y,x} \delta P_x \\ &= -W_{y,0} \sum_{x \neq 0} \delta P_x + \sum_{x \notin \{0,y\}} W_{y,x} \delta P_x + W_{y,y} \delta P_y. \end{aligned}$$

Using the definition of the diagonal elements in (1.4), we obtain the following form for the action of the reduced transition matrix

$$\begin{aligned} \sum_x W_{y,x} \delta P_x &= -W_{y,0} \sum_{x \neq 0} \delta P_x + \sum_{x \notin \{0,y\}} W_{y,x} \delta P_x + \\ &\quad - \sum_{z \neq y} W_{z,y} \delta P_y. \end{aligned} \quad (4.10)$$

We will employ the approach outlined here to compute the slowest relaxation rate for different system sizes (up to $N = 24$), then we will extrapolate the results to the infinite size limit using the technique explained in the next section.

4.3 The Bulirsch-Stoer extrapolation method

The Bulirsch-Stoer (BST) method is an iterative algorithm to extrapolate sequences of finite size data to the thermodynamic limit, it can give accurate results even with a small number of entries. In [32], it was adopted to extrapolate the exact finite size values of the slowest relaxation rate for the TASEP.

To introduce the algorithm, we consider the numerical integration of a real function over the interval $[a, b]$: we divide the interval into N steps of length $h = (b - a)/N$ and we compute the integral for different partitions, reducing at each time the step-size. We want to extrapolate the results to the limit $h = 0$.

Many integration schemes rely on the trapezoidal rule because its error contains only even powers of h , we can see that from the Euler-Maclaurin summation formula

$$\int_{x_0}^{x_{N-1}} f(x)dx = h \left[\frac{1}{2}f(x_0) + f(x_1) + \dots + \frac{1}{2}f(x_{N-1}) \right] - \frac{B_2 h^2}{2!} (f'(x_{L-1}) - f'(x_0)) + \dots - \frac{B_{2k} h^{2k}}{(2k)!} (f^{(2k-1)}(x_{N-1}) - f^{(2k-1)}(x_0)) - \dots,$$

where $x_i = x_0 + ih$, $i = 0, 1, \dots, N - 1$ and $x_0 = a$. The B_{2k} are the Bernoulli numbers generated by the function

$$\frac{t}{e^t - 1} = \sum_{k=0}^{\infty} B_k \frac{t^k}{k!}.$$

This property allows to apply recursively the trapezoidal rule k times to remove the error terms up to $O(1/N^{2k})$: as an example, let I_N be the result of the numerical quadrature with N steps. If we double the number of steps, the ratio between the leading order error terms of the two evaluations is $1/4$, thus the combination $\frac{4}{3}I_{2N} - \frac{1}{3}I_N$ eliminates this term reducing the correction to $O(1/N^4)$. These successive refinements are performed using the Neville's algorithm [33]. This is an efficient way to determine the value at a given x of the polynomial of degree $N - 1$ which interpolates the N points $y_i = f(x_i)$, $i = 0, \dots, N - 1$. We start with the constants $P_i = y_i$, $i = 0, \dots, N - 1$, then we denote by $P_{i,i+1}$ the value at x of the line passing through the points (x_i, y_i) and (x_{i+1}, y_{i+1}) and we go on up to the final polynomial $P_{0,1,\dots,N-1}$. We can visualize the recursive structure with a table in which two parents on the left lead to a single descendant on the right, we write an example for $N = 3$

$$\begin{array}{rcc} x_0 & \rightarrow & y_0 = P_0 \\ & & P_{01} \\ x_1 & \rightarrow & y_1 = P_1 & P_{012} \\ & & P_{12} \\ x_2 & \rightarrow & y_2 = P_2 \end{array} \quad (4.11)$$

Parents and descendants are linked by the relation

$$P_{i,i+1,\dots,i+l} = \frac{(x - x_{i+l})P_{i,i+1,\dots,i+l-1} + (x_i - x)P_{i+1,i+2,\dots,i+l}}{x_i - x_{i+l}}, \quad (4.12)$$

where $l = 1, \dots, N - 1$.

Bulirsch and Stoer [34] worked on the extrapolation of tabulated rational functions

with an approach of the Neville type: we denote by $R_t^{\gamma,\delta}(x)$ the rational function passing through the $n + 1$ points $(x_j, f(x_j)), j = t, t + 1, \dots, t + n$ and $n = \gamma + \delta$

$$R_t^{\gamma,\delta}(x) = \frac{e_0 + e_1x + \dots + e_\gamma x^\gamma}{g_0 + g_1x + \dots + g_\delta x^\delta}, \quad R_t^{\gamma,\delta}(x_j) = f(x_j),$$

where γ and δ are the degrees of the polynomials in the numerator and in the denominator respectively and $\delta = \gamma$ or $\delta = \gamma + 1$.

We adopt the notation $T_{i,k} := R_t^{\gamma,\delta}(x)$ with $i = t + \gamma + \delta$, $k = \gamma + \delta$; in this case the recursion is given by [35]

$$\begin{aligned} T_{i,0} &= f(x_i), \quad T_{i,-1} = 0, \\ T_{i,k} &= T_{i,k-1} + \frac{T_{i,k-1} - T_{i-1,k-1}}{\frac{x-x_{i-k}}{x-x_i} \left[1 - \frac{T_{i,k-1} - T_{i-1,k-1}}{T_{i,k-1} - T_{i-1,k-2}} \right] - 1}, \end{aligned} \quad (4.13)$$

with $i = 0, 1, \dots$ and $1 \leq k \leq i$.

We apply this method to our quadrature problem: let $T(h)$ be the expansion in terms of h of the trapezoidal sum of the integrand function

$$T(h) = t_0 + t_1 h^2 + t_2 h^4 + \dots,$$

where t_0 is the integral that we want to compute. We define the sequence of stepsizes

$$h_0 = \frac{b-a}{n_0}, \quad h_1 = \frac{b-a}{n_1}, \dots, \quad h_l = \frac{b-a}{n_l},$$

with $0 < n_0 < n_1 < \dots < n_l$, $T(h_i)$ is the result of the trapezoidal rule for a given partition. We write a rational interpolating function in h^2

$$\bar{T}_{ik}(h) = \frac{e_0 + e_1 h^2 + \dots + e_\gamma h^{2\gamma}}{g_0 + g_1 h^2 + \dots + g_\delta h^{2\delta}} \quad (4.14)$$

with the property

$$\bar{T}_{ik}(h_j) = T(h_j), \quad j = i - k, i - k + 1, \dots, i.$$

We define $T_{ik} := \bar{T}_{ik}(0)$, the recursion (4.13) with $x_i = h_i^2, i = 0, 1, \dots, l$ and $x = 0$ becomes

$$\begin{aligned} T_{i,0} &= T(h_i), \quad i = 0, \dots, l; \quad T_{i,-1} = 0, \quad i = 0, \dots, l - 1; \\ T_{i,k} &= T_{i,k-1} + \frac{T_{i,k-1} - T_{i-1,k-1}}{\left(\frac{h_{i-k}}{h_i}\right)^2 \left(1 - \frac{T_{i,k-1} - T_{i-1,k-1}}{T_{i,k-1} - T_{i-1,k-2}}\right)}, \quad 1 \leq k \leq i \leq l. \end{aligned} \quad (4.15)$$

Henkel and Schütz [36] considered the extrapolation of quantities scaling as $1/N^\sigma$ and modified the recursion as

$$T_{i,k} = T_{i,k-1} + \frac{T_{i,k-1} - T_{i-1,k-1}}{\left(\frac{h_{i-k}}{h_i}\right)^\sigma \left(1 - \frac{T_{i,k-1} - T_{i-1,k-1}}{T_{i,k-1} - T_{i-1,k-2}}\right)}. \quad (4.16)$$

They studied the effect of varying the parameter σ on the result of the extrapolation. In particular, they observed the formation of poles in the last extrapolants and proposed the criterion of choosing σ as the value that minimizes the error

$$\epsilon_{l,i} = 2(T_{l,i+1} - T_{l,i}). \quad (4.17)$$

Part II

Our contribution

Chapter 5

Dynamical transitions in the TASEP-LK: mean-field approach

In this chapter we present our investigation of the dynamical transitions in the TASEP-LK, working in the framework of the mean-field approximation. We discuss separately the balanced case with equal binding and unbinding rates and the more general one with unbalanced rates: in the former model, it turns out that the dynamical transition line can be obtained from that of the pure TASEP through the same mapping introduced in section 2.2.1 when discussing the static phase diagram. In the latter case, a new type of dynamical transition is observed, that shows some analogies with equilibrium first-order transitions. As far as the balanced case is concerned, we present a formal derivation of the properties of the density profile in the HD phase, which is the basis for the determination of the asymptotic behaviour of the mean-field slowest relaxation rate in the infinite size limit: these results have been published in [26]. We then describe in some detail the analysis of the unbalanced case, focusing the attention on the new features of the dynamical transition. The proofs of most of the results presented in this chapter are reported in appendix B.

5.1 Steady state and relaxation in mean-field

With reference to the mean-field theory for the model introduced in 2.2, we now describe the solution of the dynamical equations (2.7) in the steady state and the approach to study the relaxation process. We recall the time evolution equations (2.7) for the local densities

$$\dot{p}_n(t) = J_{n-1}(t) - J_n(t) + \omega_A p'_n(t) - \omega_D p_n(t), \quad n = 1, \dots, N,$$

and the mean-field current-density relation (2.8)

$$J_n(t) \equiv p_n(t) p'_{n+1}(t), \quad n = 0, \dots, N.$$

We observe that the equations (2.9) satisfied by the local densities in the steady state

$$p_n (p_{n+1}' + \omega_D) = (p_{n-1} + \omega_A) p_n', \quad n = 1, \dots, N,$$

can be rewritten in a fixed-point form, namely

$$p_n = \left(1 + \frac{p_{n+1}' + \omega_D}{p_{n-1} + \omega_A} \right)^{-1} \quad n = 1, \dots, N. \quad (5.1)$$

The latter recursion can be solved numerically keeping p_0 and p_{N+1} fixed. In the hypothesis that α and β are both strictly positive, it was proved [26] to admit a unique solution with the property $0 < p_n < 1$, $n = 1, \dots, N$.

To study the relaxation, we linearize (2.7) and (2.8) close to the steady state: we assume the occupation probabilities to be given by the stationary value plus a small time dependent perturbation $y(t)$

$$p_n(t) = p_n + y_n(t), \quad n = 0, \dots, N + 1, \quad (5.2)$$

where $y_0(t) = y_{N+1}(t) = 0$, $\forall t$. We plug this ansatz into (2.8) and (2.7), keeping at most the linear terms in the perturbation

$$\dot{y}_n(t) = -a_n y_n(t) + p_n y_{n+1}(t) + p_n' y_{n-1}(t) \quad n = 1, \dots, N, \quad (5.3)$$

with

$$a_n \equiv p_{n+1}' + p_{n-1} + \omega_A + \omega_D. \quad (5.4)$$

We obtain a system of first-order ordinary differential equations characterized by a tridiagonal coefficient matrix, called relaxation matrix. In the special case of pure TASEP ($\omega_A = \omega_D = 0$), the density profile is constant apart from a boundary layer close to the left end, thus the relaxation matrix is quasi-Toeplitz [1].

A relaxation mode of the system is a solution of the type

$$y_n(t) = v_n e^{-\lambda t} \quad n = 0, \dots, N + 1, \quad (5.5)$$

where $v_0 = v_{N+1} = 0$, according to the boundary conditions, and λ is the relaxation rate. Using (5.5) in (5.3), we get the eigenvalue problem associated with the relaxation matrix

$$a_n v_n - p_n v_{n+1} - p_n' v_{n-1} = \lambda v_n \quad n = 1, \dots, N. \quad (5.6)$$

In section 5.2.2 we will analyse this problem concentrating on the smallest eigenvalue λ_{\min} , which corresponds to the relevant relaxation mode at long times. The determination of the singular behaviour of the mean-field slowest relaxation rate in the infinite size limit (i.e. the dynamical transition) is the main contribution of the work described in this chapter.

We observe that the relaxation matrix is of the Jacobi type, thus we can apply the similarity transformation introduced in section 3.0.1. In this case, the eigenvector components are multiplied by a product of sub-diagonal elements, thus we define

$$u_n \equiv v_n \prod_{k=0}^{n-1} \sqrt{\frac{p_k}{p_{k+1}}}, \quad n = 0, \dots, N + 1, \quad (5.7)$$

where it is understood that the product is 1 for $n = 1$. From equation (5.6), we obtain

$$a_n u_n - \sqrt{p_n p_{n+1}'} u_{n+1} - \sqrt{p_{n-1} p_n'} u_{n-1} = \lambda u_n \quad n = 1, \dots, N, \quad (5.8)$$

with the usual boundary conditions

$$u_0 = u_{N+1} = 0. \quad (5.9)$$

5.2 The balanced case

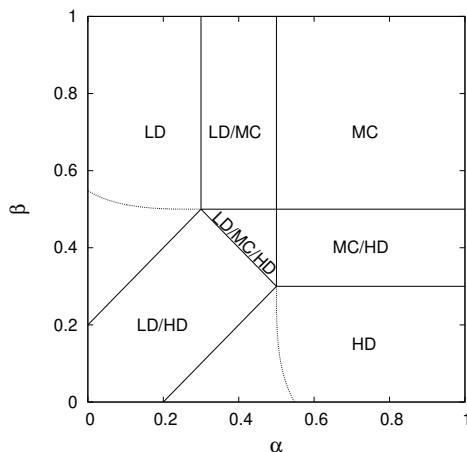


Figure 5.1: Symmetric TASEP-LK phase diagram with the mean-field dynamical transition lines.

In this section, the analysis is restricted to the case with equal binding/unbinding rates ($\Omega_A = \Omega_D = \Omega$), which preserves the HD-LD duality. Thus, we concentrate on the HD phase, all the results can be rephrased for the LD one through the particle-hole symmetry of the pure TASEP (see sec. 1.2). In figure 5.1 we show the mean-field dynamical transition line on the phase diagram of the model.

We denote by $\lambda_{\min}^{(N)}$ the slowest relaxation rate for a system of size N and we

introduce the quantity $q_0 = \beta + \Omega$, whose meaning is explained in the following. In the infinite-size limit, this eigenvalue takes the form

$$\lambda_{\min}^{(\infty)} \equiv \lim_{N \rightarrow \infty} \lambda_{\min}^{(N)} = 1 - \frac{x_*}{x_o}, \quad (5.10)$$

$$\frac{1}{x_o} \equiv 2\sqrt{q_0 q_0'}. \quad (5.11)$$

The value x_* is determined by the behaviour of a real function $f(x; \alpha, q_0)$ of the real variable $x \geq 1$ and of the model parameters α , β and Ω : in this section we give a qualitative description of the relevant features of the dynamical transition, the details of the derivation are postponed to the following sections and the most technical results are proved in appendix B (sections B.1 and B.2). The function is expressed by the series

$$f(x) \equiv 2x_o \sum_{n=1}^{\infty} (s_{n+1} - s_{n-1}) v_n(x) \zeta(x)^n, \quad (5.12)$$

where

$$\zeta(x) \equiv x - \sqrt{x^2 - 1}. \quad (5.13)$$

Its dependence on the model parameters is enclosed in x_o , defined by (5.11), and in s_n and $v_n(x)$, which are defined by recursion as

$$s_0 \equiv \alpha, \quad s_{n+1} \equiv 1 - \frac{1}{4x_o^2 s_n} \quad n = 0, 1, 2, \dots \quad (5.14)$$

and

$$v_0(x) \equiv 0, \quad v_1(x) \equiv 1, \quad (5.15)$$

$$v_{n+1}(x) \equiv [2x - 2x_o (s_{n+1} - s_{n-1})] v_n(x) - v_{n-1}(x) \quad n = 1, 2, \dots \quad (5.16)$$

Comparing the slowest relaxation rate (5.10) with that of the pure TASEP reported in [1], we see that it can be deduced from the latter by the mapping $\beta \mapsto \beta + \Omega$ introduced in 2.2.1. For the same reason, the dependence of f on β and Ω goes only through their sum.

For a given value of q_0 , there exists an interval of α values larger than a critical threshold α_c ¹ such that

$$f(x; \alpha, q_0) < 1 \quad \forall x \geq 1. \quad (5.17)$$

This interval is characterized by the fact that $x_* = 1$, thus the relaxation rate (5.10) is independent of α . When α becomes smaller than α_c , condition (5.17) is no longer

¹This α_c is the mean-field estimate, it does not coincide with the exact one mentioned in the introduction.

satisfied. In particular, $f(1; \alpha, q_0) > 1$ and also x_* becomes greater than one, being determined by the equation

$$f(x_*; \alpha, q_0) = 1. \quad (5.18)$$

The value x_* shows no discontinuity in the α variable. It increases, and as a consequence the relaxation rate decreases, upon decreasing the injection rate: the critical threshold $\alpha_c(q_0)$ is found by solving numerically the equation

$$f(1; \alpha_c, q_0) = 1. \quad (5.19)$$

At fixed Ω , the latter condition defines a critical line in the α - β phase diagram, which has been reported in figure 5.1 together with its low density counterpart. In figure 5.2 we show the behaviour of f as a function of x , for some representative values of the parameters. We consider the interval $[1, x_o]$ and we will prove that

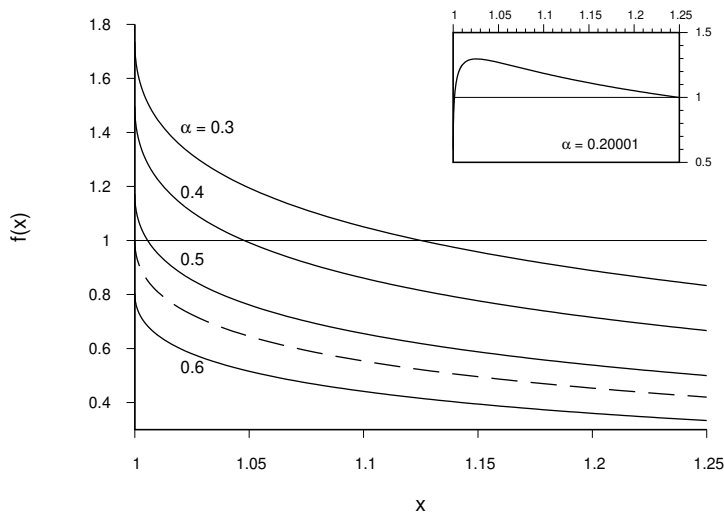


Figure 5.2: Plots of $f(x; \alpha, q_0)$ as a function of the variable x in the interval $[1, x_o]$, for $q_0 = 0.2$ (thus $x_o = 1.25$) and different α values. The case $\alpha = \alpha_c$ is denoted by a dashed line. The inset displays a case with α very close to q_0 (still in the HD phase).

x_* is bounded therein (see Lemma 6 in section 5.2.2, statement (ii)). At a given q_0 , the lower-bound value $x_* = 1$ (corresponding to $\lambda_{\min}^{(\infty)} = 1 - 1/x_o$) is reached in the whole region $\alpha \geq \alpha_c$. From the inset of figure 5.2, we can see that x_* tends to the upper-bound value x_o (which corresponds to $\lambda_{\min}^{(\infty)} \rightarrow 0$) as α tends from above to q_0 , that is to the boundary between the pure HD phase and the LD/HD coexistence region. We also observe that, close to this boundary, the function $f(x)$ is no longer monotonic and a second solution of equation (5.18) may appear, but we will prove (see criterion 2) it to be irrelevant. Along the coexistence line we have an “ordinary” dynamical transition (i.e. one accompanied by a static transition)

and we expect to find a relaxation process which is no longer exponential.

We can give a physical interpretation of the square root argument appearing in x_o (5.11): even if in the TASEP-LK the steady-state current is not uniform, we can still define a node-independent maximum current. Denoting by $J_{\max}^{(N)}$ the maximum current for a system of size N , in the infinite-size limit we have

$$J_{\max}^{(\infty)} \equiv \lim_{N \rightarrow \infty} J_{\max}^{(N)} = \frac{1}{4x_o^2}, \quad (5.20)$$

which coincides with the argument of the square-root. This result generalizes a property first observed in [1] and states that a steady state being more out of equilibrium requires a longer time to be established.

We have also derived bounds for the asymptotic behavior of the relaxation rate $\lambda_{\min}^{(N)}$ in the infinite size limit: the dynamical transition discriminates between two different scaling regimes, which are in turn affected by the presence of the Langmuir kinetics, independently of the value of the attachment/detachment rate Ω (provided that it is different from zero). In the fast phase ($x_* = 1$) we have

$$\lambda_{\min}^{(N)} = \lambda_{\min}^{(\infty)} + \begin{cases} O(N^{-2}) & \text{if } \Omega = 0 \\ O(N^{-2/3}) & \text{if } \Omega > 0 \end{cases}, \quad (5.21)$$

whereas for $\alpha < \alpha_c$ ($x_* > 1$) we have

$$\lambda_{\min}^{(N)} = \lambda_{\min}^{(\infty)} + \begin{cases} O(\zeta(x_*)^{2N}) & \text{if } \Omega = 0 \\ O(N^{-1}) & \text{if } \Omega > 0 \end{cases}, \quad (5.22)$$

where $\zeta(x)$ is defined by (5.13) and satisfies $\zeta(x) < 1$ for $x > 1$. We proved analytically that the distance between $\lambda_{\min}^{(N)}$ and $\lambda_{\min}^{(\infty)}$ is asymptotically bounded from above (up to a positive constant factor) by the scaling functions appearing in parentheses, but we have clear numerical evidences that this scaling is optimal. In figures 5.3 and 5.4 we show a comparison between numerical results and the proposed scaling functions for the pure TASEP and the TASEP-LK respectively. We observe that, for the values of β and Ω chosen in this example, in both cases the critical injection rate α_c is the same. In the TASEP-LK, the difference $\lambda_{\min}^{(N)} - \lambda_{\min}^{(\infty)}$ scales with N as a power law with two different exponents, depending on whether $\alpha > \alpha_c$ or $\alpha < \alpha_c$. In the fast phase, the numerical results suggest that the multiplying factor might be independent of α as well. In the pure TASEP case, the scaling changes from an exponential regime in the slow phase, with the characteristic parameter depending on x_* and thence on α , to a power law one in the fast phase, where the multiplying factor is quite clearly independent of the injection rate. The exact result [9] for the pure TASEP predicts a power-law behaviour with a unique scaling exponent 2, being unaffected by the dynamical transition, whereas only the prefactor displays a discontinuity at α_c [13]. It is remarkable that the

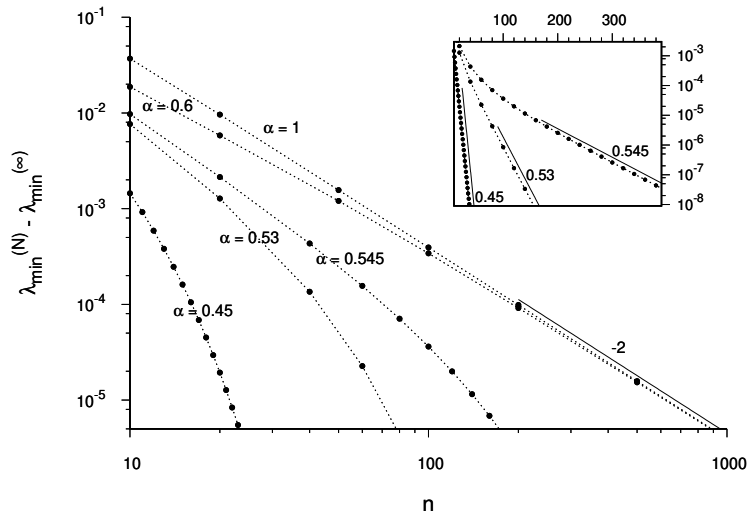


Figure 5.3: Difference between the finite-size slowest relaxation rate $\lambda_{\min}^{(N)}$ and its infinite-size limit value $\lambda_{\min}^{(\infty)}$ as a function of N (circles) for the pure TASEP ($\Omega = 0$) with $\beta = 0.2$ and different α values, both above and below the critical threshold $\alpha_c \approx 0.54786$. Solid lines represent scaling functions, i.e. $\propto N^{-2}$ in the main figure and $\propto \zeta(x_*)^{2N}$ in the inset (with x_* depending on α and β , see the text). Dotted lines are an eyeguide.

mean field scaling exponent coincides with the exact one in the fast phase. The maximum current has the following asymptotic behaviour, which does not change at the dynamical transition.

$$J_{\max}^{(N)} = J_{\max}^{(\infty)} + \begin{cases} O\left(\zeta(x_o)^{2N}\right) & \text{if } \Omega = 0 \\ O(N^{-1}) & \text{if } \Omega > 0 \end{cases}, \quad (5.23)$$

This result is justified by (5.43) in Corollary 1 and by the definition of $\zeta(x_o)$ in (5.59).

5.2.1 Properties of steady state density profile

As was mentioned in 2.2.1, the bulk density profile of the HD phase is linear in the node index n with slope ω

$$q_n = (\beta + \Omega)' + \omega n, \quad n = 0, \dots, N + 1. \quad (5.24)$$

The sequence $(q_n)_{n=0}^{N+1}$ satisfies both the steady-state equations (check (2.9) with $\omega_A = \omega_D = \omega$) and $q_{N+1} = \beta'$. We introduce the *detrended densities*

$$r_n \equiv p_n - (q_n - q_0) = p_n - \omega n, \quad n = 0, \dots, N + 1, \quad (5.25)$$

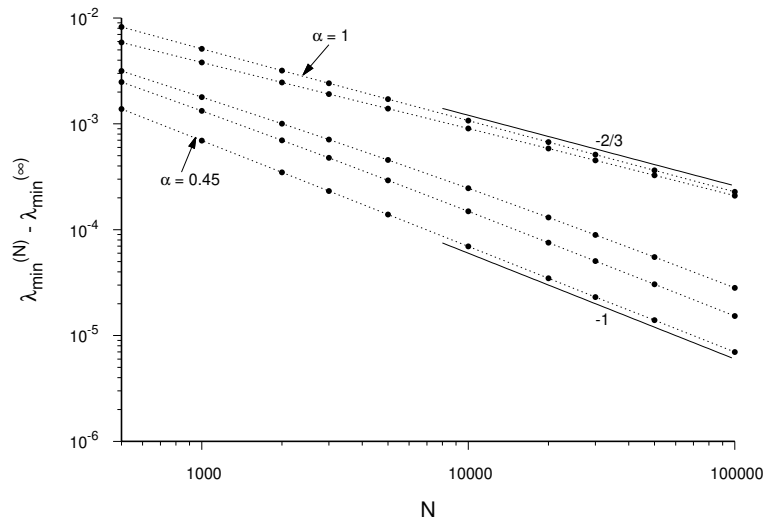


Figure 5.4: Difference between the finite-size slowest relaxation rate $\lambda_{\min}^{(N)}$ and its infinite-size limit value $\lambda_{\min}^{(\infty)}$ as a function of N (circles) for the balanced TASEP-LK ($\Omega = 0.1$) with $\beta = 0.1$ and different α values, both above and below the critical threshold $\alpha_c \approx 0.54786$. Solid lines represent scaling functions, i.e. $\propto N^{-2/3}$ and $\propto N^{-1}$ respectively (see the text). Dotted lines are an eyeguide.

that are the densities after subtracting the non-uniform part of the bulk profile. In the steady state, they satisfy the following equations

$$r_n r_{n+1}' - r_{n-1} r_n' = \omega n (r_{n+1} - r_{n-1}) \quad n = 1, \dots, N, \quad (5.26)$$

with the boundary conditions

$$r_0 = p_0 = \alpha, \quad (5.27)$$

$$r_{N+1} = q_0 = (\beta + \Omega)'. \quad (5.28)$$

We now make an intuitive argument on this density profile, then we express it in a more formal manner. We expect the detrended profile to behave, at least in the HD (or LD) phase, as the density profile of an “effective” pure TASEP. Under this assumption, the difference $r_{n+1} - r_{n-1}$ would be significantly different from zero only up to finite n , but, in this region, the prefactor ωn vanishes because the Langmuir kinetics rate scales as the inverse of the size for large N . Thus, the whole right-hand side of (5.26) is almost equal to zero and consequently

$$r_n r_{n+1}' \approx \text{constant} \quad n = 0, 1, \dots, N, \quad (5.29)$$

the detrended densities satisfy the pure TASEP mean-field equations (see (2.9) with $\omega_A = \omega_D = 0$) with the rescaled right boundary condition (5.28). The physical

meaning of this assumption is the following: the variations of the density of order 1 take place practically over a finite number of sites, where the effect of Langmuir kinetics becomes negligible for large N . On this region, the system should mimic a pure TASEP with a bulk density adjusted in order to match the local bulk density of the TASEP-LK. In the HD phase, the density variations are concentrated on the left side, thus the effective pure TASEP has the right boundary condition renormalized to the left boundary value of the bulk solution, that is $q_0 = (\beta + \Omega)'$. With the adjective “effective”, we mean that the uniform current of the TASEP is replaced by the local current value $q_0 q_0'$. We show an example of this property in figure 5.5, where we plot two different stationary density profiles, one for the pure TASEP and one for the TASEP-LK, computed numerically by (5.1), with the same α value, but two different β values, chosen in order to give the same q_0 . We see that, in the

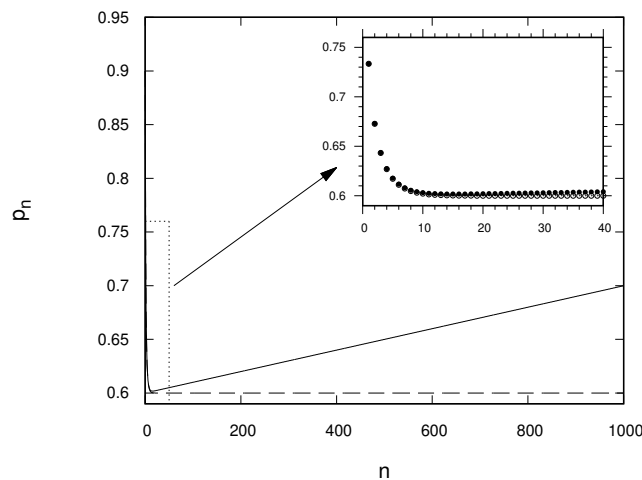


Figure 5.5: Steady-state local density p_n as a function of the node index n for the TASEP-LK ($\Omega = 0.1$, $\beta = 0.3$, $\alpha = 0.9$; solid line and solid circles) and for the pure TASEP ($\Omega = 0$, $\beta = 0.4$, $\alpha = 0.9$; dashed line and empty circles). In both cases it turns out $q_0 = 0.6$, the system size is $N = 1000$.

vicinity of the boundary layer, the two profiles are almost indistinguishable, whereas the effect of Langmuir kinetics can be clearly appreciated at a macroscopic length scale, yielding a linear density profile. We have evidence that this property may be exact: in figure 5.6, we do the same comparison with density profiles obtained by KMC simulations.

Still at the mean-field level, in a more formal derivation, we study an infinite sequence $(s_n)_{n=0}^{\infty}$ being a solution of the TASEP mean-field equations with bulk density q_0 , namely

$$s_n s_{n+1}' = q_0 q_0' \quad n = 0, 1, 2, \dots \quad (5.30)$$

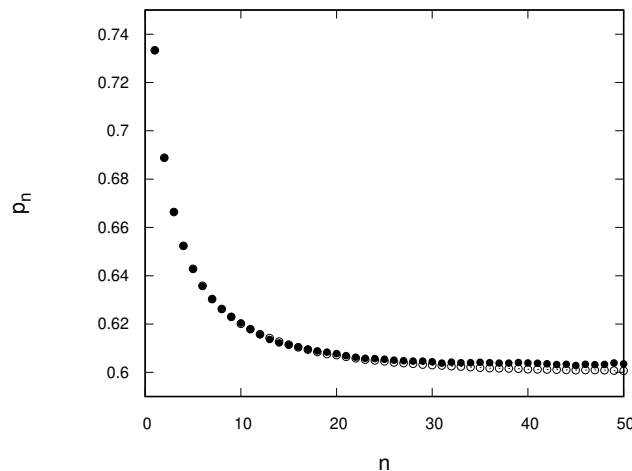


Figure 5.6: The same comparison as in figure 5.5, but the density profiles are obtained by KMC simulations.

This is a discrete Riccati equation [37]: the right-hand side takes into account that, in the bulk, we expect $s_n \approx q_0$ and the left-boundary condition is chosen according to (5.27), so that

$$s_0 = \alpha. \quad (5.31)$$

The sequence s_n represents the mean-field density profile for a TASEP with current $q_0 q_0'$, in the large N limit we expect to have

$$s_n \approx r_n \quad n = 0, \dots, N + 1. \quad (5.32)$$

We state the analytical properties of this sequence in Lemma 1, then we present our results on the bounds for the distance between s_n and the detrended densities r_n in Theorem 1, which is proved in section B.1.1 of appendix B. We rewrite the parameter bounds (2.12), (2.13) and the definition of x_o (5.11) using the expression of q_0

$$1 - \Omega > q_0 > 1/2, \quad (5.33)$$

$$\alpha > q_0', \quad (5.34)$$

$$\frac{1}{x_o} \equiv 2\sqrt{q_0 q_0'}. \quad (5.35)$$

The following lemma states that equation (5.30) with the initial condition (5.31) can be written in closed form as q_0 plus a correction that decays exponentially in n and defines the properties of the sequence $(s_n)_{n=0}^\infty$.

Lemma 1. Let $(s_n)_{n=0}^\infty$ be the infinite sequence defined as follows

$$s_n \equiv q_0 + (q_0 - q_0') \left[\left(1 - \frac{\alpha - q_0}{\alpha - q_0'} \gamma^n \right)^{-1} - 1 \right] \quad n = 0, 1, 2, \dots, \quad (5.36)$$

where

$$\gamma \equiv \frac{q_0'}{q_0}. \quad (5.37)$$

Then the following statements hold:

(i) the sequence $(s_n)_{n=0}^\infty$ satisfies (5.30), (5.31) and

$$\lim_{n \rightarrow \infty} s_n = q_0; \quad (5.38)$$

(ii) if $\alpha \geq q_0$ (resp. $\alpha \leq q_0$), then $(s_n)_{n=0}^\infty$ is non-increasing (resp. non-decreasing);

(iii) the sequence defined by (5.14) coincides with $(s_n)_{n=0}^\infty$.

A crucial point to prove statements (i) and (ii) is that the bounds for the model parameters (2.11) and (5.33) entail

$$0 < \gamma < 1. \quad (5.39)$$

Statement (iii) immediately descends from (5.35). We observe that the recursion (5.14) is exactly the same as that reported in [5], where the mean-field approximation of the TASEP was discussed.

Theorem 1. Let $(r_n)_{n=0}^{N+1}$ be the sequence of detrended densities defined above with boundary values $r_0 = \alpha$ and $r_{N+1} = q_0$, let $(s_n)_{n=0}^\infty$ and γ be defined according to Lemma 1. Then there exist suitable positive constants C^2 such that:

$$|s_n - r_n| \leq \begin{cases} C\gamma^N & \text{if } \Omega = 0 \\ C\frac{n^2\gamma^n}{N} & \text{if } \Omega > 0 \end{cases} \quad n = 0, \dots, N + 1. \quad (5.40)$$

These results allow us to state that the stationary density profile of the HD phase is

$$p_n = r_n + \omega n \approx s_n + \omega n \quad n = 0, \dots, N + 1. \quad (5.41)$$

²By *constant* we mean a finite real number independent of the node label n and of the system size N , but possibly dependent on the model parameters. For each occurrence of the symbol C , it is understood that there exists a suitable positive constant verifying the relation where the symbol appears.

A first consequence of Theorem 1 is that the steady-state current profile in the $N \rightarrow \infty$ limit is very close to the current profile corresponding to the bulk solution alone (we can call it *bulk current*), i.e.

$$J_n = p_n p_{n+1}' \approx q_n q_{n+1}' \quad n = 0, \dots, N. \quad (5.42)$$

This in turn implies that the maximum current value is very close to its bulk value at the left boundary. These arguments are collected in the following

Corollary 1. *Let $(J_n)_{n=0}^N$ and $(q_n)_{n=0}^{N+1}$ be respectively the sequences of (steady-state) currents and bulk densities, defined above, and let γ be defined according to Lemma 1. Then, the following statements hold:*

$$|J_n - q_n q_{n+1}'| \leq \begin{cases} C\gamma^N & \text{if } \Omega = 0 \\ C\frac{(n+1)\gamma^n}{N} & \text{if } \Omega > 0 \end{cases} \quad n = 0, \dots, N, \quad (5.43)$$

$$|\max(J_n)_{n=0}^N - q_0 q_0'| \leq \begin{cases} C\gamma^N & \text{if } \Omega = 0 \\ CN^{-1} & \text{if } \Omega > 0 \end{cases}. \quad (5.44)$$

The proof of the corollary is reported in section B.1.2.

5.2.2 Relaxation rates

As we have seen in section 5.1, the relaxation rates coincide with the eigenvalues of a tridiagonal symmetric matrix, that we now call A . Using the definition of detrended densities (5.25), we can rewrite the diagonal terms a_n , given by eq. (5.4), in the simpler form $r_{n+1}' + r_{n-1}$. The linear operator corresponding to this matrix maps the vector $u \equiv (u_1, \dots, u_N)$ to $Au \equiv (Au_1, \dots, Au_N)$ and is defined componentwise as

$$Au_n \equiv (r_{n+1}' + r_{n-1})u_n - \sqrt{p_n p_{n+1}'}u_{n+1} - \sqrt{p_{n-1} p_n'}u_{n-1}, \quad (5.45)$$

where $u_0 \equiv u_{N+1} \equiv 0$. The mean-field slowest relaxation rate is the smallest eigenvalue, which here we shall simply denote by λ . In this section we present the results of our investigation about the asymptotic value of λ in the infinite size limit and we provide bounds for its scaling behavior at large N .

Our starting point is to estimate λ by considering the smallest eigenvalue μ of a simplified matrix B , where we replace the detrended densities r_n with their infinite size approximation s_n in the diagonal terms and the currents $p_n p_{n+1}'$ with the corresponding bulk currents $q_n q_{n+1}'$ in the off-diagonal terms. The associated linear operator maps $u \equiv (u_1, \dots, u_N)$ to $Bu \equiv (Bu_1, \dots, Bu_N)$ and is defined by

$$Bu_n \equiv (s_{n+1}' + s_{n-1})u_n - \sqrt{q_n q_{n+1}'}u_{n+1} - \sqrt{q_{n-1} q_n'}u_{n-1}, \quad (5.46)$$

still with $u_0 \equiv u_{N+1} \equiv 0$. The eigenvalues of matrix B are still all real, because it is symmetric as well as A . Moreover, there is a small change from the original matrix to the simplified one and we can expect that this should also moderately affect the spectrum. Considering the smallest eigenvalue, we can determine bounds for the distance between λ and μ , which descend from Theorem 1 and Corollary 1.

Corollary 2. *Let λ and μ be the smallest eigenvalues of matrices A and B , respectively, and let γ be defined according to Lemma 1. Then*

$$|\lambda - \mu| \leq \begin{cases} C\gamma^N & \text{if } \Omega = 0 \\ CN^{-1} & \text{if } \Omega > 0 \end{cases}. \quad (5.47)$$

On the one hand, this can be regarded as a technical result, because, considering matrix B , we are simplifying the eigenvalue problem. On the other hand, the structure of the simplified matrix and the related results for the smallest eigenvalue reveal that the dynamical transition is driven by the competition between the boundary layer (diagonal terms) and the bulk (off-diagonal terms). In the pure TASEP case the bulk profile is uniform, thus the only deviation from the Toeplitz structure arises from the diagonal terms, as observed in [1].

On the basis of Corollary 2, we focus on μ in order to investigate the leading behavior of λ at large N : we want to find suitable upper- and lower-bounds for this eigenvalue, which may tend to coincide in the infinite size limit.

Using the *Courant minimax principle*, one can determine upper-bounds in the form $\mu \leq (u, Bu)$, for any vector $u \in \mathbb{R}^N$ such that $\|u\| = 1$, where $(u, v) \equiv \sum_{n=1}^N u_n v_n$ is the usual Euclidean scalar product and $\|u\| \equiv \sqrt{(u, u)}$ the corresponding norm. Thus, by equation (5.46), we directly prove the following Lemma, that we call *Courant-type bound*.

Lemma 2. *Let μ be the smallest eigenvalue of matrix B and let u_1, \dots, u_N be real numbers such that $\sum_{n=1}^N u_n^2 = 1$. Then*

$$\mu \leq 1 - \sum_{n=1}^N (s_{n+1} - s_{n-1}) u_n^2 - 2 \sum_{n=1}^{N-1} \sqrt{q_n q_{n+1}'} u_n u_{n+1}. \quad (5.48)$$

Determining lower-bounds is more difficult, our way to proceed is inspired by the *Gershgorin circle theorem*'s, which allows us to formulate the following Lemma, called *Gershgorin-type bound* (see appendix B.2.3).

Lemma 3. *Let μ be the smallest eigenvalue of matrix B and let w_0, \dots, w_{N+1} be real positive numbers (except w_0 and w_{N+1} , possibly being zero). Then*

$$\mu \geq 1 - \max_{n=1} \left(s_{n+1} - s_{n-1} + \frac{w_{n+1} + w_{n-1}}{2x_n w_n} \right)^N. \quad (5.49)$$

The difficulties encountered in applying the strategy outlined above depend strongly on the boundary conditions for the detrended densities, which we recall to be $r_0 = \alpha$ on the left (eq. (5.27)) and $r_{N+1} = q_0$ on the right (eq. (5.28)). By Lemma 1, we realize that the case $\alpha \geq q_0$ is much simpler than the complementary one, because for this set of α values the sequence $(s_n)_{n=0}^\infty$ is non-increasing, so that $s_{n+1} - s_{n-1}$ can never be positive. Thus, applying Lemma 3 with the simple choice $w_n \equiv 1$ for all n (which can be shown to coincide with the usual Gershgorin theorem), we easily obtain the following result.

Lemma 4. *Let μ be the smallest eigenvalue of matrix B . If $\alpha \geq q_0$, then*

$$\mu \geq 1 - \frac{1}{x_\circ}. \quad (5.50)$$

As far as the upper-bounds are concerned, choosing suitably u_1, \dots, u_N in Lemma 2, we can prove the following (see B.2.3 for the details).

Lemma 5. *Let μ be the smallest eigenvalue of matrix B . Then*

$$\mu \leq 1 - \frac{1}{x_\circ} + \begin{cases} CN^{-2} & \text{if } \Omega = 0 \\ CN^{-2/3} & \text{if } \Omega > 0 \end{cases}. \quad (5.51)$$

At odds with Lemma 4, the latter bound holds in principle for all $\alpha > q_0'$, which is required in order to stay within the HD phase region. However, when $\alpha < q_0$, it may no longer be a good one.

We now concentrate on this second more difficult case $\alpha < q_0$: in order to obtain good bounds, we have to choose u_n in Lemma 2 (Courant-type bound) and w_n in Lemma 3 (Gershgorin-type bound) as close as possible to the actual eigenvector. Moreover, to treat analytically the eigenvalue problem for matrix B , we have to get rid of the size dependence. We recall the bulk-density expression $q_n = q_0 + \omega n$ and we observe that, if $n \ll N$, we have $q_n \approx q_0$ (and consequently $q_n q_{n+1}' \approx q_0 q_0'$) independently of n . Equivalently we can say that, if we increase the system size but we only take the elements of matrix B up to row and column indices remaining much smaller than N , the off-diagonal entries tend to be constant, approaching the value $-\sqrt{q_0 q_0'}$. Keeping in mind this argument, from (5.46) along with (5.35) we expect that, for large N and $n \ll N$, the eigenvector components v_n satisfy the following equation

$$2x_\circ (s_{n+1} - s_{n-1}) v_n + v_{n+1} + v_{n-1} \propto v_n, \quad (5.52)$$

with $v_0 = 0$. The latter equation no longer depends on the system size. Actually, we expect it to become more and more accurate with increasing N , even though only as far as $n \ll N$. Therefore, we study the properties of a sequence $(v_n)_{n=0}^\infty$ satisfying (5.52), as a function of the proportionality coefficient. Such a sequence

can be defined by recursion, with the initial conditions $v_0 = 0$ (by hypothesis) and an arbitrary v_1 (for instance $v_1 = 1$). Thinking of the Gershgorin-type and the Courant-type bounds, we are interested respectively in the hypotheses under which the sequence never changes sign and whether it goes to zero rapidly enough. Its relevant properties are stated in the following

Lemma 6. *Let $(s_n)_{n=0}^\infty$ be the sequence defined by (5.14) (or equivalently Lemma 1), in the hypothesis $\alpha < q_0$, and let $(v_n(x))_{n=0}^\infty$ be the family of sequences defined by (5.15) and (5.16), parameterized by $x \in \mathbb{R}$. Then the following statements hold.*

- (i) *The sequence $(v_n(x))_{n=0}^\infty$ is nonoscillatory (i.e. eventually positive or eventually negative) if and only if $x \geq 1$.*
- (ii) *The set \mathcal{X} of real numbers x such that $v_n(x) > 0$ for all $n > 0$ is a closed, infinite interval $\mathcal{X} = [x_*, \infty)$, where $x_* \equiv \inf \mathcal{X} \in [1, x_0)$.*
- (iii) *Let $\zeta : [1, \infty) \rightarrow (0,1]$ be the function defined by (5.13) and let $f_n : [1, \infty) \rightarrow \mathbb{R}$ be the functions defined as*

$$f_n(x) \equiv 2x_0 \sum_{k=0}^n (s_{k+1} - s_{k-1}) v_k(x) \zeta(x)^k \quad n = 0, 1, 2, \dots \quad (5.53)$$

(with an arbitrary definition of s_{-1}). Then the limit

$$f(x) \equiv \lim_{n \rightarrow \infty} f_n(x) \quad (5.54)$$

exists and is finite for all $x \geq 1$. Moreover, if the sequence $(v_n(x))_{n=0}^\infty$ is eventually positive (resp. eventually negative), then $f(x) \leq 1$ (resp. $f(x) \geq 1$).

- (iv) *If $x_* > 1$, then $f(x_*) = 1$.*
- (v) *If $x_* > 1$, then $v_n(x_*) \leq C\zeta(x_*)^n$ for all n .*

According to statement (ii), we can choose $w_n = v_n(x)$ in the Gershgorin-type bound (Lemma 3), for all $x \in \mathcal{X}$. Moreover, from (5.16), it follows that the most restrictive bound is attained for the smallest x value. Thus, we obtain

Lemma 7. *Let μ be the smallest eigenvalue of matrix B , and let x_* be defined as in Lemma 6. If $\alpha < q_0$, then*

$$\mu \geq 1 - \frac{x_*}{x_0}. \quad (5.55)$$

The following result provides a stronger upper bound than Lemma 5 for $\alpha < q_0$.

Lemma 8. *Let μ be the smallest eigenvalue of matrix B , and let x_* and $\zeta(x)$ be defined as in Lemma 6. If $\alpha < q_0$ and $x_* > 1$, then*

$$\mu \leq 1 - \frac{x_*}{x_0} + \begin{cases} C\zeta(x_*)^{2N} & \text{if } \Omega = 0 \\ CN^{-1} & \text{if } \Omega > 0 \end{cases}. \quad (5.56)$$

The proof is based on statement (v) of Lemma 6 and is reported in detail in appendix B.2.5. As was mentioned above, for $\alpha < q_0$ the bound stated by Lemma 5 is still valid but, as soon as α drops below the critical threshold α_c (so that $x_* > 1$), this is no longer a good bound, as Lemma 8 turns out to be stronger. This corresponds to the slow phase, where the (infinite-size) relaxation rate depends on α and gets smaller than its plateau value.

Finally, using the results obtained so far, we can prove the following theorem for the eigenvalue λ , which is the physical quantity of interest.

Theorem 2. *Let λ be the smallest eigenvalue of matrix A , and let x_* and $\zeta(x)$ be defined as in Lemma 6. Either if $\alpha \geq q_0$, or if $\alpha < q_0$ with $x_* = 1$, then*

$$\left| \lambda - 1 + \frac{1}{x_o} \right| \leq \begin{cases} CN^{-2} & \text{if } \Omega = 0 \\ CN^{-2/3} & \text{if } \Omega > 0 \end{cases}. \quad (5.57)$$

Otherwise, if $\alpha < q_0$ with $x_* > 1$, then

$$\left| \lambda - 1 + \frac{x_*}{x_o} \right| \leq \begin{cases} C\zeta(x_*)^{2N} & \text{if } \Omega = 0 \\ CN^{-1} & \text{if } \Omega > 0 \end{cases}. \quad (5.58)$$

There are two main steps to prove this theorem. First, using Lemmas 4, 5, 7 and 8, we can prove an analogous theorem for μ . Then, Corollary 2 allows one to extend the result from μ to λ , using the property that the distance between μ and λ is, for $N \rightarrow \infty$, infinitesimal of a higher order (or at most of the same order) than the distance between λ and its limit value. In the pure TASEP case, this requirement implies the inequality $\zeta(x_*)^2 \geq \gamma$, which we prove below. Using (5.37) and (5.35), by simple algebra we obtain

$$\gamma = \zeta(x_o)^2. \quad (5.59)$$

Since $\zeta(x) > 0$ for all $x \geq 1$, the previous inequality becomes $\zeta(x_*) \geq \zeta(x_o)$. Then, considering that $\zeta(x)$ is monotonically decreasing, this condition holds for $x_* \leq x_o$, which is guaranteed by Lemma 6, statement (ii).

We note that statements (i), (iii) and (iv) in Lemma 6 are not directly involved in the proof of Theorem 2: (i) is a basic step for proving Lemma 6 itself, whereas (iii) and (iv) provide analytical tools for studying the behavior of x_* as a function of the model parameters and localizing the dynamical transition. In particular, we can formulate two criteria about the behaviour of $f(x)$.

Criterion 1. *If equation $f(x) = 1$ has no solution $x \in (1, x_o)$, then $x_* = 1$.*

Criterion 2. *If there exists $x \geq 1$ such that $f(x) > 1$, then $x_* > x$ and $f(x_*) = 1$.*

The first criterion is a direct consequence of statement (iv) and of the fact that, according to (ii), $x_* \in [1, x_o)$. It is applied to determine the parameter range where $x_* = 1$ (see sec. 5.2).

We sketch the proof of Criterion 2. According to statements (ii) and (iii), the condition $x \geq x_*$ implies $x \in \mathcal{X}$ and thence $f(x) \leq 1$. Therefore, by complementarity, $f(x) > 1$ implies $x < x_*$. Since $x \geq 1$ by hypothesis, the fact that $f(x_*) = 1$ follows directly from statement (iv).

In the special case $x = 1$, the second criterion states that $f(1) > 1$ implies $x_* > 1$. This fact is used to determine the parameter range where the latter condition holds (see sec. 5.2), whereas the precise x_* value is determined by solving numerically $f(x_*) = 1$.

In figure 5.2 we observed that for certain parameter values this last equation turns out to have two solutions. Criterion 2 allows us to rule out the spurious one, that can be denoted by \tilde{x}_* , because in such cases we observe the occurrence of a range of x values larger than \tilde{x}_* verifying $f(x) > 1$.

5.3 The unbalanced case

We now study the case $\Omega_A \neq \Omega_D$, which can be reduced to $\Omega_A > \Omega_D$ for the particle-hole symmetry of the model (see section 2.2). Even if the phase diagram is no more symmetric with respect to the line $\beta = \alpha$, we concentrate on the HD phase, which is the most interesting one for the properties of the dynamical transition. We report the result derived in the hydrodynamic limit [15] for the bulk density profile, which can be written in terms of the real 0-th order branch of the Lambert W function

$$\rho(z) = l + \left(l - \frac{1}{2}\right) W_0 \left(\frac{\beta' - l}{l - \frac{1}{2}} \exp \frac{\beta' - l - \frac{1}{2}(\Omega_A + \Omega_D)z'}{l - \frac{1}{2}} \right), \quad (5.60)$$

where $z \in [0,1]$ is a continuous variable and the extrema of the interval correspond to the system boundaries. For fixed $\Omega_A > \Omega_D$, the HD phase region is defined by the following inequalities, which involve β and the left boundary value of the bulk density $\rho(0)$

$$\frac{1}{2} > \beta > 0, \quad (5.61)$$

$$\alpha > \rho(0)'. \quad (5.62)$$

Using the property $W_0(\xi e^\xi) = \xi$ for $\xi \geq -1$ and observing that (5.61) implies $(\beta' - l)/(l - 1/2) > -1$, one verifies that the right boundary condition $\rho(1) = \beta'$ is satisfied. The mismatch between $\rho(0)$ and $p_0 = \alpha$ gives rise to a boundary layer. For the unbalanced case we do not have an analytic bulk solution at finite N ,

nevertheless we can define it as a sequence $(q_n)_{n=0}^{N+1}$ satisfying the steady state equations (2.9)

$$q_n (q_{n+1}' + \omega_D) = (q_{n-1} + \omega_A) q_n', \quad n = 1, \dots, N, \quad (5.63)$$

with the boundary conditions

$$q_0 = \rho(0), \quad (5.64)$$

$$q_{N+1} = \rho(1) = \beta'. \quad (5.65)$$

Since the solution of the discrete boundary problem is unique [26], this sequence is well-defined and, in the large N limit, we expect that

$$q_n \approx \rho\left(\frac{n}{N+1}\right), \quad n = 0, \dots, N+1. \quad (5.66)$$

We proceed in analogy with the balanced case: we write the detrended densities

$$r_n \equiv p_n - (q_n - q_0), \quad n = 0, \dots, N+1, \quad (5.67)$$

with the boundary conditions

$$r_0 = p_0 = \alpha, \quad (5.68)$$

$$r_{N+1} = q_0. \quad (5.69)$$

We express equations (5.67) with respect to the local densities and we plug them into the steady state equations (2.9). For all $n = 1, \dots, N$, we have

$$\begin{aligned} q_n (q_{n+1}' + \omega_D) + r_n r_{n+1}' - (q_n - q_0) r_{n+1} - (r_n - q_0) (q_{n+1} - \omega_D) = \\ (q_{n-1} + \omega_A) q_n' + r_{n-1} r_n' - (q_n - q_0) r_{n-1} - (r_n - q_0) (q_{n-1} + \omega_A). \end{aligned} \quad (5.70)$$

Taking into account the steady state condition for the bulk sequence (5.63), we get

$$\begin{aligned} r_n r_{n+1}' - r_{n-1} r_n' = (q_n - q_0) (r_{n+1} - r_{n-1}) + \\ + (r_n - q_0) (q_{n+1} - q_{n-1} - \omega_A - \omega_D), \end{aligned} \quad (5.71)$$

still for $n = 1, \dots, N$. The argument about the behaviour of the detrended densities (see sec. 5.2.1) can be justified for this case as follows: we have clear numerical evidences that the local density p_n approaches exponentially the bulk solution, with the characteristic length of the exponential remaining finite as $N \rightarrow \infty$. Consequently, assuming that r_n tends to q_0 exponentially in n implies that the difference $r_{n+1} - r_{n-1}$ is significantly different from zero only up to finite n . In this region, the factor $q_n - q_0$ is of order $1/N$, because q_n can be viewed as the discretization (see eq. (5.66)) of the regular function $\rho(z)$. Also the term $q_{n+1} - q_{n-1} - \omega_A - \omega_D$, which is equal to zero in the balanced case, is of order $1/N$. Thus, the pure TASEP

mean-field equations (5.29) for the detrended densities are obtained. Here we do not restate the formal results about the sequence $(s_n)_{n=0}^\infty$, we recall that equation (5.30) can be written in closed form as

$$s_n = q_0 + e_n, \quad n = 0, 1, 2, \dots \quad (5.72)$$

where

$$e_n \equiv (q_0 - q_0') \left[\left(1 - \frac{\alpha - q_0}{\alpha - q_0'} \gamma^n \right)^{-1} - 1 \right] \quad n = 0, 1, 2, \dots \quad (5.73)$$

The parameter bound (5.61) entails that

$$0 < \gamma \equiv \frac{q_0'}{q_0} < 1, \quad (5.74)$$

thus the correction e_n vanishes as n tends to infinity. We conclude that the steady state density profile in the HD phase can be written as

$$p_n = q_n + r_n - q_0 \approx \rho \left(\frac{n}{N+1} \right) + e_n, \quad n = 0, \dots, N+1. \quad (5.75)$$

We retrace the main results of Corollary 1 in the unbalanced case. In the large N limit, the current profile of the system is very close to the current profile computed by the bulk solution alone: the difference between them for all $n = 0, \dots, N$, is given by

$$\begin{aligned} p_n p_{n+1}' - q_n q_{n+1}' &= (r_n r_{n+1}' - q_0 q_0') - (q_n - q_0)(r_{n+1} - q_0) + \\ &\quad - (q_{n+1} - q_0)(r_n - q_0). \end{aligned} \quad (5.76)$$

Recalling that $r_n \approx s_n$ for the same values of n , one can see that the first term on the right-hand side is negligible. Using the same arguments adopted for equation (5.71), also the remaining terms can be neglected. Thus, by the approximate equality (5.66) and the fact that the function $\rho(z)$ is regular, we can write

$$J_n = p_n p_{n+1}' \approx q_n q_{n+1}' \approx \rho \left(\frac{n}{N+1} \right) \rho' \left(\frac{n}{N+1} \right), \quad n = 0, \dots, N. \quad (5.77)$$

Keeping in mind that the current $\rho\rho'$ is decreasing for $\rho > 1/2$ and that the bulk density is always greater than this value in the HD phase, one can argue that the maximum current corresponds to the minimum bulk density. For $\beta < l'$, the maximum current is equal to $q_0 q_0'$ and occurs at the left boundary of the system, whereas for $\beta > l'$, $J_{\max} = \beta\beta'$ is found at the right boundary.

5.3.1 New features of the dynamical transition

To introduce the dynamical transitions in the unbalanced case, we describe the results obtained by solving numerically the eigenvalue problem (5.8) at finite size. The main new feature is that the low-lying eigenvalues exhibit two different behaviours for $\beta < l'$ and $\beta > l'$, in particular the second one is not observed in the balanced case. In section 2.2.2 we observed that these two regimes in the extraction rate (we can call them “low” and “high” beta regions) correspond respectively to increasing and decreasing bulk density profiles (see fig. 2.9). Furthermore, in the previous section we noted that, changing from the low to the high beta regions, the position of the maximum current value moves from the left to the right boundary. As one can see from figure 5.7, the case $\beta < l'$ is qualitatively similar to the balanced case and the pure TASEP one (figure 2.3). Apart from the smallest one, the low-lying eigenvalues form a nearly “flat band”, meaning that they are practically independent of α . The slowest relaxation rate increases with α and, at a critical value of the injection rate, it reaches a maximum and becomes almost constant. In the $N \rightarrow \infty$ limit, which is denoted by a thick black line, it is constant and the transition is characterized by a discontinuity in the second derivative.

A new scenario is observed for $\beta > l'$: looking at figure 5.8, we see that the smallest

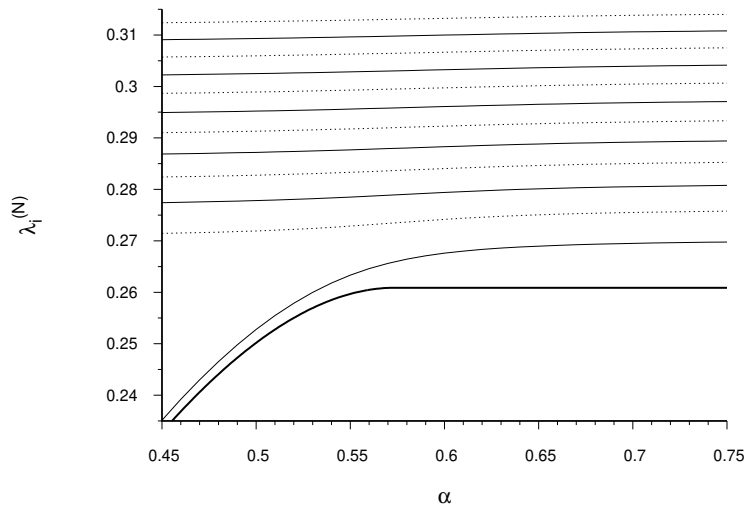


Figure 5.7: Thin lines represent the smallest 12 eigenvalues of the relaxation matrix computed numerically for $N = 300$, $\beta = 0.1$, $\Omega_A = 0.3$ and $\Omega_D = 0.1$ as a function of α . Eigenvalues of increasing magnitude are alternately displayed by solid and dotted lines. The thick solid line represents the infinite size limit of the slowest relaxation rate (5.80).

eigenvalue does not saturate in a smooth way as before and a sequence of crossings occurs through the spectrum. Actually, by examining the results on a sufficiently

small scale (as in figure 5.9), one realizes that the apparent degeneracies are indeed *avoided crossings*. The smallest eigenvalue exhibits a very sharp slope change as a function of the injection rate, whereas a number of higher eigenvalues have two subsequent slope changes (of decreasing abruptness for eigenvalues of increasing order). In the infinite size limit, the slowest relaxation rate becomes discontinuous in the first derivative. In figure 5.9 we observe that also the confinement of the slowest relaxation mode changes at the dynamical transition. We show the components of the eigenvector corresponding to the smallest eigenvalue for two values of α in the slow and in the fast phase respectively, very close to the dynamical transition. The eigenvector has components significantly different from zero on both boundaries, but we can see that in the slow phase they are mostly on the left side, whereas in the fast phase the eigenvector tends to be confined to the right boundary.

We write the left boundary value of the bulk density according to equation (5.60)

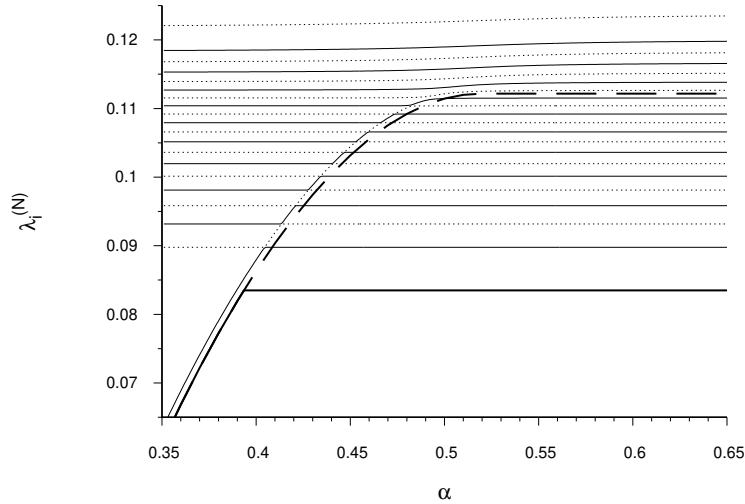


Figure 5.8: Thin lines represent the smallest 20 eigenvalues of the relaxation matrix computed numerically for $N = 300$, $\beta = 0.3$, $\Omega_A = 0.3$ and $\Omega_D = 0.1$ as a function of α . They are alternately displayed by solid and dotted lines. The thick solid line represents the $N \rightarrow \infty$ limit of the slowest relaxation rate defined by (5.82), the thick dashed line corresponds to the definition of the slowest relaxation rate for $\beta < l'$, i.e. eq. (5.80). As can be seen in the figure, this curve follows the series of avoided crossings.

$$q_0(\beta, \Omega_A, \Omega_D) = l + \left(l - \frac{1}{2}\right) W_0 \left(\frac{\beta' - l}{l - \frac{1}{2}} \exp \frac{\beta' - l - \frac{1}{2}(\Omega_A + \Omega_D)}{l - \frac{1}{2}} \right), \quad (5.78)$$

it corresponds to the intercept of the dashed lines with the vertical axis $n = 0$ in figure 2.9.

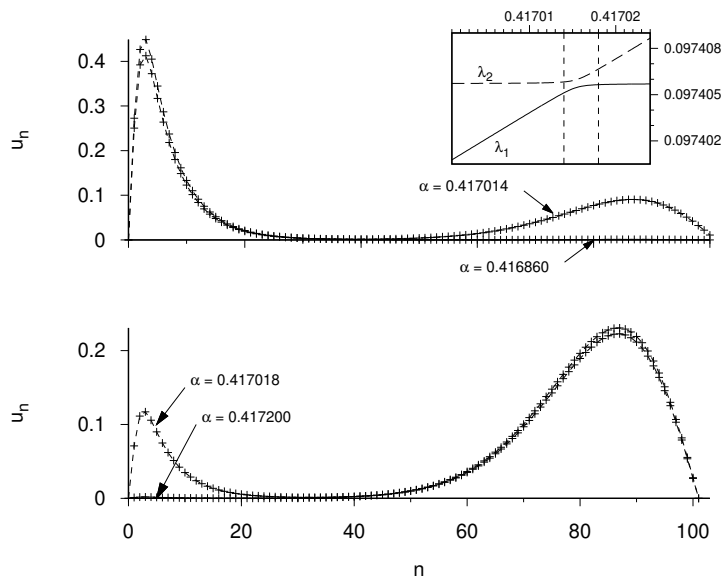


Figure 5.9: Components of the eigenvector corresponding to the smallest eigenvalue for $N = 100$, $\beta = 0.3$, $\Omega_A = 0.3$ and $\Omega_D = 0.1$, at two α values very close to $\tilde{\alpha}_c$. Slow phase: top panel. Fast phase: bottom panel. The eigenvector has components significantly different from zero on both boundaries, but in the slow phase they are mostly on the left side, whereas in the fast phase the confinement moves to the right end.

For this case, the asymptotic expression for the slowest relaxation rate is given by

$$\lambda_{\min}^{(\infty)} = 1 - 2 \max \left\{ x_* \sqrt{q_0 q_0'}, \sqrt{\beta \beta'} \right\}. \quad (5.79)$$

Looking at eqs. (5.12), (5.14), (5.15) and (5.16), we observe that the model parameters β , Ω_A and Ω_D get into the theory only through the quantities $\beta \beta'$ and $q_0 q_0'$, that are the right- and left-boundary currents in the infinite size limit. Of course equations (5.17)-(5.19) hold also in the unbalanced case, provided the different expression for q_0 .

For $\beta < l'$ the bulk density profile has a positive slope, thus $\beta' > q_0$. These two quantities are both greater than $1/2$, because we are in the HD phase, thence $q_0 q_0' > \beta \beta'$. Since $x_* \geq 1$, from equation (5.79) it follows that

$$\lambda_{\min}^{(\infty)} = 1 - 2x_* \sqrt{q_0 q_0'}. \quad (5.80)$$

This is equivalent to equation (5.10) and is denoted by a thick solid line in figure 5.7: in this portion of the HD phase region, the behaviour of $\lambda_{\min}^{(\infty)}$ as a function of the injection rate is only governed by x_* , which has no discontinuity in the α variable as in the balanced case.

In the second regime ($\beta > l'$), the slope of the bulk density profile becomes negative, thus all the inequalities are reversed and $q_0 q_0' < \beta \beta'$. We know that x_* decreases upon increasing α up to α_c , where it becomes equal to 1 and remains constant. As a consequence, there must exist another threshold value $\tilde{\alpha}_c < \alpha_c$, such that $x_* \sqrt{q_0 q_0'} < \sqrt{\beta \beta'}$ for $\alpha > \tilde{\alpha}_c$. This new threshold is computed by the equation

$$f\left(\sqrt{\frac{\beta \beta'}{q_0 q_0'}}; \tilde{\alpha}_c, q_0\right) = 1, \quad (5.81)$$

from which one can argue that $\tilde{\alpha}_c(q_0, \beta)$ and $\alpha_c(q_0)$ coincide when $\beta = l' = q_0'$, corresponding to a flat bulk profile on the value of the equilibrium Langmuir density. The transition in $\lambda_{\min}^{(\infty)}$ exhibits a discontinuity in the first derivative at $\alpha = \tilde{\alpha}_c$, as one can see from figure 5.8 (the infinite size limit (5.79) of the slowest relaxation rate is denoted by a thick solid line), and has no analogue in the balanced case. In the same figure we also observe that the expression (5.80), which is denoted by a thick dashed line, follows the series of avoided crossings. This indicates that the relaxation mode is carried on by the subsequent eigenvalues in the low lying part of the spectrum.

In figure 5.10 we show the dynamical subphases of the HD phase region: the first

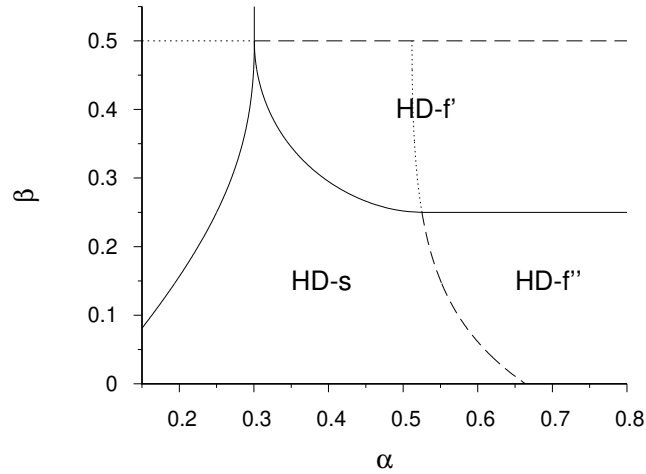


Figure 5.10: Cut of the phase diagram in the $\alpha - \beta$ plane (HD phase region) for $\Omega_A = 0.3$ and $\Omega_D = 0.1$. Thick lines denote static transitions, whereas thin lines denote dynamical transitions. The dynamical transition at “low-betas” is denoted by a dashed line and its continuation for $\beta > l'$ by a dotted line, the thin solid line denotes the first-order like dynamical transition.

distinction is between the HD-s (slow) phase, where $\lambda_{\min}^{(\infty)}$ depends on the injection rate, and the HD-f (fast) phase, where the slowest relaxation rate is independent

of α and takes the highest possible value at a given β , that is

$$\lambda_{\min}^{(\infty)} = 1 - 2 \max \left\{ \sqrt{q_0 q_0'}, \sqrt{\beta \beta'} \right\}. \quad (5.82)$$

For $\beta = l' = q_0'$ the latter expression exhibits a singularity in the first derivative (we can call it first-order), thus we can say that there is a new type of dynamical transition. For this reason, we further subdivide the HD-f region into HD-f' and HD-f". We denote the dynamical transition lines corresponding to first- ($\tilde{\alpha}_c(\beta)$) and second-order ($\alpha_c(\beta)$) singularities by solid and dashed lines respectively. In figure 5.10 we have also reported the continuation of the second order line for $\beta > l'$, denoted by a dotted line. It is not correct to say that this line represents a dynamical transition, because it is unrelated to the slowest relaxation rate. Nevertheless, it contains some extra information about the spectrum, since it can be loosely considered as a border line for the region of avoided crossings.

We verified numerically that the difference $\lambda_{\min}^{(N)} - \lambda_{\min}^{(\infty)}$ scales as a power law with the same exponents (1 in the slow phase and 2/3 in the fast phase) as in the balanced case. In figure 5.11 we show an example for $\beta = 0.1$ which is qualitatively similar to what is observed in figure 5.4. In figure 5.12 we consider an example in the high beta region ($\beta = 0.3$): we observe that the multiplying constant decreases with α in the slow phase, whereas the points in the fast phase are coincident at large N . In between we can see a crossover regime: the curves corresponding to $\alpha = 0.395$ and $\alpha = 0.4$ deviate from the power law scaling at small sizes.

We now try to provide a formal derivation of the asymptotic values for the slowest relaxation rate presented above. We recall the eigenvalue problem (5.8) for the relaxation matrix

$$Au_n \equiv a_n u_n - \sqrt{p_n p_{n+1}'} u_{n+1} - \sqrt{p_{n-1} p_n'} u_{n-1}, \quad n = 1, \dots, N$$

where a_n is defined by (5.4) and $u_0 \equiv u_{N+1} \equiv 0$. In appendix B.3 we derive upper and lower bounds for the mean-field slowest relaxation rate $\lambda_{\min}^{(N)}$, which become tight in the infinite size limit. To find suitable upper bounds, we resort again to the *Courant minimax principle*

$$\lambda_{\min}^{(N)} \leq (u, Au), \quad (5.83)$$

for any vector $u \in \mathbb{R}^N$ with unitary norm. From (5.8) we write

$$(u, Au) = \sum_{n=1}^N a_n u_n^2 - 2 \sum_{n=1}^{N-1} \sqrt{J_n} u_n u_{n+1}. \quad (5.84)$$

Expressing the local density by (5.67) and plugging this into the definition of the diagonal term, we have

$$a_n = 1 - (r_{n+1} - r_{n-1}) - (q_{n+1} - q_{n-1} - \omega_A - \omega_D). \quad (5.85)$$

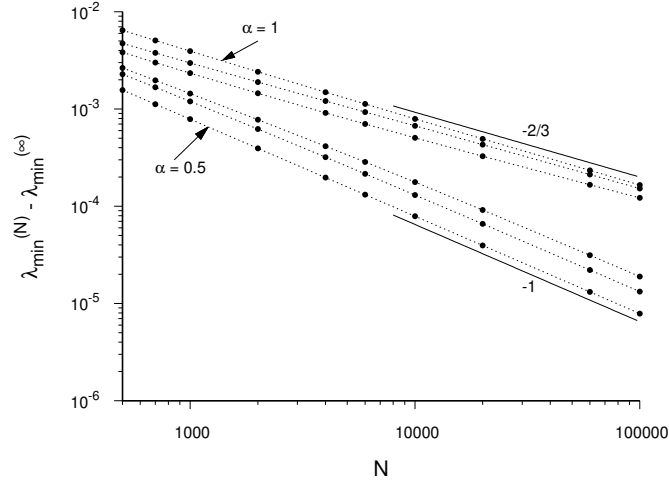


Figure 5.11: Difference between the finite-size slowest relaxation rate $\lambda_{\min}^{(N)}$ and its infinite-size limit value $\lambda_{\min}^{(\infty)}$ as a function of N (circles) for the unbalanced TASEP-LK ($\Omega_A = 0.3$, $\Omega_D = 0.1$) with $\beta = 0.1$ and different α values, both above and below the critical threshold $\alpha_c \approx 0.57368$. Solid lines represent scaling functions, i.e. $\propto N^{-2/3}$ and $\propto N^{-1}$ respectively (see the text). Dotted lines are an eyeguide.

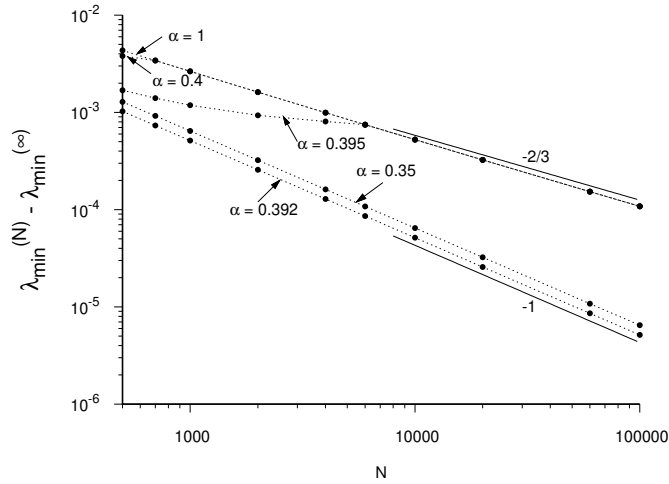


Figure 5.12: Difference between the finite-size slowest relaxation rate $\lambda_{\min}^{(N)}$ and its infinite-size limit value $\lambda_{\min}^{(\infty)}$ as a function of N (circles) for the unbalanced TASEP-LK ($\Omega_A = 0.3$, $\Omega_D = 0.1$) with $\beta = 0.3$ and different α values, both above and below the critical threshold $\alpha_c \approx 0.39345$. Solid lines represent scaling functions, i.e. $\propto N^{-2/3}$ and $\propto N^{-1}$ respectively (see the text). Dotted lines are an eyeguide.

In the quadratic form (u, Au) , there are terms vanishing for $N \rightarrow \infty$: we can neglect the last term in (5.85), then the detrended densities r_n can be replaced by s_n . Thus, we can write

$$a_n \approx 1 - (s_{n+1} - s_{n-1}) \quad (5.86)$$

and therefore

$$(u, Au) \approx 1 - \sum_{n=1}^N (s_{n+1} - s_{n-1}) u_n^2 - 2 \sum_{n=1}^{N-1} \sqrt{J_n} u_n u_{n+1}. \quad (5.87)$$

In this case we do not write formal bounds at finite N as we did for the balanced case, nevertheless all the approximate inequalities have been verified numerically. As far as the lower bounds are concerned, we use the same approach inspired by the *Gershgorin's circle theorem* that was adopted for the balanced case. In doing so, we distinguish three cases of increasing complexity in the parameter values, the details are given in appendix B.3.

Chapter 6

Complementary results for the TASEP-LK

In this chapter we investigate the dynamical transitions in the TASEP-LK using two complementary approaches: one method is the modified Domain Wall Theory (mDWT) introduced in chapter 3, the other one is to compute the exact finite size slowest relaxation rate as described in section 4.2 and then extrapolate the results to the infinite size limit with the Bulirsch-Stoer (BST) algorithm, explained in section 4.3. We present numerical evidences for the two dynamical transitions and we make conjectures about the exactness of the mDWT for this model and about the scaling exponent of the slowest relaxation rate: the results show a good agreement between the mDWT predictions and the extrapolated points both in the low and high beta regions. From our observations we have also evidence that the scaling exponent $2/3$ found for the mean-field slowest relaxation rate in the fast phase may be exact and unique as for pure TASEP.

6.1 mDWT for the TASEP-LK

We reformulate the mDWT introduced in chapter 3 in order to apply it to the TASEP-LK. In this context, the quantities $\rho_{L,R}$ denote the densities of the left/right domains separated by the wall: for the TASEP they coincide with the boundary densities, but for the TASEP-LK the bulk is no longer constant and different identifications are required. The relaxation rate λ_{DWT} given by (3.10) can be rewritten by introducing the domain wall function

$$F(\rho_L, \rho_R) = \frac{\left(\sqrt{J(\rho_L)} - \sqrt{J(\rho_R)}\right)^2}{\rho_R - \rho_L}. \quad (6.1)$$

In the mDWT we take $F(\rho_L, \rho_R)$ in the slow phase and the maximum rate in the fast phase ($\rho_L \geq \rho_L^c(\rho_R)$), thus we define the function

$$G(\rho_L, \rho_R) = \begin{cases} F(\rho_L, \rho_R), & \rho_L < \rho_L^c(\rho_R) \\ F(\rho_L^c(\rho_R), \rho_R), & \rho_L \geq \rho_L^c(\rho_R) \end{cases} \quad (6.2)$$

Now we consider the TASEP-LK with Ω_A and Ω_D fixed. For $\beta < 1 - l$, the wall is between the densities $\rho_L = \alpha$ and $\rho_R = q_0$. The reason for this choice is that, looking at the dynamics close to the steady state, the density immediately on the right of the wall is q_0 (an example is given in figure 6.1). The same holds in the balanced case for $0 < \beta < 1/2 - \Omega$, where $q_0 = (\beta + \Omega)'$. For $\beta > 1 - l$, previous mean-field results suggest that an important role is played by the right boundary and that the slowest relaxation rate should be determined by the minimum between two quantities related to the left and right boundary currents respectively, yielding a new critical value $\tilde{\rho}_L^c(\rho_R)$. The mDWT rate for the TASEP-LK can be defined by the function

$$\lambda(\rho_L, \rho_R) = \begin{cases} G(\alpha, q_0), & \beta \leq 1 - l \\ \min \{G(\alpha, q_0), F(\rho_L^c(\beta'), \beta')\}, & \beta \geq 1 - l \end{cases} \quad (6.3)$$

We report an example of the definition (6.3) in figure 6.2, for two values of beta respectively smaller and greater than $1 - l$.

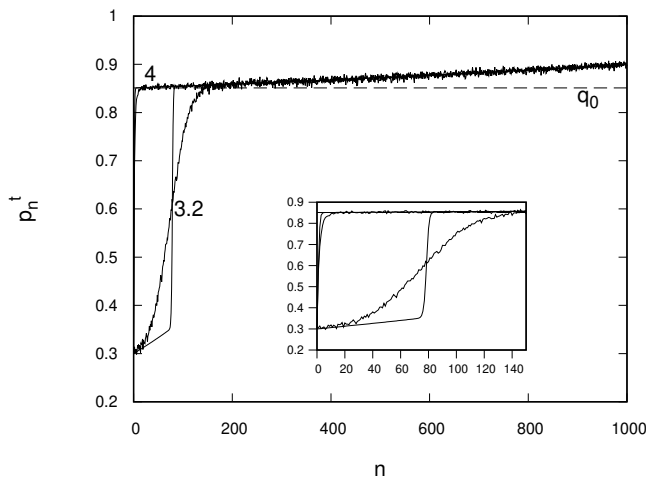


Figure 6.1: Density profile at two different times for the TASEP-LK, $\Omega_A = 0.4$, $\Omega_D = 0.1$, $\alpha = 0.3$, $\beta = 0.1$; with these parameter values $q_0 \approx 0.85115$ (dashed line). $t/N = 4$ is indistinguishable from the steady state. Solid lines: mean-field, noisy lines: KMC simulations (average over 10^4 trajectories).

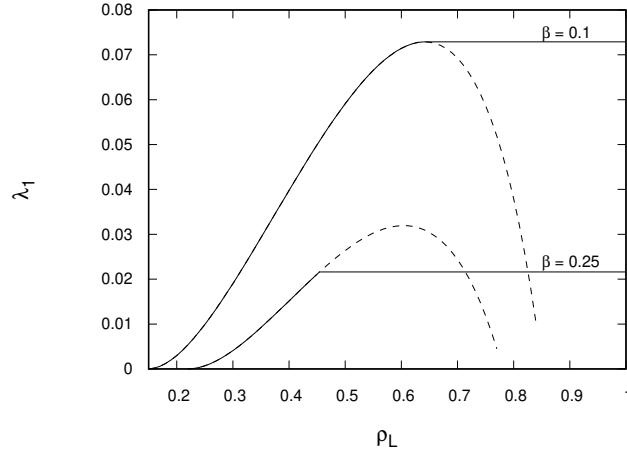


Figure 6.2: DWT rate (thin dashed line) and mDWT solution (thick solid line) as a function of ρ_L for the TASEP-LK, $\Omega_A = 0.4$, $\Omega_D = 0.1$. Top curve corresponds to $\beta = 0.1 < 1 - l$, bottom curve to $\beta = 0.25 > 1 - l$.

6.2 BST extrapolation for the TASEP-LK

As mentioned in section 4.3, the parameter σ in the BST algorithm corresponds to the size dependence $1/N^\sigma$ of the quantity that one wants to extrapolate. For the case under investigation we observe that, for values of σ greater than 1 (as it is for the slowest relaxation rate of pure TASEP), the extrapolation gives accurate results, whereas for $\sigma < 1$ it is unstable. To get an intuitive understanding of the cause of this instability, one can study the quantity of interest as a function of $1/N$. An illustrative picture is reported in figure 6.3: while for $\sigma > 1$ the curve reaches a plateau in the infinite size limit, in the complementary case there is a vertical tangent for $1/N \rightarrow 0$.

We now make two conjectures for the TASEP-LK: the first one is that the scaling exponent $2/3$ found for the mean-field slowest relaxation rate of the TASEP-LK in the fast phase is exact, the second one is that the mDWT is exact also for this model. We denote by $\lambda_e^{(N)}$ the exact slowest relaxation rate at finite size, by $\lambda_e^{(\infty)}$ its asymptotic value in the infinite size limit and by $\hat{\lambda}^{(\infty)}$ the one obtained by the mDWT. Given this argument, it would be possible to write

$$\lambda_e^{(N)} \simeq \lambda_e^{(\infty)} + CN^{-2/3}. \quad (6.4)$$

This choice is suggested by mean-field results and by observing that the plot of $\lambda_e^{(N)}$ as a function of $N^{-2/3}$ appears to be roughly linear for the largest N values analyzed.

To verify the conjectures, we study the extrapolation of the quantity

$$\xi_N := \left(\lambda_e^{(N)} - \hat{\lambda}^{(\infty)} \right)^a, \quad (6.5)$$

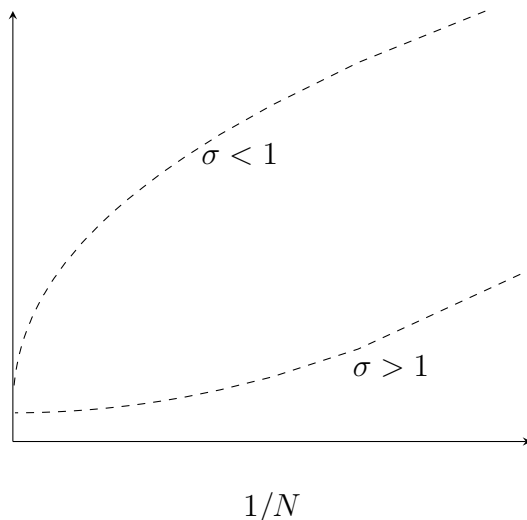


Figure 6.3: Intuitive explanation of the stability of BST extrapolation of a finite size sequence with scaling exponents σ greater or smaller than one. For $\sigma > 1$ the curve reaches a plateau in the infinite size limit, whereas for $\sigma < 1$ there is a vertical tangent for $1/N \rightarrow 0$.

which depends on the two parameters $\hat{\lambda}^{(\infty)}$ and a . In the hypothesis $\hat{\lambda}^{(\infty)} = \lambda_e^{(\infty)}$, this quantity would scale with the size as $CN^{-\frac{2}{3}a}$, thus we adopt $\sigma = \frac{2}{3}a$ in the BST algorithm. Varying $\hat{\lambda}^{(\infty)}$ until ξ_N extrapolates to zero, we have evidence that the value of the mDWT slowest relaxation rate giving a null extrapolant is very close to $\lambda_e^{(\infty)}$ (see the illustration in figure 6.4). Changing the parameter a , there are poles in the last extrapolants (see section 4.3), so there is more than one solution. We try to reduce as much as possible the number of spurious zeros and we select the closest solution to $\lambda_e^{(\infty)}$: for $a = 1$ we reobtain the unstable case of an exponent $\sigma < 1$, whereas for $a \geq 3$ there are many spurious solutions. Thus, an empirical prescription for this parameter is $1 < a < 3$ and we observed the optimal result for values of a roughly between 2.3 and 2.8, where the extrapolated points are less scattered. To verify the robustness of the extrapolation, we consider the result after all the iterations and we do different trials changing at each time the range in the system size: we fix $N_{max} = 21$ and we take $3 \leq N_{min} \leq 10$.

In figure 6.5 we compare the mDWT with the results obtained by the BST extrapolation for $a = 2.5$, superimposing all the series in N . We take the same example of figure 6.2: one can observe that the points are concentrated close to the mDWT curve for both low and high beta regions. This indicates that the exact slowest relaxation rate may have a unique scaling exponent, as for pure TASEP. As regards the case $\beta > 1 - l$, from the extrapolants we can distinguish an abrupt change of slope at the dynamical transition. The same behaviour is found studying λ_1 as a function of β in the fast fase (see figure 6.6): we observe a change of slope for

$\beta = 1 - l$ and the extrapolated points follow the mDWT curve. As β approaches the static transition with the MC phase, the slowest relaxation rate is very small and thus difficult to determine accurately: the BST results are more spread and can take negative values, but we know that the slowest relaxation rate approaches zero as β reaches $1/2$ and we can state that the points are consistent with this behaviour.

To obtain more accurate results by the BST extrapolation of exact finite size slow-

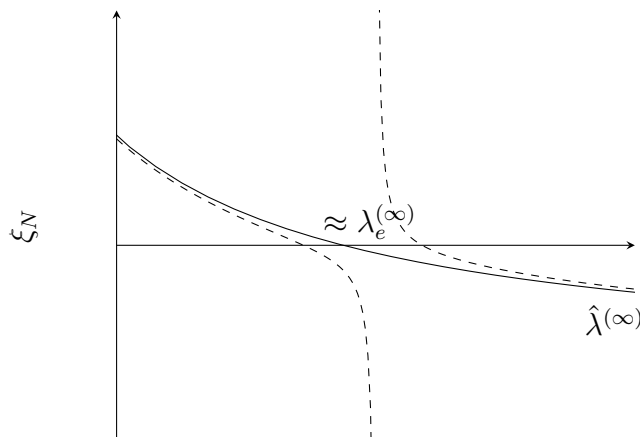


Figure 6.4: Example picture to illustrate the numerical evidences explained in the text. The value of ξ_N as a function of $\hat{\lambda}^{(\infty)}$ is denoted by a solid line: the value of $\hat{\lambda}^{(\infty)}$ such that ξ_N extrapolates to zero is very close to $\lambda_e^{(\infty)}$. Varying the parameter σ of the BST extrapolation, there are poles in the last extrapolants (dashed line).

est relaxation rates in the TASEP-LK, longer sequences would be needed, but we can conclude that the series shown above provide a rather clear numerical evidence of a dynamical transition. Using the same value for the parameter a , the points show a reasonable agreement with the reference curve of mDWT as a function of both α and β .

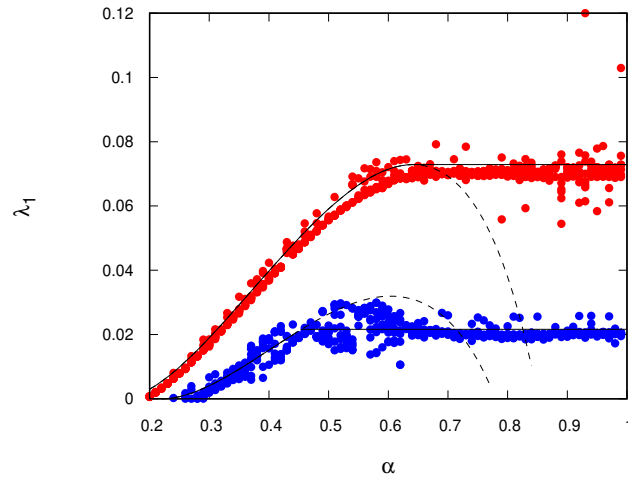


Figure 6.5: Comparison between mDWT and BST results as a function of α for the slowest relaxation rate of the TASEP-LK, $\Omega_A = 0.4$, $\Omega_D = 0.1$. For the BST method, we take $a = 2.5$ in (6.5) and we superimpose the extrapolations with different ranges in the system size: $N_{max} = 21$ and $3 \leq N_{min} \leq 10$. Top curve corresponds to $\beta = 0.1$, bottom curve to $\beta = 0.25$.

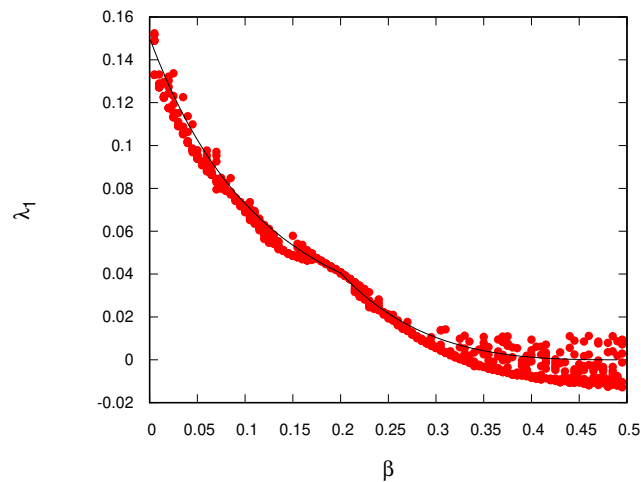


Figure 6.6: Comparison between mDWT and BST results as a function of β , for $\alpha = 0.9$. The model parameters are the same as in figure 6.5 and the same series in N are superimposed.

Chapter 7

Dynamical transitions in the AS model

In this chapter we present our results about the investigation of the dynamical transitions in the AS model with three approaches: the pair approximation, the mDWT and the BST extrapolation of exact finite size results. Dynamical transitions are found by all methods and the results are consistent. A novel feature in this model is the occurrence of a second slow phase in the same LD phase for strongly attractive interactions.

Almost all the contents of this chapter have been published in [38].

7.1 Pair approximation approach to the relaxation

We recall the time evolution equations (2.20) for the local densities

$$\dot{p}_n(t) = J_{n-1}(t) - J_n(t), \quad n = 1, \dots, N$$

and for the two-node expectations: eq. (2.21)

$$\dot{C}_n(t) = \theta P_{n-1}^t[100] + \eta P_n^t[1101] + \theta P_n^t[1100] - J_n(t),$$

for $n = 2, \dots, N - 3$ and eqs. (2.22)-(2.24)

$$\dot{C}_1(t) = \alpha_2 P_1^t[00] + \eta P_1^t[1101] + \theta P_1^t[1100] - J_1(t),$$

$$\dot{C}_{N-2}(t) = \theta P_{N-3}^t[100] + \beta_1 P_{N-2}^t[110] - J_{N-2}(t),$$

$$\dot{C}_{N-1}(t) = \theta P_{N-2}^t[100] + \beta_2 P_{N-1}^t[11] - J_{N-1}(t),$$

for the boundary nodes. We apply the pair approximation (2.6) to the 3- and 4-node marginals and we rewrite the dynamical equations in matrix form: we introduce

the $(2N - 1)$ -component vector

$$v^t = (p_1(t), C_1(t), \dots, p_{N-1}(t), C_{N-1}(t), p_N(t)), \quad (7.1)$$

so that we can write

$$\dot{v}^t = \phi(v^t). \quad (7.2)$$

The relaxation to the steady state $v = (p_1, C_1, \dots, p_{N-1}, C_{N-1}, p_N)$, given by the condition $\phi(v) = 0$, is described by the matrix M with elements

$$M_{i,j} = - \left. \frac{\partial \phi_i}{\partial v_j^t} \right|_{v^t=v}, \quad i, j = 1, \dots, 2N - 1. \quad (7.3)$$

The smallest eigenvalue of this matrix is the pair approximation prediction for the slowest relaxation rate. As was observed in the mean-field theory for the TASEP (see fig. 2.3), also the pair approximation for the AS model detects a dynamical transition as a qualitative change in the spectrum of the relaxation matrix. We show an example in figure (7.1), where we plot the 9 smallest eigenvalues as a function of ρ_L for the case $\eta = 1$, $\theta = 0.5$. These eigenvalues are real, while in the whole spectrum there are pairs of complex conjugates.

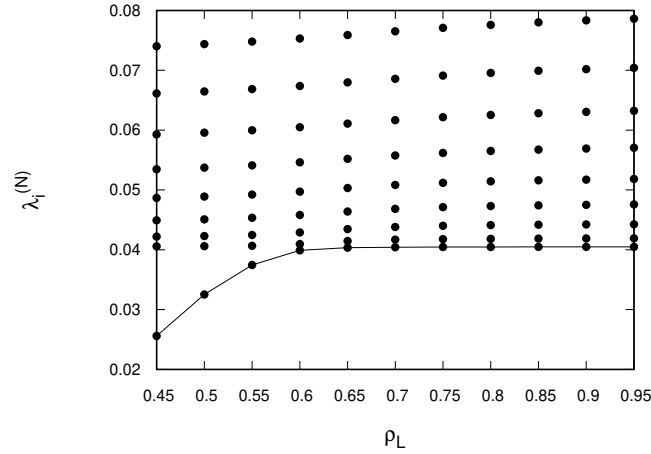


Figure 7.1: Low lying part $(\lambda_1, \dots, \lambda_9)$ of the spectrum of the pair approximation relaxation matrix as a function of ρ_L , for $N = 100$, $\eta = 1$, $\theta = 0.5$ and $\rho_R = 0.8$. The line connecting the points λ_1 is a guide for the eye.

7.2 The repulsive case

In figure 7.2 we show the static and dynamical phase diagrams of the AS model for $\theta = 1$ and $\eta = 0.1$. We report the dynamical transition lines provided by the

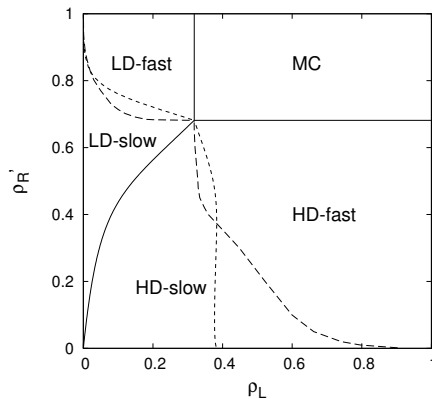


Figure 7.2: Phase diagram for strongly repulsive interactions, $\eta = 0.1$, $\theta = 1$. The static transitions are denoted by solid lines, thick (respectively thin) dashed lines indicate the dynamical transitions predicted by the pair approximation (resp. mDWT.)

pair approximation and by the mDWT, which are denoted by thick and thin dashed lines respectively. Considering the HD phase, for values of ρ_R' close to zero, the modified Domain Wall Theory predicts that the dynamical transition tends to a value of ρ_L smaller than one, at odds with the pair approximation.

In figure 7.3 we plot the smallest eigenvalue of the relaxation matrix λ_1 (it corresponds to the red lines) as a function of ρ_L for $\rho_R = 0.8$, $\eta = 0.8$ and $\theta = 1$, at various system sizes ($N = 100, 200, 400, 800$). The behaviour is analogous to that of the mean-field relaxation rate for the TASEP: one can observe a weak size dependence in the fast phase, where λ_1 approaches its asymptotic value as $1/N^2$, whereas this quantity is practically independent of the system size in the slow phase, where the scaling is exponential. We have verified numerically the same scaling of this relaxation rate in the fast phase, for different values of the parameters η , θ and at different values of ρ_R within the HD phase. Together with the pair-approximation slowest relaxation rate, we also show the results obtained by the mDWT (blue line) and by the extrapolation of the exact finite size results (black stars). As regards the latter method, we computed the smallest nonzero eigenvalue of the reduced transition matrix for $4 \leq N \leq 22$ and set the parameter σ in (4.16) at 2, after verifying numerically that this value gives near-optimal results according to the criterion (4.17) proposed in [36]. One can observe that the pair approximation overestimates significantly (of almost three times) the relaxation rate with respect to the other two methods, which are instead close to each other, with the mDWT rate slightly smaller than the extrapolation of the exact finite size results in the fast phase. This observation is reasonable, because in the pair approximation the system is exploring only a subset of all the possible configurations of the phase space and thus the dynamics is faster. Furthermore, the ratio η/θ is close to one,

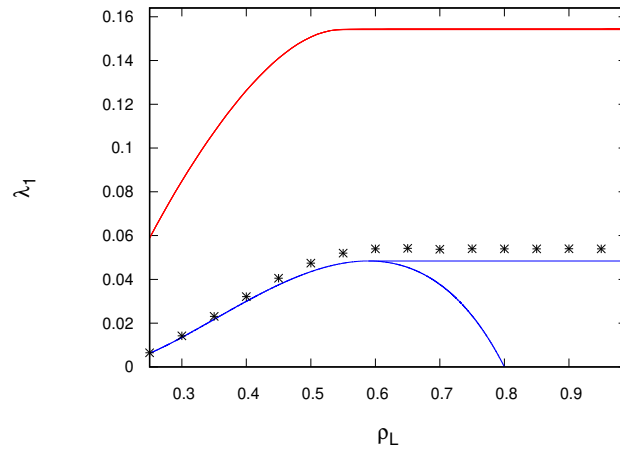


Figure 7.3: The relaxation rate λ_1 obtained by the three approaches as a function of ρ_L for $\eta = 0.8$, $\theta = 1$ and $\rho_R = 0.8$. From top to bottom: pair approximation for $N = 100, 200, 400$ and 800 (red lines), mDWT (blue lines) and extrapolation of exact finite-size results (black stars).

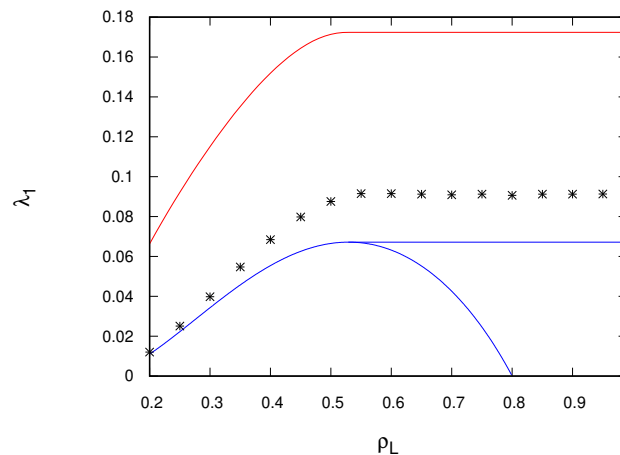


Figure 7.4: The relaxation rate λ_1 obtained by the three approaches as a function of ρ_L for $\eta = 0.5$, $\theta = 1$. The results of the pair approximation are computed for $N = 800$.

i.e. to the TASEP case, for which the mDWT rate is exact.

Keeping the same value of ρ_R , we consider two other examples with different values of the ratio η/θ , in the repulsive regime. For the case $\eta/\theta = 1/2$ reported in figure 7.4, we observe that the mDWT rate is below the extrapolated results except for small values of ρ_L . In the strongly repulsive case ($\eta = 0.1$, $\theta = 1$, figure 7.5) we

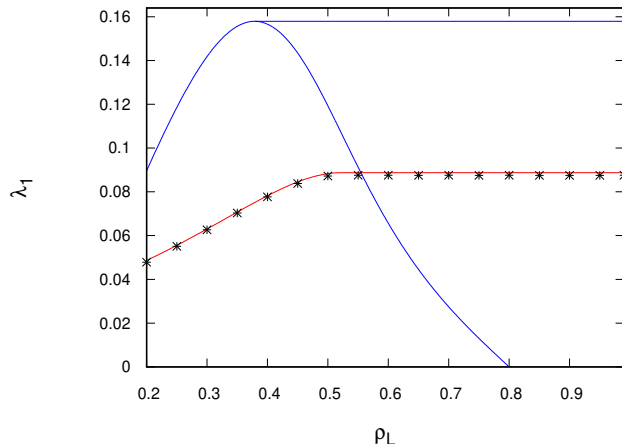


Figure 7.5: The same plot as in figure 7.4, for $\eta = 0.1$, $\theta = 1$. In this case, the mDWT overestimates the slowest relaxation rate, whereas the results from the pair approximation and the BST extrapolation are almost coincident.

observe an unexpected behaviour: the mDWT overestimates the relaxation rate, whereas the pair approximation result is almost coincident with that given by the extrapolation. This case corresponds to the phase diagram in figure 7.2, where we can see that the mDWT gives a different prediction for the dynamical transition line, especially at small values of ρ_R' . In figures 7.6 and 7.7 we plot the slowest relaxation rate obtained by the three approaches as a function of the ratio η/θ for $\rho_R = 0.8$ and two points in the slow ($\rho_L = 0.35$) and in the fast ($\rho_L = 0.99$) phase respectively. One can observe that the results obtained by the pair approximation and by the extrapolation of the exact finite size results are non-monotonic and reach a maximum at a given value of η/θ , whereas the mDWT rate is strictly decreasing. For small values of η/θ , the pair approximation rate is practically coincident with the exact result, then the two relaxation rates detach and become significantly different. The mDWT rate is greater than the other results in the strongly repulsive regime, then it is found below them for intermediate values of η/θ and approaches the exact result close to the pure TASEP limit ($\eta/\theta = 1$). In the slow phase we can see that the mDWT rate already reaches the extrapolated result at about $\eta/\theta = 0.7$.

Finally we look at λ_1 as a function of the current J and of ρ_R' in the strongly repulsive case $\eta = 0.1$, $\theta = 1$ and in the fast phase ($\rho_L = 0.99$): in figure 7.8 we plot the pair approximation slowest relaxation rate as a function of the current (right panel (b)), the left panel (a) shows J as a function of ρ_R' . We observe that the relaxation rate is not monotonically decreasing, as it is for pure TASEP. In figure 7.9a we show the slowest relaxation rate obtained by the three approaches as a function of ρ_R' : for small values of this parameter, the result of the pair approximation is

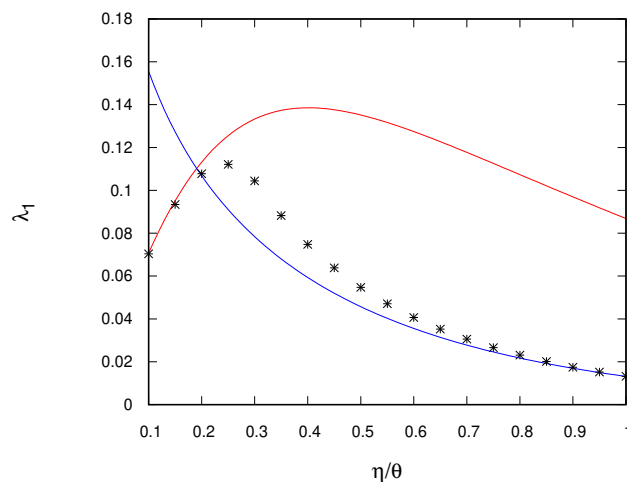


Figure 7.6: The relaxation rate λ_1 obtained by the three approaches as a function of the ratio η/θ , for $\rho_L = 0.35$ and $\rho_R = 0.8$. The pair approximation rate is computed for $N = 800$. The results obtained by the pair approximation and the extrapolation are non-monotonic and reach a maximum at a given value of η/θ , whereas the mDWT rate is strictly decreasing. For small values of η/θ , the pair approximation is practically coincident with the extrapolation.

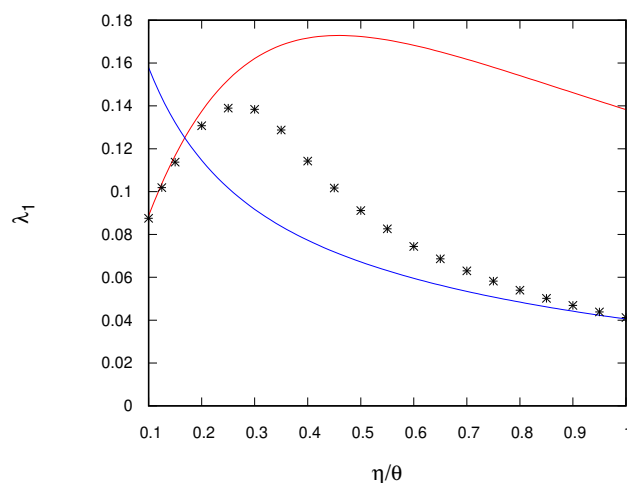


Figure 7.7: The same plot as in figure 7.6, for $\rho_L = 0.99$ and $\rho_R = 0.8$.

practically coincident with that obtained by the extrapolation of the exact finite size relaxation rates. The pair approximation rate reaches a maximum at about $\rho_R' = 0.5$, the extrapolated points are slightly increasing up to $\rho_R' = 0.4$, then they decrease to zero and are in good agreement with the mDWT rate, which is monotonically decreasing. For comparison, in figure 7.9b there is the same plot

for $\eta = 0.5$ and $\theta = 1$, where we can see that all the three relaxation rates are monotonically decreasing.

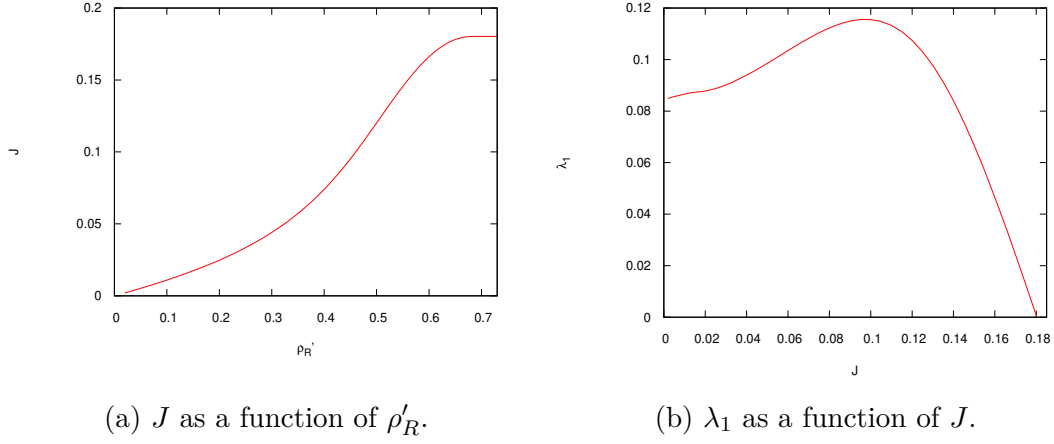


Figure 7.8: Pair approximation for the AS model, $\eta = 0.1$, $\theta = 1$, $\rho_L = 0.99$ and $N = 800$.

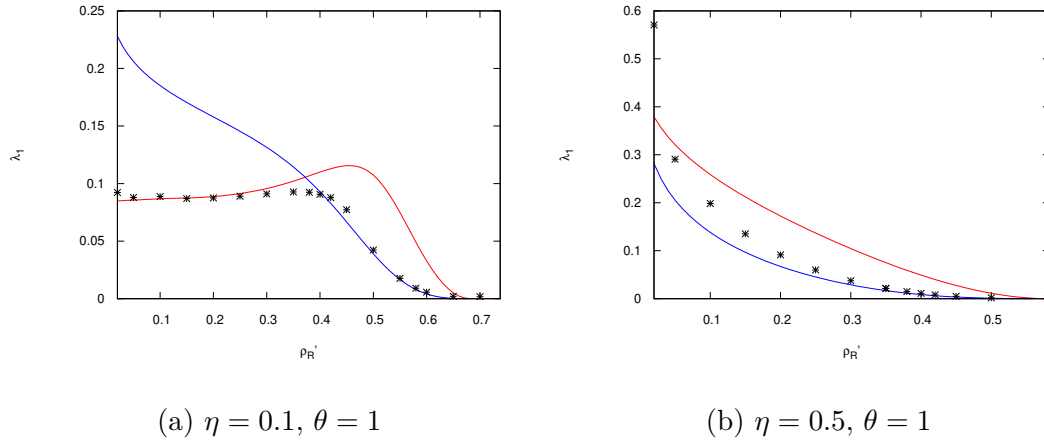


Figure 7.9: The relaxation rate λ_1 obtained by the three methods as a function of ρ'_R for $\rho_L = 0.99$. The results of the pair approximation are computed for $N = 800$.

7.3 The attractive case

In figure 7.10 we show the phase diagram of the model for weakly attractive interactions ($\eta = 1$, $\theta = 0.5$): in this case, the dynamical transition lines provided by the mDWT are close to the pair approximation ones. Then, in figure 7.11 we plot the slowest relaxation rate λ_1 obtained by the three approaches as a function

of ρ_L . The pair approximation rate (computed for $N = 800$) is significantly greater than the other two, also the mDWT slightly overestimates the exact result except for small values of ρ_L .

Now we concentrate on the strongly attractive case. We recall that, for η suffi-

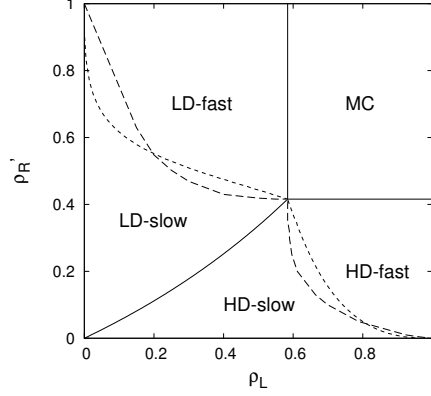


Figure 7.10: Phase diagram of the AS model for weakly attractive interactions, $\eta = 1$, $\theta = 0.5$. The static transitions are denoted by solid lines, thick (respectively thin) dashed lines indicate the dynamical transitions predicted by the pair approximation (resp. mDWT).

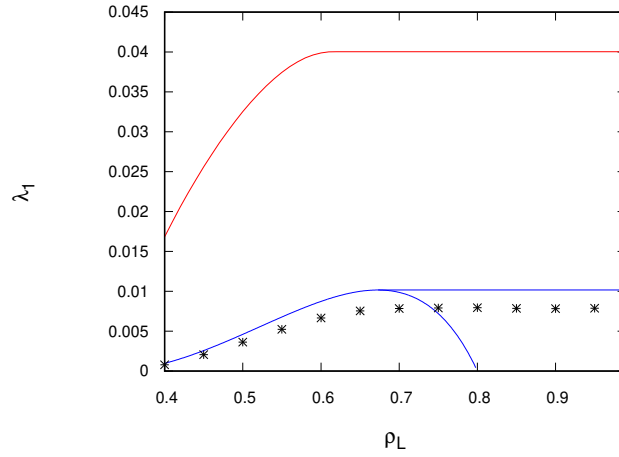


Figure 7.11: The relaxation rate λ_1 obtained by the three approaches as a function of ρ_L for $\eta = 1$, $\theta = 0.5$ and $\rho_R = 0.8$. From top to bottom: pair approximation for $N = 800$, mDWT and extrapolation of exact finite-size results.

ciently greater than θ , an additional HD-like phase (see section 1.3.2) is observed in the high- ρ_L , small- ρ_R corner of the phase diagram and that this phenomenon

is reproduced qualitatively by the pair approximation (see section 2.3, we observe it for $\eta/\theta \gtrsim 6$). In this case the model shows a remarkable novel feature: two dynamical transitions occur in the LD phase. As a consequence, there is a LD-slow phase at small values of ρ_R' , close to the “ordinary” HD phase, and another one at large values of the same parameter, close to the $\overline{\text{HD}}^{\text{IV}}$ phase. In figure 7.12 we show a portion of the phase diagram for $\eta = 1$ and $\theta = 0.1$, where the boundaries of the $\overline{\text{HD}}^{\text{IV}}$ phase are determined in the pair approximation. We note that, for the small values of θ necessary to observe the reentrant transition, it is very difficult to determine the dynamical transition line for smaller values of ρ_L , since the relaxation matrix becomes ill-conditioned. As one can see from figure 7.13, the second

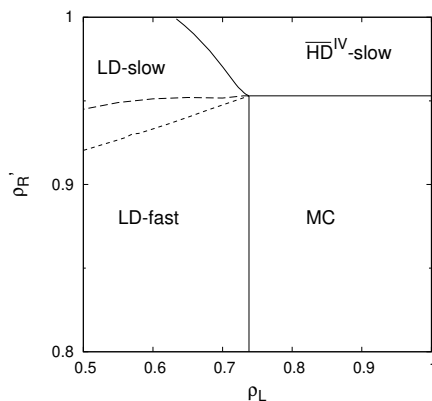


Figure 7.12: Portion of the phase diagram for strongly attractive interactions, $\eta = 1$, $\theta = 0.1$.

dynamical transition is found both in the pair approximation and the mDWT. We already mentioned in 2.3 that, for small values of ρ_R , the density on the right of the domain wall is a function $\bar{q}^{\text{IV}}(\rho_R)$, which in the pair approximation is linear. Thus, we fitted the bulk density of the $\overline{\text{HD}}^{\text{IV}}$ phase as a function of ρ_R and we computed the mDWT rate accordingly. Also the extrapolation of the exact rate at finite size seems to exhibit this new transition, however it is more difficult to obtain accurate results in this case. Considering $4 \leq N \leq 24$, we report the results after five (green bullets) and after all twenty iterations (black stars) of the BST algorithm. The difficulty comes from the emergence, in the last extrapolants, of poles which can be close to $\sigma = 2$ and thus yield a bias in the estimate of the rate. We give an example of this problem for the 20-iterations point at $\rho_R' = 0.9$, which is above the plateau formed by the points on its left: in figure 7.14 we plot the value of λ_1 as a function of σ . There is a pole near $\sigma = 2.16$, which yields a value of the rate greater than 0.001 at $\sigma = 2$, as one can see from the inset.

This problem was already observed in 6.2 for the TASEP-LK and in principle it can occur also with the pure TASEP, for which however the BST extrapolation

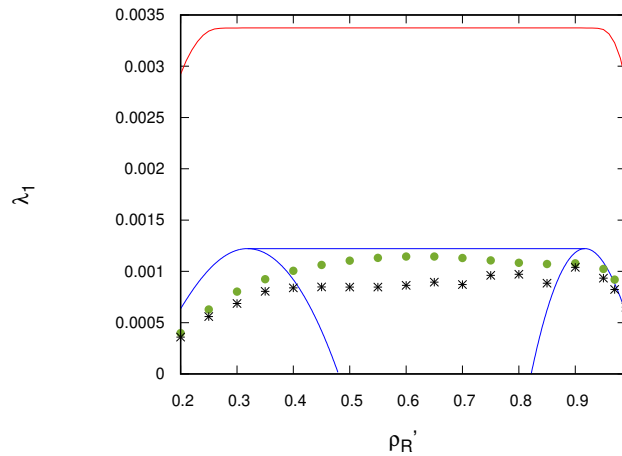


Figure 7.13: The relaxation rate λ_1 obtained by the three approaches as a function of ρ_R' for $\eta = 1$, $\theta = 0.1$ and $\rho_L = 0.52$. From top to bottom: pair approximation for $N = 800$, mDWT and extrapolation of exact finite-size results after 5 (green bullets) and after all (black stars) the iterations.

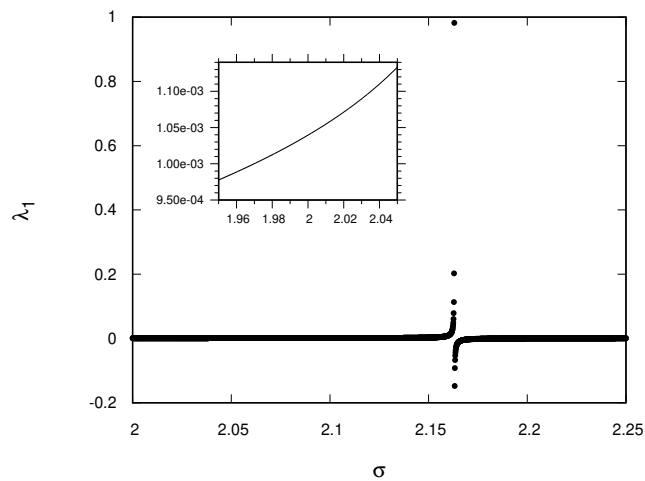


Figure 7.14: The last extrapolant of the relaxation rate λ_1 , obtained by the BST algorithm, as a function of the parameter σ . The inset shows the same quantity in a small interval centered at $\sigma = 2$.

gives very accurate results. In our analysis, we compute the rate in the fast phase with a small step in ρ_L (in fig. 7.15 we take $\Delta\rho_L = 0.001$) and hence we find a few localized singular values, but in fact almost all the points are concentrated on the exact location of the rate.

Coming back to the strongly attractive case of the AS model, we take a step of 0.01

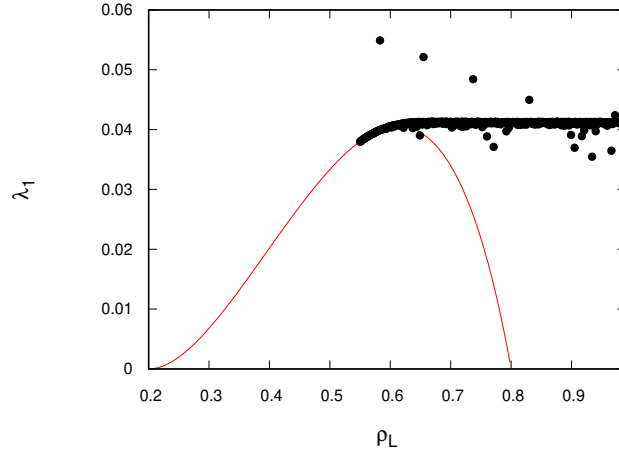


Figure 7.15: The last extrapolant (black bullets) of the relaxation rate λ_1 obtained by the BST algorithm for pure TASEP as a function of ρ_L , at $\rho_R = 0.8$. The red line denotes the mDWT result.

in the parameter ρ_R' and we compute the extrapolated results for the relaxation rate after all the iterations, considering different ranges in the system size. This approach was adopted also for the TASEP-LK, in this case we consider slightly longer sequences: we take $N_{\max} = 24$ and we vary N_{\min} from 4 up to 20, the results are reported in figure 7.16. The lower curves correspond to $4 \leq N_{\min} \leq 10$ and $N_{\min} = 12$ (dark green bullets), the upper series correspond to $18 \leq N_{\min} \leq 20$. One can realize that the majority of the series in N are concentrated in the lower part and suggest the most likely value of the relaxation rate, moreover they reveal the two dynamical transitions. The shorter sequences overestimate λ_1 and yield a poor definition of the first transition.

The relaxation rate of the $\overline{\text{HD}}^{\text{IV}}$ phase is very small and depends on both boundary densities, as in the HD-slow phase. For this reason, we denote this phase as $\overline{\text{HD}}^{\text{IV}} - \text{slow}$ in figure 7.12.

7.4 Full dynamics of the model

Considering as an example the repulsive case with the same values of θ and η as in figure 7.2, we take two points in the HD phase, corresponding to the slow ($\rho_L = 0.2$, $\rho_R = 0.5$) and the fast ($\rho_L = 0.5$, $\rho_R = 0.5$) phases respectively. For both cases we study the full time evolution of the density profile from an almost empty lattice (uniform density at 0.01) with no correlations. The results are reported in figures 7.17 and 7.18, where we compare the dynamical equations of the pair approximation with the Kinetic Monte Carlo results (average over 10^4 trajectories).

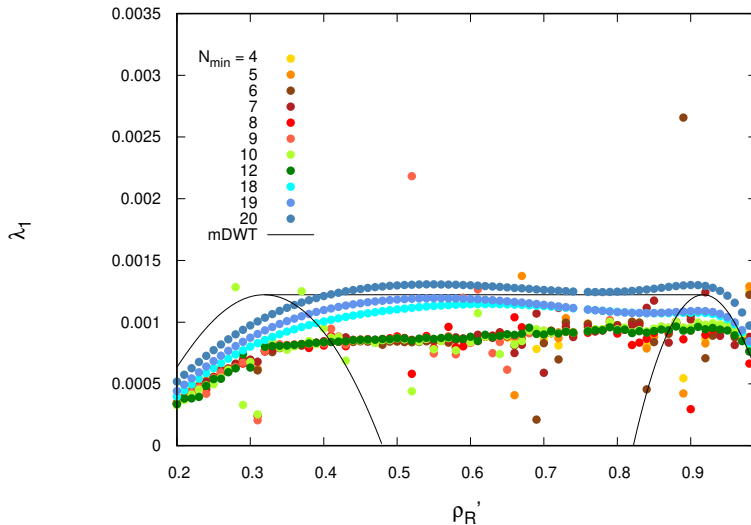


Figure 7.16: The last extrapolant of the relaxation rate λ_1 as a function of ρ_R' , considering different ranges in N , where $N_{max} = 24$. The bottom curves correspond to $4 \leq N_{min} \leq 10$ and $N_{min} = 12$ (dark green bullets), the upper series are given by $18 \leq N_{min} \leq 20$. The thin black lines denote the mDWT.

We observe that the picture provided by the pair approximation shows a good agreement with the simulations, the only relevant difference being that its domain walls are too sharp. A similar analysis was performed in [23] for another model in the KLS class, considering a single point in the phase diagram and with no reference to a dynamical transition. The MCAK approximation, introduced in the latter work and already mentioned in 2.3, exhibited the same feature in the shock.

In the HD-slow phase, we can distinguish two regimes: in a first part (which was called penetration regime in [23]) up to $t_1/N = \rho_L/J(\rho_L) \sim 1.5$, particles fill the lattice and form a LD-like plateau at ρ_L , which occupies almost all the system apart from a boundary layer close to the right end. This is an interesting feature, considering also that the slow phases are located near the LD-HD coexistence line: even if the plateau is not a long-lived metastable state, the slow phase could be viewed as a loose analogue of metastability regions in equilibrium phase diagrams. In the second regime (called intermediate in [23]) from t_1 to the steady state, a domain wall separating two regions of uniform densities ρ_L and ρ_R moves to the left with a velocity v_s given by (3.2), whose magnitude increases with ρ_L . For the parameter values in example, $v_s \simeq -0.105$.

The dynamics in the HD-fast phase can again be divided into two parts. However, in the penetration regime, the injection rate is so large that the particles do not have time to form a plateau at density ρ_L , which would take a time $t_1/N = \rho_L/J(\rho_L) \sim 4$. Since in the previous case $|v_s|$ was increasing with ρ_L , the shock moves faster than

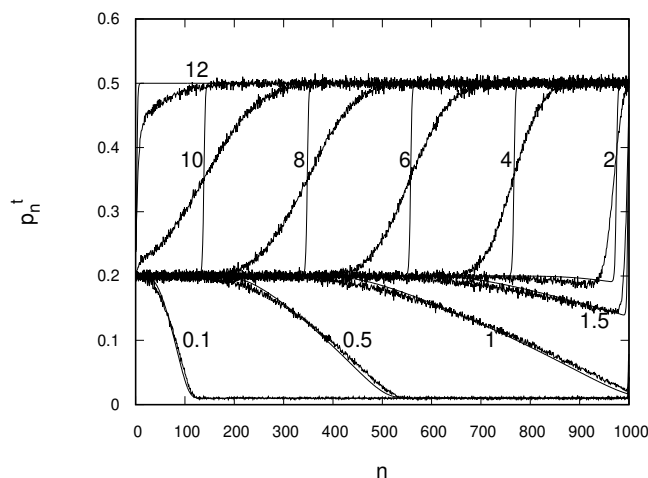


Figure 7.17: Density profile at different times for $N = 1000$, $\eta = 0.1$, $\theta = 1$ in the HD-slow phase ($\rho_L = 0.2$, $\rho_R = 0.5$). The number near each curve is the reduced time t/N , $t/N = 12$ is indistinguishable from the steady state. The thick smooth lines correspond to the pair approximation, the thin noisy ones denote the KMC simulation (average over 10^4 trajectories).

in the slow phase. Its velocity increases with time, but it is smaller than v_s (in the limit $\rho_L \rightarrow \rho_R^-$), because the density immediately on the left of the shock is smaller than ρ_L . Actually, we verified that in the parameter region of the HD-fast phase the shock speed no longer increases with ρ_L .

Moreover, it turns out that the full dynamics is practically independent of ρ_L in

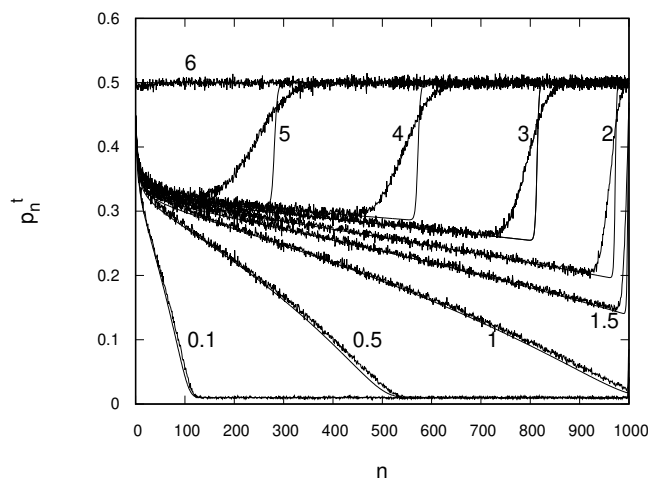


Figure 7.18: Same as fig. 7.17 in the HD-fast phase ($\rho_L = 0.5$), $t/N = 6$ is indistinguishable from the steady state.

the fast phase: in figure 7.19 we plot the current profiles at different times for three values of the left boundary density ($\rho_L = 0.5$ with solid line, $\rho_L = 0.7$ with dotted line and $\rho_L = 0.9$ with dashed line) in the HD-fast phase. Except near the left boundary, the three curves are coincident; this feature is confirmed by the KMC simulations, denoted by noisy lines. A similar behaviour is observed if one looks at the density or at the two-node marginals. These results support the existence of a dynamical transition and indicate that the pair approximation is a reliable method also for describing the dynamics of the model. The dynamical properties

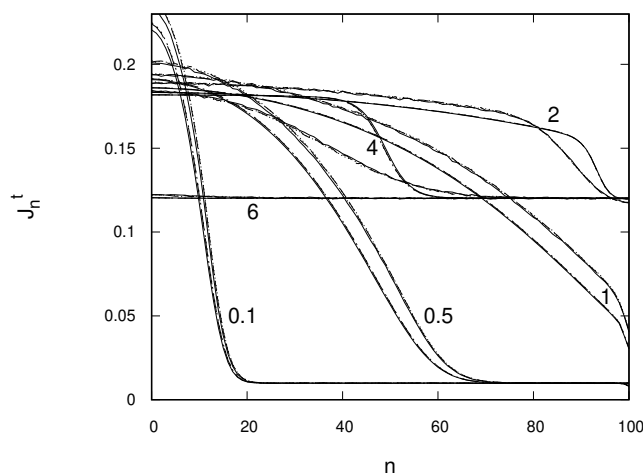


Figure 7.19: Current profile at different times for $N = 100$, $\eta = 0.1$, $\theta = 1$, $\rho_R = 0.5$ and at three different values of ρ_L in the HD-fast phase: 0.5 (solid lines), 0.7 (dotted) and 0.9 (dashed). $t/N = 6$ is indistinguishable from the steady state. The pair approximation results are denoted by thick smooth lines, the KMC simulations (average over 10^6 trajectories) by thin noisy lines.

observed in this example remain valid also for other values of η and θ . In the $\overline{\text{HD}}^{\text{IV}}$ phase, one does not observe the formation of a plateau at intermediate times in the evolution of the density profile.

We now consider the dynamics of the same case ($\eta = 0.1$, $\theta = 1$) for $\rho_R = 0.8$, in order to try to get some insights into what was observed in section 7.2 about the slowest relaxation rate. In particular, if the pair approximation rate is practically coincident with the exact one, we expect that the position of the domain walls in the pair approximation and in the KMC simulation should be the same in the long time dynamics (very close to the steady state). In figure 7.20 we show an example in the slow (a) and in the fast (b) phases: the penetration regime is analogous to what is observed in figures 7.17 and 7.18, then at $t/N = 2$ the profile forms a structure on the top of the domain wall which extends and becomes practically linear in n , with a slope progressively decreasing as the dynamics goes on. This

feature, which is more marked in the fast phase, entails that the mDWT cannot give an accurate result for the relaxation rate in this case, because the density on the right of the wall is not equal to ρ_R . We can see that the density immediately on the right of the wall in the pair approximation and in KMC simulations are already very close to each other at intermediate times.

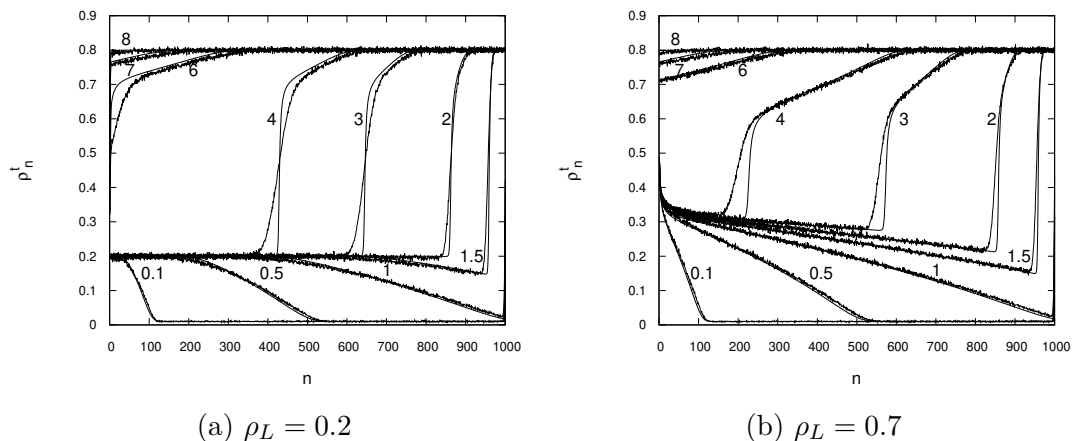


Figure 7.20: Density profile at different times for the same values of the hopping rates as in figure 7.17, in the slow (a) and in the fast (b) phases at $\rho_R = 0.8$. $t/N = 8$ is indistinguishable from the steady state. Thick smooth lines denote the pair approximation, thin noisy lines denote KMC simulations (average over 10^4 trajectories). At $t/N = 2$ the profile forms a structure on the top of the domain wall which extends and becomes practically linear in n , with a slope progressively decreasing as the dynamics goes on. The density immediately on the right of the wall in the pair approximation and in KMC simulations are already very close to each other at intermediate times.

Chapter 8

Reflections upon the physical meaning of the dynamical transition

With reference to the driven diffusive models that have been investigated in the thesis, in this chapter we try to think back to the properties of the dynamical transition, underlining the aspects that can help in giving a physical understanding of this phenomenon. We start with a discussion of the methods adopted in our research activity, compared to the techniques employed in previous works on the PASEP/TASEP dynamical transitions.

8.1 Discussion of methods

As was mentioned in 1.2, the existence of a dynamical transition was discovered for the TASEP by De Gier and Essler [9, 13], who employed the Bethe ansatz to diagonalize the transition matrix of a PASEP with open boundary conditions and arbitrary values of hopping and injection/extraction rates. They derived equations describing the complete relaxation spectrum, then, considering the TASEP as a special case, the authors determined the asymptotic behaviour of the spectral gap (the slowest relaxation rate) in the infinite size limit. Thanks to this analytical approach, it was found that the gap does not vanish in the infinite size limit in the HD and LD phase regions and that it exhibits a singularity.

The purpose of this thesis is to investigate the existence of dynamical transitions in two models more general than the TASEP, for which an exact solution is not available. Therefore, we have to resort to approximations and to combine different methods in order to ensure that our results indicate a true dynamical transition and are not due to artifacts. Building on the fact that the cluster mean-field approximations reproduce the exact static phase diagram of the TASEP and yield

dynamical transition lines close to the exact ones [1], we applied them also to the TASEP with Langmuir kinetics and to the AS model. For the first case, we managed to perform an analytical treatment within the mean-field approximation and to determine asymptotic bounds for the slowest relaxation rate which become tight in the infinite size limit. For the second case, the simple mean-field is not adequate [18], thence we employed a pair approximation: with the choice of bulk-adapted boundary rates and $\rho_L = \rho_R = \rho$, it reproduces the exact steady state bulk current-density relation at any finite size. Consequently, the pair approximation with this choice of the boundary rates yields the exact location of most static phase transitions. We determined numerically the smallest eigenvalue of the relaxation matrix: dynamical transitions are found also in the pair approximation for this model, moreover the results point out a second transition in the same LD phase when the interactions are strongly attractive.

The dynamical transitions of both models have been investigated also with other approaches. We adopted two techniques originally adopted for the TASEP [3, 13, 2], but applicable to generic driven diffusive models: they are the modified Domain Wall Theory and the Bulirsch-Stoer extrapolation method. The mDWT is a heuristic solution which takes the DWT rate in the slow phase and its maximum value in the fast phase. It was introduced in [13] and then in [2] to solve the problem of the original DWT presented in [3], which erroneously predicted a relaxation rate independent of β for $\alpha \geq 1/2$. While it is exact by construction for pure TASEP, we cannot expect this property to be satisfied also in the presence of interactions, because the theory does not take into account a possible internal structure of the wall, which could be non-negligible in the presence of interactions. Actually, in chapter 7 we verified that the mDWT approaches the exact result (given by the extrapolation of the exact finite size relaxation rates) as the ratio η/θ reaches unity. Nevertheless, also the mDWT rate exhibits a second dynamical transition for ρ_R' close to 1. Conversely, for the TASEP-LK we conjectured the exactness of the mDWT predictions and we observed a good agreement with the results of the BST extrapolation.

The latter method was also applied in [3] to the finite size slowest relaxation rates of the TASEP and it was subsequently shown to accurately reproduce the exact asymptotic result. We verified that this method can be applied also to the AS model, with the same value of the parameter σ in (4.16) used for pure TASEP. The strongly attractive case ($\eta/\theta = 10$) is more difficult to treat because of the occurrence of poles [36] near $\sigma = 2$ in the last extrapolants, however we can state that also the BST extrapolation reveals the dynamical transitions of the AS model, including the one close to the HD^{IV} phase. For the TASEP-LK, the exponent $\sigma < 1$ makes the extrapolation unstable, thus we considered a quantity depending on two parameters: the first one is the mDWT rate, that is subtracted from the finite size slowest relaxation rate, the second one is the exponent a to which the difference is raised. We varied the mDWT rate until the difference extrapolates to zero and

chose the value of a in order to reduce as much as possible the number of spurious solutions. The results provide an evidence of the two kinds of dynamical transition and show a good agreement with the mDWT predictions.

A further approach to investigate the TASEP dynamical transition are kinetic Monte Carlo simulations: in [4], Proeme et al. tried to compute the slowest relaxation rate by measuring the decay rate of different observables at long times. They chose an initial condition far from the steady state: considering the HD phase, each site of the lattice is independently occupied with probability α . The infinite size limit of the relaxation rate was obtained by a polynomial fit of finite size results. The main difficulty is that the residual signal after all the higher relaxation modes have decayed is small and affected by noise. The results showed qualitatively a greater agreement with the exact prediction by De Gier and Essler than with the original DWT one, but were not accurate. Thus, the authors computed the slowest relaxation rate using the Density Matrix Renormalization Group (DMRG) method. We tried to determine the slowest relaxation rate of the AS model by simulating systems of sizes much greater than those considered in [4] (we went up to $L = 1000$), but it was not possible to observe a clear single exponential relaxation and obtain a better estimate, probably because of the small separation among the smallest eigenvalues of the transition matrix. However, thanks to the simulations, we understood that the full dynamics of the system is independent of the control parameter (ρ_L for the HD phase) in the fast phase. Moreover, we observed a good agreement of the pair approximation with KMC simulations, confirming the effectiveness of cluster mean-field methods to study driven diffusive models.

8.2 Physically relevant aspects

Considering the HD phase for simplicity and looking at the behaviour of the low-lying eigenvalues of the relaxation matrix as a function of ρ_L (figs. 2.3, 5.7, 5.8 and 7.1), we can grasp an important property of the dynamical transition, that is the competition between bulk and boundary layer: in the fast phase, ρ_L is close to the bulk density ρ_R , so that the bulk properties predominate in determining the relaxation dynamics. In the slow phase instead, ρ_L is far from ρ_R , thus the slowest relaxation mode is driven by the boundary. In section 5.2.2 we understood the same point by looking at the structure of the simplified matrix B , where the boundary layer acts in the diagonal terms, whereas the bulk currents appear in the off-diagonal terms. Considering the TASEP, we find the deviation from the pure Toeplitz structure in the diagonal elements.

Another aspect is the dependence of the slowest relaxation rate on the uniform current, in the TASEP and in the AS model, or on the maximal current in the TASEP-LK. The mean-field theory for the TASEP and the TASEP-LK indicates that the slowest relaxation rate decreases upon increasing the maximum current,

meaning that a steady state which is farther from equilibrium, takes a longer time to be established. Also for the AS model we verified the same behaviour of λ_1 at different values of the ratio η/θ in the HD phase. The only exception is the extreme (repulsive) case $\eta = 0.1$, $\theta = 1$, for which the slowest relaxation rate predicted by the pair approximation is increasing up to a certain value of J (see fig. 7.8b).

A common trait of the models studied here is that the slow phases are located in the phase diagram close to the LD-HD coexistence line. Moreover, looking at the full dynamics of the AS model in the HD phase, we observed the formation of a LD-like plateau at intermediate times in the slow phase. Although this plateau is not a long-lived metastable state, the slow phase could be viewed as a loose analogue of metastability regions in an equilibrium phase diagram. The same behaviour is observed in the full dynamics of the TASEP and also in the relaxation dynamics of the TASEP-LK one can see the formation of a LD-like profile: we show an example in figure 8.1 for $N = 1000$, $\alpha = 0.35$, $\beta = 0.3$, $\Omega_A = 0.3$ and $\Omega_D = 0.1$. The LD bulk profile is denoted by a thick red line.

Another important point is that of a change in the structure of the eigenvector

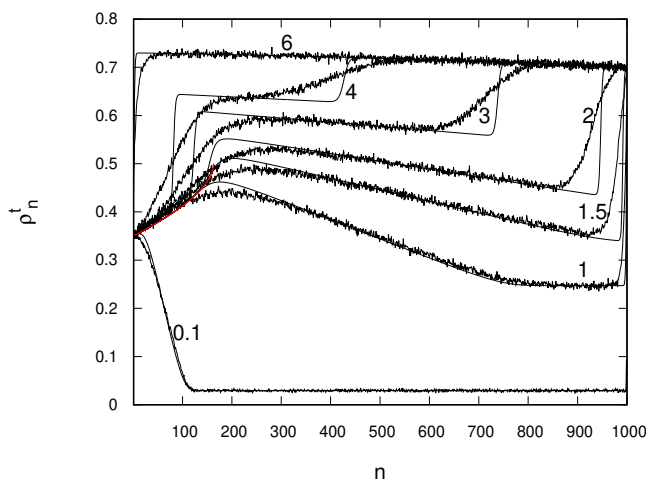


Figure 8.1: Density profile at different times for the TASEP-LK. $N = 1000$, $\alpha = 0.35$, $\beta = 0.3$, $\Omega_A = 0.3$ and $\Omega_D = 0.1$. The LD bulk profile is denoted by a thick red line. $t/N = 6$ is undistinguishable from the steady state.

corresponding to λ_1 at the dynamical transition. Considering the mean-field theory for the TASEP, the components of the eigenvector of the original relaxation matrix (see eq. (5.6)) decay exponentially to zero. We can estimate the parameters of the exponential function through a fit, then divide the eigenvector components by the fitting function evaluated at the same n and observe the residual structure. We show an example for $\beta = 0.4$ and $N = 600$. We compute the critical threshold at finite size $\alpha_c(\beta, N = 600) \approx 0.50045$ and we consider α values close to the dynamical transition, to exclude the possibility that the change in the shape of the eigenvector

could be due to other causes. We plot the components of the eigenvector of the original (non symmetrized) relaxation matrix in log-y scale and fit them with a linear function $y = a + bn$, we report the fit parameters in table 8.1 We can see that

α	a	b
0.495	0.553	-0.216
0.498	0.549	-0.210
0.502	0.972	-0.205
0.51	1.871	-0.203
0.55	3.106	-0.203

Table 8.1: Fit parameters of the components of the eigenvectors \mathbf{v}_1 of the non-symmetrized mean-field relaxation matrix for the TASEP at different α values in the slow and fast phases. $\beta = 0.4$, $\alpha_c(\beta, N = 600) \approx 0.50054$.

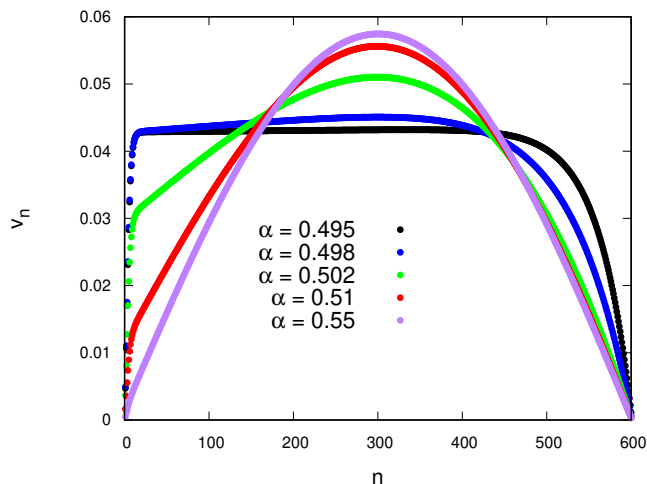


Figure 8.2: Components of the same eigenvectors of table 8.1 obtained after dividing by the exponential decay.

the slope b , which is equal to the inverse of the characteristic length of the exponential, becomes constant in the fast phase. In figure 8.2 we show the components of the eigenvectors obtained after dividing by the exponential function. In the slow phase the eigenvector is constant in the central region (the bulk), whereas in the fast phase it takes a sinusoidal shape, which becomes exactly equal to a function of the type $C \sin\left(\frac{n\pi}{N}\right)$ only for $\alpha = \beta'$ (i.e. when the relaxation matrix is purely Toeplitz).

After performing the similarity transformation given by eq. (5.7), the eigenvector still has an exponential decay and we verified numerically that the behaviour in the

bulk is given by $\zeta(x_*)^n$ (see fig. 8.3).

The same qualitative picture holds also for the AS model: making reference to the

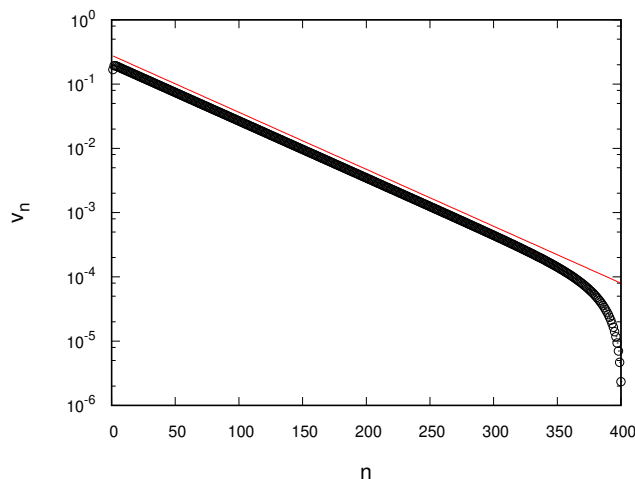
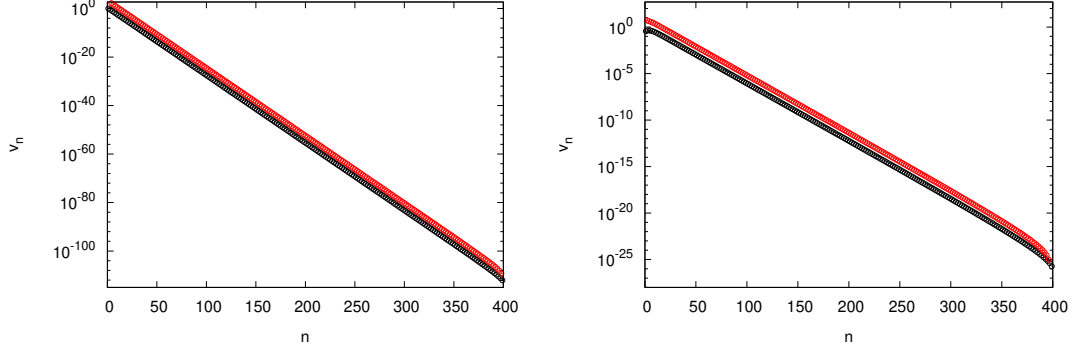


Figure 8.3: Components of the eigenvector corresponding to λ_1 of the symmetric relaxation matrix for $\alpha = 0.64$, $\beta = 0.1$ and $N = 400$. The slope of the red line is equal to $\log \zeta(x_*)$.

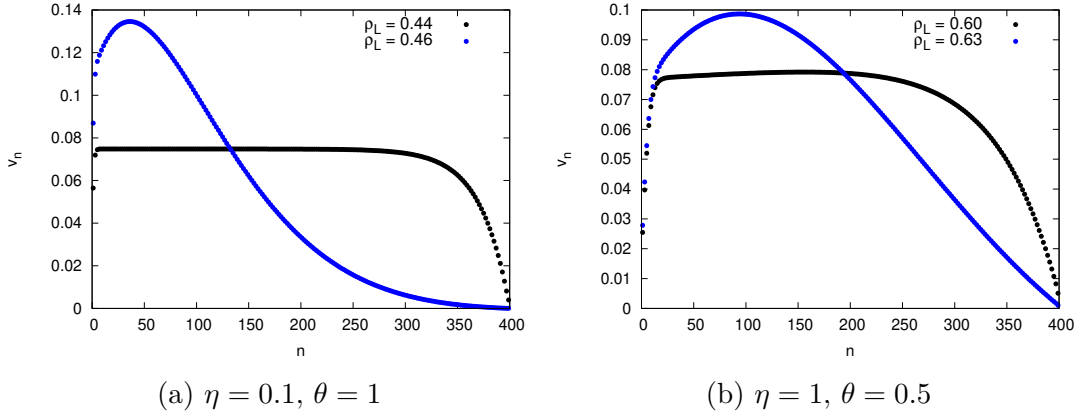
phase diagrams 7.2 ($\eta = 0.1$, $\theta = 1$) and 7.10 ($\eta = 1$, $\theta = 0.5$), in figure 8.4 we plot for both examples the density (black circles) and correlation (red circles) components of the eigenvector corresponding to λ_1 of the pair approximation relaxation matrix. We can see again an exponential decay in the bulk. In figure 8.5 we plot the density components after dividing by the exponential decay in the slow and in the fast phase.

The results reported here conclude the technical part of the thesis. The final section is devoted to an overall summary of the results and to an outline of possible future research lines.



(a) $\eta = 0.1, \theta = 1, \rho_L = 0.44, \rho_R = 0.7$. (b) $\eta = 1, \theta = 0.5, \rho_L = 0.6, \rho_R = 0.8$.

Figure 8.4: Components of the eigenvector corresponding to λ_1 of the AS model for $N = 200$. Black/red circles denote the components corresponding to densities/correlations. Left panel: strongly repulsive case (fig. 7.2). Right panel: weakly attractive case (fig. 7.10).



(a) $\eta = 0.1, \theta = 1$

(b) $\eta = 1, \theta = 0.5$

Figure 8.5: Components (densities) of the eigenvector corresponding to λ_1 after dividing by the exponential decay in the slow (black) and fast (blue) phases. The values of η and θ are the same as in figure 8.4, $N = 200$.

Conclusions and prospects

From the results obtained in this thesis, the most important evidence is that the dynamical transition appears to be quite a robust phenomenon, which does not depend strongly on the specific dynamical rules of the driven diffusive system under consideration. Another relevant aspect is that new dynamical transitions arise in the two models studied in this project. In particular, in the unbalanced TASEP-LK we observe that the slowest relaxation rate exhibits a discontinuity in the first derivative at the dynamical transition in the high beta region of the HD phase: this behaviour has similarities with equilibrium first order transitions. In the AS model, two dynamical transitions are found in the same LD phase for values of the ratio η/θ sufficiently high to observe the $\overline{\text{HD}}^{\text{IV}}$ phase.

As was observed for pure TASEP [1], we can state that the mean-field like cluster approximations are reliable methods to analyse driven diffusive models and we showed that they also reproduce the full dynamics with good accuracy. For the TASEP-LK we worked within the ordinary mean-field approximation and derived analytical results for the slowest relaxation rate predicting a dynamical transition. The mean-field framework could be adequate to study the relaxation dynamics of more general models. One example is the TASEP-LK with two lanes [39, 40]: the introduction of this model is motivated by experimental observations on molecular motors [41], which can move along parallel tracks and jump between them. Another aspect that could be accounted for are finite reservoirs of particles. For the latter problem there is an equivalent definition of the open TASEP [42] on a ring of $L + 1$ nodes, where the additional site $n = 0$ acts as a reservoir and the total number of particles N_{tot} is fixed. A particle of the reservoir can jump to the site $n = 1$ with rate α , if the latter is empty. A particle at site $n = L$ leaves the lattice with rate β , independently of the number of particles in the reservoir. If $N_{tot} \geq L + 1$, then $\rho_0 \geq 1$ (unlimited occupation) and the properties of sites $n = 1, \dots, L$ are identical to those of the open TASEP. The case $N_{tot} < L + 1$ is the so-called “parking garage model” and was studied in [43].

For the AS model we studied the effect of local interactions on dynamical properties within a pair approximation. A possible future direction for this and for more complex cluster methods, is to investigate the relaxation dynamics of driven

diffusive models with interactions between extended size particles like the ones considered in [44, 45, 46]: this generalization of the AS model could be important for biological traffic processes, characterized by molecules larger than their step size and interacting with one another. Exact solutions for the TASEP with arbitrary size particles without interactions were obtained for periodic boundary conditions (see [47] and references therein). Also for this case the ordinary mean-field is not accurate because the lengths of particles introduce correlations. Thinking about applications to the modeling of mRNA translation - the process that inspired the original formulation of the TASEP in [12] - another ingredient would be a set of heterogeneous hopping rates. For this problem there are no exact solutions yet: some results have been obtained through approximate methods for the case with one [48] or two [49] defects, i.e. sites having hopping rate smaller than one, for dynamic obstacles which attach and detach randomly from lattice sites [50] or for a set of quenched hopping rates chosen from a distribution (see [51] and references therein).

We have also experimented for both models two methods originally employed to determine the slowest relaxation rate of pure TASEP: the mDWT and the BST extrapolation of exact finite size results. For the AS model the mDWT is no more exact and predicts a different location of the dynamical transition with respect to the pair approximation for strongly repulsive interactions. Nevertheless, it reveals the dynamical transitions found by the pair approximation and potentially it could be applied to investigate this phenomenon in more complex models. Guided by the insights of the mean-field analysis, we generalized the mDWT to the TASEP-LK and we conjectured its exactness.

The BST extrapolation of the exact slowest relaxation rates at finite-size for the AS model is more tricky in the strongly attractive case, but different trials like the one shown in figure 7.16 could be performed to determine the most likely location of the exact slowest relaxation rate. For the TASEP-LK we defined a criterion to avoid an unstable behaviour of the BST algorithm and to reduce as much as possible the formation of poles in the last extrapolants. Our results reveal both kinds of dynamical transition and agree with the conjecture.

In conclusion, in this thesis we have obtained new results on the dynamical transitions in two possible extensions of the TASEP. We believe that the theory and the tools presented in the previous chapters could be the starting point to investigate the relaxation dynamics of more complex driven diffusive models and we hope that they will encourage further research in this intriguing topic of nonequilibrium statistical physics.

Appendix A

Time evolution equations of the marginal cluster probabilities

In this appendix we derive the dynamical equations for the local densities (2.3) and the two-node marginals (2.4) of the TASEP from the master equation of the process, then we generalize the procedure to the AS model, deriving equations (2.20) and (2.21).

We denote by x and y the lattice configurations respectively before and after a transition (see section 4.1). With reference to the master equation (1.3), the elements of the transition matrix are given by the sum of the contributions of all the possible transition processes.

$$W_{y,x} = \sum_{n=0}^N W_{y,x}^n. \quad (\text{A.1})$$

A.1 Pure TASEP

For $n = 1, \dots, N - 1$ (hopping processes) we have

$$W_{y,x}^n = \delta(y_1, x_1) \cdot \dots \cdot \delta(y_{n-1}, x_{n-1}) x_n (1 - x_{n+1}) (y_{n+1} - y_n) \cdot \\ \times \delta(y_{n+2}, x_{n+2}) \cdot \dots \cdot \delta(y_N, x_N), \quad (\text{A.2})$$

whereas at the boundaries (injection and extraction)

$$W_{y,x}^0 = \alpha (1 - x_1) (2y_1 - 1) \delta(y_2, x_2) \cdot \dots \cdot \delta(y_N, x_N), \quad (\text{A.3})$$

$$W_{y,x}^N = \beta \delta(y_1, x_1) \cdot \dots \cdot \delta(y_{N-1}, x_{N-1}) x_N (1 - 2y_N). \quad (\text{A.4})$$

The time evolution of single node marginals is given by

$$\dot{P}_n^t [y_n] = \sum_{y \setminus y_n} \sum_x W_{y,x} P^t [x]. \quad (\text{A.5})$$

Fixing the occupation $y_n = 1$, the nonzero contributions in the sum (A.1) are those for n and $n - 1$

$$\begin{aligned} \sum_{y \setminus y_n} \sum_x W_{y,x}^{n-1} P^t[x] &= \sum_{y \setminus y_n} (1 - y_{n-1}) P^t[y_1 \dots y_{n-2} 1 0 \dots y_N] = P_{n-1}^t[10], \\ \sum_{y \setminus y_n} \sum_x W_{y,x}^n P^t[x] &= \sum_{y \setminus y_n} (y_{n+1} - 1) P^t[y_1 \dots y_{n-1} 1 0 \dots y_N] = -P_n^t[10]. \end{aligned}$$

Thus, we obtain

$$\dot{P}_n^t[1] = P_{n-1}^t[10] - P_n^t[10], \quad (\text{A.6})$$

which is the continuity equation (2.3).

The dynamical equations for the two-node marginals can be written as

$$\dot{P}_n^t[y_n y_{n+1}] = \sum_{y \setminus \{y_n, y_{n+1}\}} \sum_x W_{y,x} P^t[x]. \quad (\text{A.7})$$

Fixing the occupation numbers $y_n = 1$ and $y_{n+1} = 0$, we get

$$\begin{aligned} \sum_{y \setminus \{y_n, y_{n+1}\}} \sum_x W_{y,x}^{n-1} P^t[x] &= \sum_{y \setminus \{y_n, y_{n+1}\}} (1 - y_{n-1}) P^t[y_1 \dots y_{n-2} 1 0 0, \dots, y_N] \\ &= P_{n-1}^t[100], \\ \sum_{y \setminus \{y_n, y_{n+1}\}} \sum_x W_{y,x}^n P^t[x] &= \sum_{y \setminus \{y_n, y_{n+1}\}} (y_{n+1} - y_n) P^t[y_1 \dots y_{n-1} 1 0 \dots y_N] \\ &= -P_n^t[10], \\ \sum_{y \setminus \{y_n, y_{n+1}\}} \sum_x W_{y,x}^{n+1} P^t[x] &= \sum_{y \setminus \{y_n, y_{n+1}\}} y_{n+2} P^t[y_1 \dots y_{n-1} 1 1 0 \dots y_N] \\ &= P_n^t[110]. \end{aligned}$$

Thence, we obtain the equation (2.4)

$$\dot{P}_n^t[10] = P_{n-1}^t[100] + P_n^t[110] - P_n^t[10]. \quad (\text{A.8})$$

A.2 AS model

For the AS model, the hopping processes at $n = 1, \dots, N - 2$ are defined by

$$\begin{aligned} W_{y,x}^{1,n} &= \eta \delta(y_1, x_1) \dots \delta(y_{n-1}, x_{n-1}) x_n (1 - x_{n+1}) x_{n+2} (y_{n+1} - y_n) \cdot \\ &\quad \times \delta(y_{n+2}, x_{n+2}) \dots \delta(y_N, x_N), \end{aligned} \quad (\text{A.9})$$

$$\begin{aligned} W_{y,x}^{2,n} &= \theta \delta(y_1, x_1) \dots \delta(y_{n-1}, x_{n-1}) x_n (1 - x_{n+1}) (1 - x_{n+2}) (y_{n+1} - y_n) \cdot \\ &\quad \times \delta(y_{n+2}, x_{n+2}) \dots \delta(y_N, x_N). \end{aligned} \quad (\text{A.10})$$

The injection and extraction processes are defined by

$$W_{y,x}^{1,0} = \alpha_1 (1 - x_1) x_2 (2y_1 - 1) \delta(y_2, x_2) \cdot \dots \cdot \delta(y_N, x_N), \quad (\text{A.11})$$

$$W_{y,x}^{2,0} = \alpha_2 (1 - x_1) (1 - x_2) (2y_1 - 1) \delta(y_2, x_2) \cdot \dots \cdot \delta(y_N, x_N), \quad (\text{A.12})$$

$$W_{y,x}^{N-1} = \beta_1 \delta(y_1, x_1) \cdot \dots \cdot \delta(y_{N-2}, x_{N-2}) x_{N-1} (1 - x_N) (y_N - y_{N-1}), \quad (\text{A.13})$$

$$W_{y,x}^N = \beta_2 \delta(y_1, x_1) \cdot \dots \cdot \delta(y_{N-1}, x_{N-1}) x_N (1 - 2y_N). \quad (\text{A.14})$$

We fix $y_n = 1$ and we consider the time evolution of local densities: the nonzero contributions in (A.1) are again those for n and $n - 1$

$$\begin{aligned} \sum_{y \setminus y_n} \sum_x W_{y,x}^{1,n-1} P^t[x] &= \eta \sum_{y \setminus y_n} (1 - y_{n-1}) P^t[y_1 \dots y_{n-2} 1 0 1 \dots y_N] = \eta P_{n-1}^t[101], \\ \sum_{y \setminus y_n} \sum_x W_{y,x}^{2,n-1} P^t[x] &= \theta \sum_{y \setminus y_n} (1 - y_{n-1}) P^t[y_1 \dots y_{n-2} 1 0 0 \dots y_N] = \theta P_{n-1}^t[100], \\ \sum_{y \setminus y_n} \sum_x W_{y,x}^{1,n} P^t[x] &= \eta \sum_{y \setminus y_n} (y_{n+1} - 1) P^t[y_1 \dots y_{n-1} 1 0 1 \dots y_N] = -\eta P_n^t[101], \\ \sum_{y \setminus y_n} \sum_x W_{y,x}^{2,n} P^t[x] &= \theta \sum_{y \setminus y_n} (y_{n+1} - 1) P^t[y_1 \dots y_{n-1} 1 0 0 \dots y_N] = -\theta P_n^t[100]. \end{aligned}$$

From these contributions, we obtain

$$\dot{P}_n^t[1] = \eta P_{n-1}^t[101] + \theta P_{n-1}^t[100] - \eta P_n^t[101] - \theta P_n^t[100], \quad (\text{A.15})$$

which is still a continuity equation with the generalized current definition (1.8).

Then, we fix the occupations $y_n = 1$ and $y_{n+1} = 0$ to write the time evolution equations for two-node marginals. We start with the terms in n

$$\begin{aligned} \sum_{y \setminus \{y_n, y_{n+1}\}} \sum_x W_{y,x}^{1,n} P^t[x] &= \eta \sum_{y \setminus \{y_n, y_{n+1}\}} (y_{n+1} - y_n) P^t[y_1 \dots y_{n-1} 1 0 1 \dots y_N] \\ &= -\eta P_n^t[101], \\ \sum_{y \setminus \{y_n, y_{n+1}\}} \sum_x W_{y,x}^{2,n} P^t[x] &= \theta \sum_{y \setminus \{y_n, y_{n+1}\}} (y_{n+1} - y_n) P^t[y_1 \dots y_{n-1} 1 0 0 \dots y_N] \\ &= -\theta P_n^t[100]. \end{aligned}$$

We write the passages in detail for the terms in $n - 1$ and $n + 1$

$$\begin{aligned}
 \sum_{y \setminus \{y_n, y_{n+1}\}} \sum_x W_{y,x}^{1,n-1} P^t[x] &= \eta \sum_{y \setminus \{y_n, y_{n+1}\}} \sum_x \delta(y_1, x_1) \cdots \delta(y_{n-2}, x_{n-2}) x_{n-1} (1 - x_n) \cdot \\
 &\quad \times x_{n+1} (1 - y_{n-1}) \delta(y_{n+1}, x_{n+1}) \cdots \delta(y_N, x_N) P^t[x_1 \dots x_N] \\
 &= \eta \sum_{y \setminus \{y_n, y_{n+1}\}} (1 - y_{n-1}) y_{n+1} P^t[y_1 \dots y_{n-2} 1 0 y_{n+1} \dots y_N] = 0, \\
 \sum_{y \setminus \{y_n, y_{n+1}\}} \sum_x W_{y,x}^{2,n-1} P^t[x] &= \theta \sum_{y \setminus \{y_n, y_{n+1}\}} \sum_x \delta(y_1, x_1) \cdots \delta(y_{n-2}, x_{n-2}) x_{n-1} (1 - x_n) \cdot \\
 &\quad \times (1 - x_{n+1}) (1 - y_{n-1}) \delta(y_{n+1}, x_{n+1}) \cdots \delta(y_N, x_N) P^t[x_1 \dots x_N] \\
 &= \theta \sum_{y \setminus \{y_n, y_{n+1}\}} (1 - y_{n-1}) (1 - y_{n+1}) P^t[y_1 \dots y_{n-2} 1 0 y_{n+1} \dots y_N] \\
 &= \theta P_{n-1}^t[100], \\
 \sum_{y \setminus \{y_n, y_{n+1}\}} \sum_x W_{y,x}^{1,n+1} P^t[x] &= \eta \sum_{y \setminus \{y_n, y_{n+1}\}} \sum_x \delta(y_1, x_1) \cdots \delta(y_n, x_n) x_{n+1} (1 - x_{n+2}) \cdot \\
 &\quad \times x_{n+3} y_{n+2} \delta(y_{n+3}, x_{n+3}) \cdots \delta(y_N, x_N) P^t[x_1 \dots x_N] \\
 &= \eta \sum_{y \setminus \{y_n, y_{n+1}\}} y_{n+2} P^t[y_1 \dots y_{n-1} 1 1 0 1 \dots y_N] = \eta P_n^t[1101], \\
 \sum_{y \setminus \{y_n, y_{n+1}\}} \sum_x W_{y,x}^{2,n+1} P^t[x] &= \theta \sum_{y \setminus \{y_n, y_{n+1}\}} \sum_x \delta(y_1, x_1) \cdots \delta(y_n, x_n) x_{n+1} (1 - x_{n+2}) \cdot \\
 &\quad \times (1 - x_{n+3}) y_{n+2} \delta(y_{n+3}, x_{n+3}) \cdots \delta(y_N, x_N) P^t[x_1 \dots x_N] \\
 &= \theta \sum_{y \setminus \{y_n, y_{n+1}\}} y_{n+2} P^t[y_1, \dots, y_{n-1} 1 1 0 0 \dots y_N] = \theta P_n^t[1100].
 \end{aligned}$$

Putting all these contributions together, we obtain

$$\dot{P}_n^t[10] = \theta P_{n-1}^t[100] + \theta P_n^t[1100] + \eta P_n^t[1101] - J_n(t),$$

which coincides with equation (2.21).

Appendix B

Proofs of analytical results in chapter 5

B.1 Bounds for the density and current profiles

In this appendix we report the complete proof of Theorem 1 and Corollary 1, under the hypotheses (2.11), (5.33) and (5.34) on the model parameters. We start by proving useful auxiliary results that are employed in the following

Lemma 9. *Let $(r_n)_{n=0}^{N+1}$ be the sequence of detrended densities, defined as in section 5.2.1, with boundary values $r_0 = \alpha$ and $r_{N+1} = q_0$. Then*

$$\begin{cases} \alpha \geq r_n \geq r_{n+1} \geq q_0 & \text{if } \alpha \geq q_0 \\ \alpha \leq r_n \leq r_{n+1} \leq q_0 & \text{if } \alpha \leq q_0 \end{cases} \quad n = 1, \dots, N-1, \quad (\text{B.1})$$

$$\begin{cases} r_{n-1}r_n' \geq r_n r_{n+1}' \geq q_0 q_0' & \text{if } \alpha \geq q_0 \\ r_{n-1}r_n' \leq r_n r_{n+1}' \leq q_0 q_0' & \text{if } \alpha \leq q_0 \end{cases} \quad n = 1, \dots, N. \quad (\text{B.2})$$

Proof From (2.9) with $\omega_A = \omega_D = \omega$, taking into account the definition (5.25) of detrended densities, by simple algebra one can write the equations

$$p_n (r_n - r_{n+1}) = (r_{n-1} - r_n) p_n' \quad n = 1, \dots, N. \quad (\text{B.3})$$

Now, since $0 < p_n < 1$, $n = 1, \dots, N$, we deduce that the quantities $r_n - r_{n+1}$, for $n = 0, \dots, N$, must all have the same sign or they must be all zero, so that the sequence $(r_n)_{n=0}^{N+1}$ must be strictly monotonic or constant, respectively. We can thus write

$$\begin{cases} r_0 \geq r_n \geq r_{n+1} \geq r_{N+1} & \text{if } r_0 \geq r_{N+1} \\ r_0 \leq r_n \leq r_{n+1} \leq r_{N+1} & \text{if } r_0 \leq r_{N+1} \end{cases} \quad n = 1, \dots, N-1. \quad (\text{B.4})$$

With the given boundary values, (B.1) follows immediately. Furthermore, from (5.26) we see that the condition $r_{n-1} \geq r_{n+1}$ implies $r_{n-1}r_n' \geq r_n r_{n+1}'$, for $n = 1, \dots, N$ and the same with opposite inequalities. As a consequence we have

$$\begin{cases} r_{n-1}r_n' \geq r_n r_{n+1}' \geq r_N r_{N+1}' & \text{if } r_0 \geq r_{N+1} \\ r_{n-1}r_n' \leq r_n r_{n+1}' \leq r_N r_{N+1}' & \text{if } r_0 \leq r_{N+1} \end{cases} \quad n = 1, \dots, N-1. \quad (\text{B.5})$$

With the given boundary value $r_{N+1} = q_0$, using (B.1) and taking into account that $q_0' > 0$, we finally obtain (B.2).

Lemma 10. *Let $(q_n)_{n=0}^{N+1}$ be the sequence of bulk densities, defined as in section 5.2.1. Then, the following inequalities hold*

$$q_0 q_0' \geq q_{n-1} q_n' \geq q_n q_{n+1}' \geq q_0 q_0' - C\omega(n+1) \quad n = 1, \dots, N. \quad (\text{B.6})$$

Proof Using the bulk-density expression $q_n = q_0 + \omega n$, we see that

$$q_n q_{n+1}' = q_0 q_0' - \omega q_0 - \omega n [q_0 - q_0' + \omega(n+1)] \quad n = 0, \dots, N, \quad (\text{B.7})$$

where we notice that $q_0 - q_0' > 0$, since by hypothesis $q_0 > 1/2$. As a consequence, $q_n q_{n+1}'$ is either constant (for $\Omega = 0$) or decreasing in n (for $\Omega > 0$) and the upper-bound is evident. The lower-bound easily follows observing that $\omega(n+1) \leq \Omega$.

B.1.1 Proof of Theorem 1

Let us define the sequences

$$\varrho_n \equiv \begin{cases} r_n - q_0 & \text{if } \alpha \geq q_0 \\ q_0 - r_n & \text{if } \alpha \leq q_0 \end{cases} \quad n = 0, \dots, N+1, \quad (\text{B.8})$$

$$\varepsilon_n \equiv \begin{cases} r_n r_{n+1}' - q_0 q_0' & \text{if } \alpha \geq q_0 \\ q_0 q_0' - r_n r_{n+1}' & \text{if } \alpha \leq q_0 \end{cases} \quad n = 0, \dots, N, \quad (\text{B.9})$$

$$\delta_n \equiv \begin{cases} s_n - r_n & \text{if } \alpha \geq q_0 \\ r_n - s_n & \text{if } \alpha \leq q_0 \end{cases} \quad n = 0, \dots, N+1. \quad (\text{B.10})$$

We observe that the above definitions are consistent also in the case $\alpha = q_0$, because, according to (5.36) in Lemma 1 and (B.1) in Lemma 9, in that case we have $r_n = s_n = q_0$ for all n , thus all three sequences are constantly equal to zero. Now, from (B.8) and (B.1) we get

$$\varrho_n \geq 0 \quad n = 0, \dots, N+1, \quad (\text{B.11})$$

which allows us to write

$$\varrho_n = |r_n - q_0| \quad n = 0, \dots, N + 1. \quad (\text{B.12})$$

Moreover, from (B.9) and (B.2) we get

$$\varepsilon_n \geq 0 \quad n = 0, \dots, N, \quad (\text{B.13})$$

which also allows us to write

$$\varepsilon_n = |r_n r_{n+1}' - q_0 q_0'| \quad n = 0, \dots, N. \quad (\text{B.14})$$

Furthermore, using (B.9), (B.10) and (5.30) (Lemma 1), we can write

$$\varepsilon_n = r_n \delta_{n+1} - s_{n+1}' \delta_n \quad n = 0, \dots, N. \quad (\text{B.15})$$

Using (B.1) in Lemma 9, along with $q_0 > 0$ and $\alpha > 0$, we see that r_n is positive for all n , so that from (B.13) and (B.15) we can write

$$\delta_{n+1} \geq \frac{s_{n+1}'}{r_n} \delta_n \quad n = 0, \dots, N, \quad (\text{B.16})$$

where Lemma 1 ensures that the term s_{n+1}'/r_n is positive as well for all n . Again by the Lemma 1, $s_0 = \alpha$, so with $r_0 = \alpha$ we have $\delta_0 = 0$. Then, applying recursively the above inequality, we arrive at

$$\delta_n \geq 0 \quad n = 0, \dots, N + 1, \quad (\text{B.17})$$

which also allows us to write

$$\delta_n = |s_n - r_n| \quad n = 0, \dots, N + 1. \quad (\text{B.18})$$

So far, we have proved that ϱ_n , ε_n and δ_n are all non-negative quantities. We now prove upper-bounds for the same quantities: before entering the details, we give a sketch of the main steps needed for this proof. First, making use of Lemma 1 and of the lower-bounds (B.11) and (B.17), we prove the upper-bounds for ϱ_n and ε_n . Subsequently, using the upper-bound for ε_n together with (B.15), we also get the upper-bound for δ_n , i.e. the thesis.

Upper-bound for ϱ_n The following bounds are easily deduced from Lemma 1

$$\begin{cases} s_n \leq q_0 + C\gamma^n & \text{if } \alpha \geq q_0 \\ s_n \geq q_0 - C\gamma^n & \text{if } \alpha \leq q_0 \end{cases} \quad n = 0, 1, 2, \dots \quad (\text{B.19})$$

Moreover, by (B.17) and (B.10), we can write

$$\begin{cases} r_n \leq s_n & \text{if } \alpha \geq q_0 \\ r_n \geq s_n & \text{if } \alpha \leq q_0 \end{cases} \quad n = 0, \dots, N + 1, \quad (\text{B.20})$$

and therefore, with the definition (B.8),

$$\varrho_n \leq C\gamma^n \quad n = 0, \dots, N + 1. \quad (\text{B.21})$$

Taking into account (B.12), this is equivalent to

$$|r_n - q_0| \leq C\gamma^n \quad n = 0, \dots, N + 1. \quad (\text{B.22})$$

Upper-bound for ε_n Let us observe that one can write, in full generality,

$$\varepsilon_n = \sum_{k=n+1}^N (\varepsilon_{k-1} - \varepsilon_k) + \varepsilon_N \quad n = 0, \dots, N - 1. \quad (\text{B.23})$$

Taking into account, in order, (5.26) with (B.8) and (B.9), (B.11), and finally (B.21), we get

$$\varepsilon_{n-1} - \varepsilon_n = \omega n (\varrho_{n-1} - \varrho_{n+1}) \leq \omega n \varrho_{n-1} \leq C\omega n \gamma^{n-1} \quad n = 1, \dots, N. \quad (\text{B.24})$$

Moreover, using (B.8) and (B.9) with $r_{N+1} = q_0$, and then (B.21) with $q_0' > 0$, we have

$$\varepsilon_N = \varrho_N q_0' \leq C\gamma^N. \quad (\text{B.25})$$

Now, we distinguish the pure TASEP from the TASEP-LK. In the former case we have $\omega = 0$, so that (B.24) reads $\varepsilon_{n-1} - \varepsilon_n = 0$. Then from (B.23) and (B.25) we get

$$\varepsilon_n \leq C\gamma^N \quad n = 0, \dots, N. \quad (\text{B.26})$$

Otherwise, in the TASEP-LK, we have $\omega = \Omega/(N + 1)$ with $\Omega > 0$, so that (B.24) reads $\varepsilon_{n-1} - \varepsilon_n \leq Cn\gamma^{n-1}/(N + 1)$. Then from (B.23) and (B.25) we get

$$\varepsilon_n \leq \frac{C}{N + 1} \sum_{k=n+1}^{N+1} k\gamma^{k-1} \quad n = 0, \dots, N. \quad (\text{B.27})$$

Recalling (5.39), we can manipulate the sum as follows

$$\sum_{k=n+1}^{N+1} k\gamma^{k-1} < \sum_{k=n+1}^{\infty} k\gamma^{k-1} = \frac{(n + 1)\gamma^n - n\gamma^{n+1}}{(1 - \gamma)^2}. \quad (\text{B.28})$$

We then have

$$\varepsilon_n \leq C \frac{(n + 1)\gamma^n}{N} \quad n = 0, \dots, N, \quad (\text{B.29})$$

where we have legitimately replaced $N + 1$ with N in the denominator. The announced upper-bounds for ε_n have been obtained, (B.26) for $\Omega = 0$ and (B.29) for $\Omega > 0$. Taking into account (B.14), they are equivalent to

$$|r_n r_{n+1}' - q_0 q_0'| \leq \begin{cases} C\gamma^N & \text{if } \Omega = 0 \\ C \frac{(n+1)\gamma^n}{N} & \text{if } \Omega > 0 \end{cases} \quad n = 0, \dots, N. \quad (\text{B.30})$$

Upper-bound for δ_n We replace ε_n with the expression given by (B.15). Using the fact that, by virtue of Lemma 9 with $q_0 > 0$ and $\alpha > 0$, the quantities r_n are bounded from below by a positive constant, we can write, for $\Omega = 0$,

$$\delta_{n+1} \leq \frac{s_{n+1}'}{r_n} \delta_n + C\gamma^N \quad n = 0, \dots, N, \quad (\text{B.31})$$

and, for $\Omega > 0$,

$$\delta_{n+1} \leq \frac{s_{n+1}'}{r_n} \delta_n + C \frac{(n+1)\gamma^n}{N} \quad n = 0, \dots, N, \quad (\text{B.32})$$

where, by Lemmas 1 and 9, the term s_{n+1}'/r_n is known to be always positive and bounded by a constant. First we consider the case $\Omega = 0$. Recalling that $\delta_0 = 0$ and applying recursively (B.31), the following bound is obtained

$$\delta_n \leq C\gamma^N \quad n = 0, \dots, N + 1. \quad (\text{B.33})$$

Taking into account (B.18), this is equivalent to the thesis of Theorem 1, for the case $\Omega = 0$. The case $\Omega > 0$ is slightly more complicated. We apply recursively (B.32) to get

$$\delta_n \leq \frac{C}{N} \sum_{k=0}^n k\gamma^{k-1} \prod_{l=k}^{n-1} \frac{s_{l+1}'}{r_l} \quad n = 0, \dots, N + 1. \quad (\text{B.34})$$

Now, we discuss the cases $\alpha \geq q_0$ and $\alpha < q_0$ separately. In the former case, from (B.20) and (B.1), along with $\gamma = q_0'/q_0$, we easily get

$$\frac{s_{n+1}'}{r_n} \leq \gamma \quad n = 0, \dots, N, \quad (\text{B.35})$$

and therefore

$$\delta_n \leq \frac{C}{N} \left(\sum_{k=0}^n k \right) \gamma^{n-1} \leq C \frac{n^2 \gamma^n}{N} \quad n = 0, \dots, N + 1. \quad (\text{B.36})$$

Taking into account (B.18), this is equivalent to the thesis of Theorem 1, for the case $\Omega > 0$. The last step to complete the proof is to show that (B.36) holds even in the complementary hypothesis $\alpha < q_0$. In such a case, (B.20) and (B.1) imply the opposite of (B.35), so that we cannot apply the above argument. Nevertheless, we can observe that, because of (B.19) and (B.20), both s_n and r_n approach q_0 exponentially upon increasing n . As a consequence, the term s_{n+1}'/r_n approaches γ exponentially as well, which entails that in (B.34) it should be possible to write

$$\prod_{l=k}^{n-1} \frac{s_{l+1}'}{r_l} \leq C\gamma^{n-k}, \quad (\text{B.37})$$

so that (B.36) can still be obtained.

B.1.2 Proof of Corollary 1

Let us recall the current-density relationship $J_n = p_n p_{n+1}'$, the definition of detrended densities (5.25), i.e. $p_n = r_n + \omega n$, and the bulk solution (5.24), i.e. $q_n = q_0 + \omega n$. By simple algebra we get for $n = 0, \dots, N$

$$J_n - q_n q_{n+1}' = (r_n r_{n+1}' - q_0 q_0') - \omega n (r_{n+1} - q_0) - \omega (n+1) (r_n - q_0), \quad (\text{B.38})$$

and thence, using the triangular inequality,

$$|J_n - q_n q_{n+1}'| \leq |r_n r_{n+1}' - q_0 q_0'| + \omega n |r_{n+1} - q_0| + \omega (n+1) |r_n - q_0|, \quad (\text{B.39})$$

for the same values of n . Equation (5.43) can be easily proved using (B.22) and (B.30) from inside the proof of Theorem 1. In order to prove also (5.44), we first note that, using again the triangular inequality, we can write

$$\begin{aligned} \left| \max_{n=0}^N (J_n) - q_0 q_0' \right| &\leq \left| \max_{n=0}^N (J_n) - \max_{n=0}^N (q_n q_{n+1}') \right| + \\ &+ \left| \max_{n=0}^N (q_n q_{n+1}') - q_0 q_0' \right|. \end{aligned} \quad (\text{B.40})$$

Now, given two generic sequences $(x_n)_{n=0}^N$ and $(y_n)_{n=0}^N$, the following inequality holds

$$\left| \max_{n=0}^N (x_n) - \max_{n=0}^N (y_n) \right| \leq \max_{n=0}^N (|x_n - y_n|), \quad (\text{B.41})$$

whereas Lemma 10 obviously entails

$$\max_{n=0}^N (q_n q_{n+1}') = q_0 q_1'. \quad (\text{B.42})$$

As a consequence we can write

$$\left| \max_{n=0}^N (J_n) - q_0 q_0' \right| \leq \max_{n=0}^N (|J_n - q_n q_{n+1}'|) + \omega q_0. \quad (\text{B.43})$$

Using (5.43), we can easily prove (5.44).

B.2 Asymptotic bounds for the slowest relaxation rate (balanced case)

B.2.1 Proof of Corollary 2

The proof is based on the *Courant minimax principle*, by which we can state both $\lambda = \min \{(u, Au)\}_{u \in \mathbb{R}^N: \|u\|=1}$ and $\mu = \min \{(u, Bu)\}_{u \in \mathbb{R}^N: \|u\|=1}$, therefore

$$|\lambda - \mu| \leq \max \{|(u, Au) - (u, Bu)|\}_{u \in \mathbb{R}^N: \|u\|=1}. \quad (\text{B.44})$$

To derive Corollary 2, we need to prove the bound for $|(u, Au) - (u, Bu)|$, where

$$(u, Au) - (u, Bu) = \sum_{n=1}^N (s_{n+1} - r_{n+1} - s_{n-1} + r_{n-1}) u_n^2 + 2 \sum_{n=1}^{N-1} \left(\sqrt{p_n p_{n+1}'} - \sqrt{q_n q_{n+1}'} \right) u_n u_{n+1}. \quad (\text{B.45})$$

First, using the triangular inequality, we can write

$$|(u, Au) - (u, Bu)| \leq \sum_{n=1}^N (|s_{n+1} - r_{n+1}| + |s_{n-1} - r_{n-1}|) u_n^2 + 2 \sum_{n=1}^{N-1} \left| \sqrt{p_n p_{n+1}'} - \sqrt{q_n q_{n+1}'} \right| |u_n| |u_{n+1}|, \quad (\text{B.46})$$

Then, from Theorem 1 we have, $\forall n$,

$$|s_{n+1} - r_{n+1}| + |s_{n-1} - r_{n-1}| \leq \begin{cases} C\gamma^N & \text{if } \Omega = 0 \\ CN^{-1} & \text{if } \Omega > 0 \end{cases}. \quad (\text{B.47})$$

Moreover, from Corollary 1 we obtain, for all n ,

$$|p_n p_{n+1}' - q_n q_{n+1}'| \leq \begin{cases} C\gamma^N & \text{if } \Omega = 0 \\ CN^{-1} & \text{if } \Omega > 0 \end{cases}, \quad (\text{B.48})$$

from which we derive an analogous bound for $|\sqrt{p_n p_{n+1}'} - \sqrt{q_n q_{n+1}'}|$. At this point, given a vector u such that $\sum_{n=1}^{N-1} u_n^2 = 1$, we have in particular that $\sum_{n=1}^{N-1} |u_n| |u_{n+1}| \leq 1$, thanks to the *Cauchy-Schwarz inequality*. Plugging the bounds (B.47) and (B.48) into (B.46), we conclude the proof.

B.2.2 Proof of Lemma 3

We denote by v an eigenvector of B corresponding to the smallest eigenvalue μ , so that $Bv = \mu v$. This vector can be chosen in such a way that $v_n = w_n$ for some $n \in \{1, \dots, N\}$ and $|v_k| \leq w_k$ for the other $k \neq n$ (even $k = 0$ and $k = N + 1$, by setting $v_0 \equiv v_{N+1} \equiv 0$). In practice, one can take n as an index corresponding to the maximum of $\{|v_1|/w_1, \dots, |v_N|/w_N\}$ and then normalize v by v_n/w_n . This argument entails that $v_n \neq 0$, thus we can write $\mu = Bv_n/v_n$, that is

$$\mu = 1 - (s_{n+1} - s_{n-1}) - \sqrt{q_n q_{n+1}'} \frac{v_{n+1}}{v_n} - \sqrt{q_{n-1} q_n'} \frac{v_{n-1}}{v_n}. \quad (\text{B.49})$$

Then, using $v_n = w_n > 0$ and $v_{n\pm 1} \leq w_{n\pm 1}$, we obtain the following bound

$$\mu \geq 1 - (s_{n+1} - s_{n-1}) - \sqrt{q_n q_{n+1}'} \frac{w_{n+1}}{w_n} - \sqrt{q_{n-1} q_n'} \frac{w_{n-1}}{w_n}. \quad (\text{B.50})$$

By Lemma 10 we have that $q_n q_{n+1}' \leq q_{n-1} q_n' \leq q_0 q_0'$, thus the bound becomes

$$\mu \geq 1 - \left(s_{n+1} - s_{n-1} + \sqrt{q_0 q_0'} \frac{w_{n+1} + w_{n-1}}{w_n} \right). \quad (\text{B.51})$$

Now, we observe that in general one cannot foresee the proper index n , so that we are forced to choose the worst case. Using the definition of x_\circ (5.35), we conclude the proof.

B.2.3 Proof of Lemma 5

In order to use the Courant-type bound (Lemma 2), we define a trial vector. For a given integer $M > 1$, we consider the sequence

$$y_n \equiv \sqrt{\frac{2}{M}} \sin \frac{\pi n}{M}, \quad (\text{B.52})$$

then we take the vector u with components

$$u_n \equiv \begin{cases} y_n & \text{if } n \leq M \\ 0 & \text{if } n \geq M \end{cases}, \quad (\text{B.53})$$

where $n = 1, \dots, N$ and $M \geq 2$. We assume $M \leq N + 1$, so that the above definition verifies $\sum_{n=1}^N u_n^2 = 1$, as required by Lemma 2. Moreover, it satisfies the property

$$\sum_{n=1}^{M-2} u_n u_{n+1} = \cos \frac{\pi}{M}. \quad (\text{B.54})$$

We rewrite equation (5.48) according to this choice for u_n

$$\mu \leq 1 + \sum_{n=1}^{M-1} (s_{n-1} - s_{n+1}) u_n^2 - 2 \sum_{n=1}^{M-2} \sqrt{q_n q_{n+1}'} u_n u_{n+1}. \quad (\text{B.55})$$

From Lemma 1 we can easily deduce the bound $s_{n-1} - s_{n+1} \leq C\gamma^n$. Taking also into account that $\sin x \leq x$ for all real non-negative x , we can write

$$\sum_{n=1}^{M-1} (s_{n-1} - s_{n+1}) u_n^2 \leq \frac{C}{M^3}. \quad (\text{B.56})$$

As regards the second sum in (B.55), by Lemma 10 we have that $q_n q_{n+1}' \geq q_{M-2} q_{M-1}'$ for all $n = 1, \dots, M - 2$. Using also (B.54), we obtain

$$\sum_{n=1}^{M-2} \sqrt{q_n q_{n+1}'} u_n u_{n+1} \geq \sqrt{q_{M-2} q_{M-1}'} \cos \frac{\pi}{M}. \quad (\text{B.57})$$

Using the results (B.56) and (B.57) in (B.55), we reach the inequality

$$\mu \leq 1 + \frac{C}{M^3} - 2\sqrt{q_{M-2}q_{M-1}'} \cos \frac{\pi}{M}. \quad (\text{B.58})$$

Now, we use the property $\cos(\pi/M) \geq 1 - \frac{1}{2}(\pi/M)^2$ and, applying again Lemma 10, we show that $\sqrt{q_{M-2}q_{M-1}'} \geq \sqrt{q_0q_0'} - C\Omega M/N$. Hence, we get

$$\mu \leq 1 - 2\sqrt{q_0q_0'} + \pi^2\sqrt{q_0q_0'} M^{-2} + C\Omega MN^{-1} + CM^{-3}. \quad (\text{B.59})$$

In the pure TASEP case we have $\Omega = 0$ and the term in MN^{-1} disappears: the most restrictive bound can be attained choosing M as large as possible, i.e. $M = N + 1$, which allows us to write

$$\mu \leq 1 - 2\sqrt{q_0q_0'} + \pi^2\sqrt{q_0q_0'} N^{-2} + CN^{-3}. \quad (\text{B.60})$$

The term in N^{-3} may be dropped, provided the prefactor of N^{-2} is replaced by a suitable constant C .

In the TASEP-LK case, the terms in M^{-2} and MN^{-1} are both present: one can realize that the most restrictive bound is attained when they have the same asymptotic order, that is choosing M of the order of $N^{1/3}$. We then obtain

$$\mu \leq 1 - 2\sqrt{q_0q_0'} + CN^{-2/3} + CN^{-1}, \quad (\text{B.61})$$

where the term in N^{-1} may obviously be dropped. Using the definition of x_\circ (5.35), we conclude the proof.

B.2.4 Proof of Lemma 6

Statement (i) We need to use some results from the theory of difference equations, for which we refer to [37].

A generic sequence $(w_n)_{n=0}^\infty$ is said to be *nonoscillatory* if the sequence $(w_n w_{n+1})_{n=0}^\infty$ is eventually positive (there exists $n > 0$ such that w_k is either positive or negative $\forall k > n$), and *oscillatory* otherwise. We can easily show that our sequence $(v_n(x))_{n=0}^\infty$ is nonoscillatory for $x > 1$ (see [37], Theorem 6.5.5) and oscillatory for $x < 1$ (see [37], Theorem 6.5.3). To study the case $x = 1$, we consider the sequence $(s_n)_{n=0}^\infty$ and we define

$$\xi_n \equiv 2x_\circ (s_{n+1} - s_{n-1}) \quad n = 1, 2, \dots \quad (\text{B.62})$$

Since we are in the hypothesis $\alpha < q_0$, by Lemma 1 we have that $\xi_n > 0$ for all n and $\xi_n \rightarrow 0$ for $n \rightarrow \infty$, with an exponential decay. Then, there must exist an integer $m > 0$ such that $(2 \sum_{i=n}^\infty \xi_i)^2 \leq \xi_n$ for all $n \geq m$. We define the sequence $(w_n)_{n=0}^\infty$ as

$$w_n \equiv \begin{cases} 0 & \text{if } n < m \\ \prod_{k=m}^n (1 + 2 \sum_{i=k}^\infty \xi_i) & \text{if } n \geq m \end{cases}. \quad (\text{B.63})$$

For $n \geq m$, we have both $w_n > 0$ and

$$w_{n+1} - (2 - \xi_n)w_n + w_{n-1} \leq \left[\frac{(2 \sum_{i=n}^{\infty} \xi_i)^2}{1 + 2 \sum_{i=n}^{\infty} \xi_i} - \xi_n \right] w_n \leq 0. \quad (\text{B.64})$$

Finally, invoking Corollary 6.8.3 in [37], we can directly prove that the sequence $(v_n(1))_{n=0}^{\infty}$ is nonoscillatory.

Statement (ii) We start with the following result in [37] (Theorem 6.8.1).

If $(\bar{w}_n)_{n=0}^{\infty}$ and $(\underline{w}_n)_{n=0}^{\infty}$ are two sequences satisfying, for all $n > 0$, the relationships $\bar{w}_{n+1} + \bar{w}_{n-1} = \bar{\kappa}_n \bar{w}_n$ and $\underline{w}_{n+1} + \underline{w}_{n-1} = \underline{\kappa}_n \underline{w}_n$ with $\bar{w}_0 = \underline{w}_0$ and $\bar{w}_1 = \underline{w}_1$, and if $\underline{w}_n > 0$ and $\bar{\kappa}_n \geq \underline{\kappa}_n$ for all $n > 0$, then $\bar{w}_n \geq \underline{w}_n$ for all n .

We assume in particular $\bar{w}_0 \equiv \underline{w}_0 \equiv 0$ and $\bar{w}_1 \equiv \underline{w}_1 \equiv 1$. Setting $\bar{\kappa}_n \equiv 2x - \xi_n$ and $\underline{\kappa}_n \equiv 2$ entails $\bar{w}_n = v_n(x)$ and $\underline{w}_n = n$, so that, if x is such that $2x - \xi_n \geq 2$ for all $n > 0$, from the theorem above we get $v_n(x) \geq n > 0$ for all $n > 0$. The required x exists, because, by (B.62) and Lemma 1, the sequence $(\xi_n)_{n=1}^{\infty}$ is bounded. Furthermore, setting $\bar{\kappa}_n \equiv 2y - \xi_n$ and $\underline{\kappa}_n \equiv 2x - \xi_n$ entails $\bar{w}_n = v_n(y)$ and $\underline{w}_n = v_n(x)$, so that, if $y \geq x$, we get $v_n(y) \geq v_n(x) \forall n$. By this argument we realize that the set \mathcal{X} of all real numbers x with the property that $v_n(x) > 0$ for all $n > 0$ is an infinite interval. Using statement (i), we see that this set is contained in $[1, \infty)$ because the sequence $(v_n(x))_{n=0}^{\infty}$ is oscillatory when $x < 1$. Moreover, the set \mathcal{X} is closed, because we can prove that, if a sequence $(x_k)_{k=1}^{\infty} \subseteq \mathcal{X}$ converges to x_{∞} , then $x_{\infty} \in \mathcal{X}$. Keeping in mind that the functions $v_n(x)$ of the variable x are continuous (they are polynomials), by hypothesis we have $v_n(x_k) > 0$ for all $k > 0$ and $n > 0$, which implies $v_n(x_{\infty}) \geq 0$ for each $n > 0$, once k is sent to infinity. The number x_{∞} belongs to \mathcal{X} if the stronger condition $v_n(x_{\infty}) > 0$ is satisfied for all $n > 0$, which can be proved by contradiction as follows. If there were an integer $m > 1$ such that $v_m(x_{\infty}) = 0$, then, according to (5.16), we would find $v_{m+1}(x_{\infty}) + v_{m-1}(x_{\infty}) = 0$. This would imply both $v_{m+1}(x_{\infty})$ and $v_{m-1}(x_{\infty})$ being equal to zero, because $v_n(x_{\infty}) \geq 0$ for all n , and therefore $v_n(x_{\infty}) = 0$ for all n , contradicting the fact that $v_1(x_{\infty}) = 1$.

So far we have proved that $\mathcal{X} = [x_*, \infty)$ with $x_* \geq 1$. The remaining point to be proved to complete statement (ii) is $x_* < x_{\circ}$. First of all, we note that $x_{\circ} > 1$, because $q_0 = (\beta + \Omega)' > 1/2$ according to the hypothesis (5.33). The proof of this last point consists of two parts: in a preliminary step, we study the sequence $(v_n(x_{\circ}))_{n=0}^{\infty}$, showing that it satisfies the condition $v_n(x_{\circ}) > 0$ for all $n > 0$, which entails $x_{\circ} \in \mathcal{X}$ and thence the weak inequality $x_* \leq x_{\circ}$. Then we move to the strict inequality $x_* < x_{\circ}$ by proving that there exists $x < x_{\circ}$ such that $v_n(x) > 0$ for all $n > 0$.

We define the sequence

$$\sigma_n \equiv 2x_{\circ} s_n \quad n = 0, 1, 2, \dots \quad (\text{B.65})$$

and we observe that, using (5.30) and (5.35), it is possible to write, for all $n > 0$

$$2x_\circ - 2x_\circ(s_{n+1} - s_{n-1}) = \frac{1}{\sigma_n} + \sigma_{n-1}. \quad (\text{B.66})$$

By (5.16), we obtain

$$\left[v_{n+1}(x_\circ) - \frac{v_n(x_\circ)}{\sigma_n} \right] = \sigma_{n-1} \left[v_n(x_\circ) - \frac{v_{n-1}(x_\circ)}{\sigma_{n-1}} \right] \quad (\text{B.67})$$

for all $n > 0$, with $v_0(x_\circ) = 0$ and $v_1(x_\circ) = 1$. We observe that the terms in square brackets are the same with shifted indices and, by Lemma 1, we have $\sigma_n > 0$ for all n . Thence, we can prove by induction that the condition $v_{n+1}(x_\circ) > v_n(x_\circ)/\sigma_n > 0$, which is obviously verified for $n = 1$, holds for all $n > 0$.

Now we start the second step. First of all we observe that, using in order (B.65), (5.35), Lemma 1 and (5.39), we can write

$$\lim_{n \rightarrow \infty} \sigma_n = \lim_{n \rightarrow \infty} \frac{s_n}{\sqrt{q_0 q_0'}} = \sqrt{\frac{q_0}{q_0'}} = \frac{1}{\sqrt{\gamma}} > 1. \quad (\text{B.68})$$

As a consequence, there must exist an integer $m > 0$ such that $\sigma_m > 1$. We define the function

$$c(x) \equiv 1 + 2(x - x_\circ) \left(\sigma_m - \frac{1}{\sigma_m} \right)^{-1}. \quad (\text{B.69})$$

We have previously proved that the condition $v_{n+1}(x_\circ) > v_n(x_\circ)/\sigma_n > 0$ holds for all $n > 0$ and we note that $c(x_\circ) = 1$. Thence, by continuity, there must exist $x < x_\circ$ (x being close enough to x_\circ) such that the condition

$$v_{n+1}(x) > \frac{v_n(x)}{\sigma_n c(x)} > 0 \quad (\text{B.70})$$

can be satisfied up to a finite n , specifically for $n = 1, \dots, m$. We can choose x in such a way that

$$x \geq x_\circ - \frac{1}{2} \left(1 - \frac{\sigma_m}{\sigma_{m+1}} \right) \left(\sigma_m - \frac{1}{\sigma_m} \right), \quad (\text{B.71})$$

because by Lemma 1 in the hypothesis $\alpha < q_0$, the sequence $(\sigma_n)_{n=0}^\infty$ is strictly increasing, so that $\sigma_{m+1} > \sigma_m > 1$. Therefore, the right-hand side of (B.71) is strictly smaller than x_\circ . We see that (B.71) entails $c(x) \geq \sigma_m/\sigma_{m+1}$ and, since σ_n increases with n , we can write for all $n > m$

$$\sigma_m - \frac{1}{\sigma_m} \leq \sigma_{n-1} - \frac{1}{\sigma_n c(x)}. \quad (\text{B.72})$$

Observing that $c(x) < 1$, we plug the above inequality into (B.69) to obtain

$$2x - 2x_\circ \geq [c(x) - 1] \left[\sigma_{n-1} - \frac{1}{\sigma_n c(x)} \right] \quad (\text{B.73})$$

still for all $n > m$. Furthermore, from (B.66) we get

$$2x - 2x_\circ (s_{n+1} - s_{n-1}) \geq \frac{1}{\sigma_n c(x)} + \sigma_{n-1} c(x) \quad (\text{B.74})$$

for all $n > m$. We can show that this last inequality is a sufficient condition for (B.70) to hold even for all $n > m$. Indeed, combining (5.16) and (B.74) we see that, if for a given $n > m$ we have $v_n(x) > 0$, then

$$\left[v_{n+1}(x) - \frac{v_n(x)}{\sigma_n c(x)} \right] \geq \sigma_{n-1} c(x) \left[v_n(x) - \frac{v_{n-1}(x)}{\sigma_{n-1} c(x)} \right]. \quad (\text{B.75})$$

Starting from the case $n = m + 1$, for which we have proved that the condition $v_n(x) > v_{n-1}(x)/[\sigma_{n-1} c(x)] > 0$ is verified, we can proceed by induction to prove (B.70) for all $n > m$.

Statement (iii) We note that $\zeta(x)$ corresponds to the smaller root of the characteristic equation associated with the difference equation (5.16), without the terms in s_n

$$\zeta + \zeta^{-1} = 2x,$$

the other root being ζ^{-1} . Observing that $\zeta(x) > 0$ for all $x \geq 1$, we multiply both sides of (5.16) by $\zeta(x)^n$ to obtain for all $n > 0$

$$\begin{aligned} & \left[v_{n+1}(x) \zeta(x)^n - v_n(x) \zeta(x)^{n+1} \right] - \left[v_n(x) \zeta(x)^{n-1} - v_{n-1}(x) \zeta(x)^n \right] \\ & = -2x_\circ (s_{n+1} - s_{n-1}) v_n(x) \zeta(x)^n \end{aligned} \quad (\text{B.76})$$

We now sum over n with $v_0(x) = 0$ and $v_1(x) = 1$, divide by $\zeta(x)^{2n}$ and use definition (5.53). We get

$$\frac{v_{n+1}(x)}{\zeta(x)^n} - \frac{v_n(x)}{\zeta(x)^{n-1}} = \frac{1 - f_n(x)}{\zeta(x)^{2n}} \quad (\text{B.77})$$

for all $n \geq 0$. For $n = 0$, (B.77) gives the initial condition $v_1(x) = 1$, because $v_0(x) = 0$ implies $f_0(x) = 0$. Summing (B.77) over n , starting from any given k , we obtain for all $n > k$

$$\frac{v_n(x)}{\zeta(x)^{n-1}} = \frac{v_k(x)}{\zeta(x)^{k-1}} + \sum_{l=k}^{n-1} \frac{1 - f_l(x)}{\zeta(x)^{2l}}. \quad (\text{B.78})$$

We recall that for any given $x \geq 1$, the sequence $(v_n(x))_{n=0}^\infty$ is non-oscillatory, i.e. it is eventually positive or negative. We consider the positive case first. Since $s_{n+1} - s_{n-1}$ is always positive, we have that $f_n(x) > f_{n-1}(x)$ for all $n > m$, the sequence $(f_n(x))_{n=0}^\infty$ is eventually increasing. Consequently, using (B.78) we can write

$$0 < \frac{v_n(x)}{\zeta(x)^{n-1}} \leq \frac{v_k(x)}{\zeta(x)^{k-1}} + [1 - f_k(x)] \sum_{l=k}^{n-1} \frac{1}{\zeta(x)^{2l}} \quad (\text{B.79})$$

for all $k \geq m$ and for all $n > k$. Multiplying both sides of the latter inequality by $\zeta(x)^{2k}$, we obtain

$$f_k(x) < 1 + \frac{v_k(x)\zeta(x)^{k+1}}{\sum_{l=0}^{n-k-1} \zeta(x)^{-2l}} \quad (\text{B.80})$$

still for all $k \geq m$ and for all $n > k$. Finally, observing that the denominator diverges with n , we send the latter to infinity and we get

$$f_k(x) \leq 1 \quad (\text{B.81})$$

for all $k \geq m$. The limit (5.54) exists because the sequence $(f_n(x))_{n=0}^\infty$ is eventually increasing, whereas the result $f(x) \leq 1$ follows easily from (B.81).

In the case with $v_n(x) < 0$ for all $n > m$, from (5.53) it follows that $f_n(x) < f_{n-1}(x)$ for all $n > m$. By (B.78) we obtain a fully analogous argument with opposite inequalities and thence the result $f(x) \geq 1$.

Statement (iv) A consequence of statements (ii) and (iii) is that $f(x_*) \leq 1$, since $x_* \in \mathcal{X}$ and thence $v_n(x_*) > 0$ for all $n > 0$. In order to show that $f(x_*) = 1$ if $x_* > 1$, it is enough to prove that $f(x_*) \geq 1$ within this case. Keeping in mind that the $v_n(x)$ are continuous functions of x , we observe that, for each integer $k > 0$, there exists $x_k \in (1, x_*)$ such that $v_n(x) > 0$ for all $x \geq x_k$ and all $n = 1, \dots, k$, because $x_* > 1$ and $v_n(x_*) > 0$. We can choose x_k in such a way that $x_{k+1} \geq x_k$ for all $k > 0$, so that we have a non-decreasing sequence, being upper-bounded by x_* : this implies that the limit $x_\infty \equiv \lim_{k \rightarrow \infty} x_k$ exists and $x_\infty \leq x_*$. We prove by contradiction that $x_\infty = x_*$: if it was $x_\infty < x_*$, this would imply $x_* > \inf \mathcal{X}$, in contradiction with statement (ii).

Since $x_k \notin \mathcal{X}$ by construction, for any $k > 0$ there must exist some integer $l \geq k$ satisfying $v_{l+1}(x_k) \leq 0$. We denote by ℓ_k the smallest of these integers, thus $\ell_k \geq k$, while $v_n(x_k) > 0$ for all $n = 1, \dots, \ell_k$ and $v_{\ell_k+1}(x_k) \leq 0$. Using (B.77) for $x = x_k$ and $\ell = \ell_k$, we can write for any $k > 0$

$$\frac{v_{\ell_k+1}(x_k)}{\zeta(x_k)^{\ell_k}} - \frac{v_{\ell_k}(x_k)}{\zeta(x_k)^{\ell_k-1}} = \frac{1 - f_{\ell_k}(x_k)}{\zeta(x_k)^{2\ell_k}}. \quad (\text{B.82})$$

From what was said about $v_{\ell_k+1}(x_k)$ and $v_{\ell_k}(x_k)$, it follows that

$$f_{\ell_k}(x_k) > 1, \quad \forall k > 0. \quad (\text{B.83})$$

We now pick any integer $m > 0$ and consider $k > m$. We have that $\ell_k > m$ because $\ell_k \geq k$, then, by (B.83) and (5.53), we obtain

$$f_m(x_k) > 1 - 2x_\circ \sum_{n=m+1}^{\ell_k} (s_{n+1} - s_{n-1}) v_n(x_k) \zeta(x_k)^n. \quad (\text{B.84})$$

We find an upper bound for the term $v_n(x_k)\zeta(x_k)^n$ as follows. We rewrite (B.78) for $k = 0$,

$$\frac{v_n(x)}{\zeta(x)^{n-1}} = \sum_{l=0}^{n-1} \frac{1 - f_l(x)}{\zeta(x)^{2l}}, \quad \forall n > 0. \quad (\text{B.85})$$

We choose $x = x_k$ keeping in mind that, for all $n = 1, \dots, \ell_k$, we have $v_n(x_k) > 0$ and consequently $f_l(x_k) \geq 0$ for all $l = 0, \dots, \ell_k$. We deduce that

$$0 < \frac{v_n(x_k)}{\zeta(x_k)^{n-1}} \leq \sum_{l=0}^{n-1} \frac{1}{\zeta(x_k)^{2l}} \quad (\text{B.86})$$

for all $k > 0$ and for all $n = 1, \dots, \ell_k$. Furthermore, we recall that $x_k > 1$ (and thence $\zeta(x_k) < 1$) and we multiply by $\zeta(x_k)^{2n-1}$ to obtain

$$0 < v_n(x_k)\zeta(x_k)^n < \frac{1}{\zeta(x_k)^{-1} - \zeta(x_k)} \leq C \quad (\text{B.87})$$

for all $k > 0$ and for all $n = 1, \dots, \ell_k$. The last inequality is obtained by observing that $x_k \geq x_1 > 1$ implies $\zeta(x_k) \leq \zeta(x_1) < 1$ ($\zeta(x)$ is monotonically decreasing). At this point, using this bound in (B.84), we get

$$f_m(x_k) > 1 - C \sum_{n=m+1}^{\ell_k} (s_{n+1} - s_{n-1}) \quad (\text{B.88})$$

for all $m > 0$ and $k > m$. We can now send k to infinity: since $\ell_k \geq k$, we have that $\lim_{k \rightarrow \infty} \ell_k = \infty$. Then, recalling that $\lim_{k \rightarrow \infty} x_k = x_*$ and that $f_m(x)$ is a continuous function of x , we arrive at

$$f_m(x_*) \geq 1 - C \sum_{n=m+1}^{\infty} (s_{n+1} - s_{n-1}) \quad (\text{B.89})$$

for all $m > 0$. Sending m to infinity, we finally obtain the result $f(x_*) \geq 1$.

Statement (v) Using the result of the previous statement, namely that $x_* > 1 \implies f(x_*) = 1$, we rewrite (B.85) for $x = x_*$

$$\frac{v_n(x_*)}{\zeta(x_*)^{n-1}} = \sum_{l=0}^{n-1} \frac{2x_o \sum_{k=l+1}^{\infty} (s_{k+1} - s_{k-1}) v_k(x_*) \zeta(x_*)^k}{\zeta(x_*)^{2l}} \quad (\text{B.90})$$

for all $n > 0$. Using the same scheme leading to (B.87), for $x_* > 1$ we can see that $v_k(x_*)\zeta(x_*)^k \leq C$ for all $k > 0$. Then, from Lemma 1 it can be argued that $s_{k+1} - s_{k-1} \leq C\gamma^k$. Using this bound together with (5.59) in (B.90), we get for all $n > 0$

$$\frac{v_n(x_*)}{\zeta(x_*)^{n-1}} \leq C \sum_{l=0}^{n-1} \left[\frac{\zeta(x_o)}{\zeta(x_*)} \right]^{2l}. \quad (\text{B.91})$$

Since $\zeta(x)$ is monotonically decreasing, the condition $x_* < x_o$, which is always satisfied by virtue of statement (ii), entails that $\zeta(x_*) > \zeta(x_o)$. This is enough to prove the bound $v_n(x_*) \leq C\zeta(x_*)^n$.

B.2.5 Proof of Lemma 8

With reference to the Courant-type bound (5.48) (Lemma 2), we define

$$u_n \equiv \frac{v_n(x_*)}{\sqrt{\sum_{k=1}^N v_k(x_*)^2}} \quad n = 0, \dots, N+1, \quad (\text{B.92})$$

where $v_n(x_*)$ is defined according to Lemma 6. We note that (B.92) satisfies the normalization requirement of Lemma 2 ($\sum_{n=1}^N u_n^2 = 1$) and $u_n > 0$ for all $n > 0$, while $u_0 = 0$. Moreover, from Lemma 10, we easily obtain the bound

$$\sqrt{q_n q_{n+1}'} \geq \sqrt{q_0 q_0'} - C\omega(n+1) \quad n = 0, \dots, N. \quad (\text{B.93})$$

Using the latter result in (5.48) and recalling (5.35), we can write

$$\mu \leq 1 - \sum_{n=1}^N (s_{n+1} - s_{n-1}) u_n^2 - \frac{1}{x_\circ} \sum_{n=1}^{N-1} u_n u_{n+1} + C\omega \sum_{n=1}^{N-1} n u_n u_{n+1}. \quad (\text{B.94})$$

Now, using (B.92) together with (5.16), we get

$$2x_\circ (s_{n+1} - s_{n-1}) u_n + u_{n+1} + u_{n-1} = 2x_* u_n \quad n = 1, \dots, N. \quad (\text{B.95})$$

Multiplying both sides of this last equation by u_n and summing over $n = 1, \dots, N$, we arrive at

$$2x_\circ \sum_{n=1}^N (s_{n+1} - s_{n-1}) u_n^2 + 2 \sum_{n=1}^{N-1} u_n u_{n+1} = 2x_* - u_N u_{N+1}. \quad (\text{B.96})$$

We plug this result into (B.94) to obtain

$$\mu \leq 1 - \frac{x_*}{x_\circ} + C u_N u_{N+1} + C\omega \sum_{n=1}^{N-1} n u_n u_{n+1}. \quad (\text{B.97})$$

At this point, we observe that $\sum_{k=1}^N v_k(x_*)^2 \geq v_1(x_*)^2 = 1$. Thus, by statement (v) in Lemma 6, we have that $u_n \leq C\zeta(x_*)^n$ for all n and we can write

$$\mu \leq 1 - \frac{x_*}{x_\circ} + C\zeta(x_*)^{2N} + C\omega \sum_{n=1}^{N-1} n \zeta(x_*)^{2n}. \quad (\text{B.98})$$

To conclude the proof, we note that the hypothesis $x_* > 1$ implies $\zeta(x_*) < 1$, which ensures that the sum in (B.98) remains finite for $N \rightarrow \infty$.

B.3 Asymptotic bounds for the slowest relaxation rate (unbalanced case)

B.3.1 Upper bounds

Upper bound (i)

We adopt the same trial vector defined in (B.53) for the proof of Lemma 5. We choose M in such a way that, in the infinite size limit, one has $M \rightarrow \infty$, but $M/N \rightarrow 0$. In this way, the vector u has a large number, but a vanishing fraction, of nonzero components and is concentrated at the left boundary of the system. We rewrite the quadratic form (5.87) for the relaxation matrix in the large N limit

$$(u, Au) \approx 1 - \sum_{n=1}^N (s_{n+1} - s_{n-1}) u_n^2 - 2 \sum_{n=1}^{N-1} \sqrt{J_n} u_n u_{n+1}.$$

Since the difference $s_{n+1} - s_{n-1}$ goes to zero exponentially upon increasing n , we can neglect the second term in the right hand side. Considering the other sum, we recall that, by equation (5.77), the current can be regarded as a regular function of the variable $z \equiv n/(N+1)$. The definition of the trial vector together with the fact that $M/N \rightarrow 0$ entail that z vanishes for all n values included in the sum and the current is well approximated by its left boundary value, thus we can write

$$\sum_{n=1}^{N-1} \sqrt{J_n} u_n u_{n+1} = \sum_{n=1}^{M-2} \sqrt{J_n} u_n u_{n+1} \approx \sqrt{q_0 q_0'} \sum_{n=1}^{M-2} u_n u_{n+1}. \quad (\text{B.99})$$

Using (B.54) and taking the limit for $M \rightarrow \infty$, we obtain

$$(u, Au) \approx 1 - 2\sqrt{q_0 q_0'} \quad (\text{B.100})$$

and the following upper bound

$$\lambda_{min}^{(\infty)} \leq 1 - 2\sqrt{q_0 q_0'}. \quad (\text{B.101})$$

Upper bound (ii)

In this case we have to choose a trial vector being concentrated at the right boundary: using again (B.52) for y_n , we define

$$u_n \equiv \begin{cases} 0 & \text{if } n \leq N+1-M \\ y_{N+1-n} & \text{if } n \geq N+1-M \end{cases}, \quad (\text{B.102})$$

where $n = 1, \dots, N$. Now the local current is well approximated by its right boundary value, for all the n in the sum, thus we can write

$$\sum_{n=1}^{N-1} \sqrt{J_n} u_n u_{n+1} = \sum_{n=1}^{M-2} \sqrt{J_{N+1-n}} y_n y_{n+1} \approx \sqrt{\beta \beta'} \sum_{n=1}^{M-2} y_n y_{n+1}. \quad (\text{B.103})$$

We can again neglect the second term in the right hand side of (5.87). Using (B.54) and taking the limit for $M \rightarrow \infty$, we have

$$(u, Au) \approx 1 - 2\sqrt{\beta\beta'} \quad (\text{B.104})$$

and the upper bound for the slowest relaxation rate

$$\lambda_{\min}^{\infty} \leq 1 - 2\sqrt{\beta\beta'}. \quad (\text{B.105})$$

These two bounds do not depend on α and hold in principle with no restriction on this parameter, provided that $\alpha > q_0'$ in order to stay within the HD phase. However, they cannot be good bounds in the slow phase, where the slowest relaxation rate becomes smaller than its plateau value and depends on α .

Upper bound (iii)

Proceeding in analogy with the balanced case, we use the definition (B.92) for the vector u in the Courant-type bound (5.83). Using this in (5.16), we get

$$\frac{s_{n+1} - s_{n-1}}{\sqrt{q_0 q_0'}} = 2x_* u_n - u_{n+1} - u_{n-1}, \quad n = 1, 2, \dots \quad (\text{B.106})$$

Then, we multiply both sides by u_n and we sum over $n = 1, \dots, N$, taking into account that $u_0 = 0$

$$\sum_{n=1}^N \frac{s_{n+1} - s_{n-1}}{\sqrt{q_0 q_0'}} u_n^2 = 2x_* - 2 \sum_{n=1}^{N-1} u_n u_{n+1} - u_N u_{N+1}. \quad (\text{B.107})$$

We now recall the result of statement (v) in Lemma 6: if $x_* > 1$, the sequence $v_n(x_*)$ is upper bounded by $\zeta(x_*)^n$ up to a positive constant factor and $\zeta(x_*) < 1$. Using the fact that $\sum_{k=1}^N v_k(x_*)^2 \geq v_1(x_*)^2 = 1$, it follows that the same bound holds for u_n . As a consequence, the last term in the right hand side of (B.107) can be neglected. From (5.87), we get

$$(u, Au) \approx 1 - 2x_* \sqrt{q_0 q_0'} - 2 \sum_{n=1}^{N-1} \left(\sqrt{J_n} - \sqrt{q_0 q_0'} \right) u_n u_{n+1} \quad (\text{B.108})$$

We observe that the difference $\sqrt{J_n} - \sqrt{q_0 q_0'}$ is of order n/N . In the same hypothesis $x_* > 1$, the whole sum has asymptotic order $1/N$ in the infinite size limit. Thus we obtain

$$(u, Au) \approx 1 - 2x_* \sqrt{q_0 q_0'} \quad (\text{B.109})$$

and the upper bound

$$\lambda_{\min}^{\infty} \leq 1 - 2x_* \sqrt{q_0 q_0'} \quad (\text{B.110})$$

Overall upper bound

We now put the three bounds together: upper bound (iii) holds only for $x_* > 1$,

but upper bound (i) is its analogue for $x_* = 1$. Consequently, (B.110) is valid for all the possible values of x_* . Considering this last result along with the upper bound (ii), we obtain the overall bound

$$\lambda_{min}^{(\infty)} \leq 1 - 2 \max \left\{ x_* \sqrt{q_0 q_0'}, \sqrt{\beta \beta'} \right\}. \quad (\text{B.111})$$

B.3.2 Lower bounds

We follow the strategy developed in the proof of Lemma 3 (*Gershgorin type bound*). We take m as an index where the maximum of $\{|u_1|/w_1, \dots, |u_N|/w_N\}$ is reached and then normalize the vector u by u_m/w_m . We can write

$$\lambda_{min}^{(N)} = \frac{(Au)_m}{u_m} = a_m - \sqrt{J_m} \frac{u_{m+1}}{u_m} - \sqrt{J_{m-1}} \frac{u_{m-1}}{u_m}. \quad (\text{B.112})$$

Using the property $u_m = w_m > 0$ and $u_{m\pm 1} \leq w_{m\pm 1}$, we obtain the bound

$$\lambda_{min}^{(N)} \geq a_m - \sqrt{J_m} \frac{w_{m+1}}{w_m} - \sqrt{J_{m-1}} \frac{w_{m-1}}{w_m}. \quad (\text{B.113})$$

Now, since it is not possible to guess the proper index m , we have to choose the worst case

$$\lambda_{min}^{(N)} \geq \min_{n=1}^N \left\{ a_n - \sqrt{J_n} \frac{w_{n+1}}{w_n} - \sqrt{J_{n-1}} \frac{w_{n-1}}{w_n} \right\} \quad (\text{B.114})$$

We are interested in the infinite size limit, thus we can make some simplifications: we can use the approximate form (5.86) for the diagonal term a_n

$$a_n \approx 1 - (s_{n+1} - s_{n-1}),$$

then we can replace J_{n-1} with J_n , using the argument that the local current is approximately a regular function of n/N . Defining

$$\Delta_n \equiv s_{n+1} - s_{n-1} + \sqrt{J_n} \frac{w_{n+1} + w_{n-1}}{w_n} \quad n = 1, \dots, N, \quad (\text{B.115})$$

we have

$$\lambda_{min}^{(N)} \gtrsim 1 - \max_{n=1}^N \Delta_n. \quad (\text{B.116})$$

We have used the symbol \gtrsim , because the left hand side can be smaller than the right hand side, but at most by an amount vanishing in the $N \rightarrow \infty$ limit.

To apply this bound in the HD phase, we can delineate three different cases of increasing complexity.

Case $\alpha > q_0$

By (5.72) and (5.73), we see that the sequence s_n is non-increasing, thus

$s_{n+1} - s_{n-1} \leq 0$. Choosing w_n equal to a constant (which leads to the Gershgorin theorem), we get

$$\Delta_n \leq 2\sqrt{J_n} \quad n = 1, \dots, N. \quad (\text{B.117})$$

We send N to infinity, using the approximation (5.77) for the local current, which implies that its maximum value can be either q_0q_0' or $\beta\beta'$. We get

$$\lambda_{min}^{(\infty)} \geq 1 - 2 \max \left\{ \sqrt{q_0q_0'}, \sqrt{\beta\beta'} \right\}. \quad (\text{B.118})$$

We compare this result with the upper bound (B.111): taking into account that $x_* = 1$ in this range of α values, we can conclude that the bound is tight and can be written as an equality.

Case $\alpha_c \leq \alpha < q_0$

For this case we make the choice

$$w_n = v_n(x_*) \quad n = 0, 1, 2, \dots, \quad (\text{B.119})$$

which is legitimate, because $v_n(x) > 0, \forall n > 0$ for $x \geq x_*$. From now on we use v_n as a shorthand for $v_n(x_*)$, from (B.115) we get

$$\Delta_n = s_{n+1} - s_{n-1} + \sqrt{J_n} \frac{v_{n+1} + v_{n-1}}{v_n} \quad n = 1, \dots, N. \quad (\text{B.120})$$

We express the difference $s_{n+1} - s_{n-1}$ by (5.16)

$$s_{n+1} - s_{n-1} = \sqrt{q_0q_0'} \left[2x_* - \frac{v_{n+1} - v_{n-1}}{v_n} \right] \quad n = 1, 2, \dots \quad (\text{B.121})$$

Plugging this result into (B.120), we obtain

$$\Delta_n = 2x_*\sqrt{q_0q_0'} + \left(\sqrt{J_n} - \sqrt{q_0q_0'} \right) \frac{v_{n+1} + v_{n-1}}{v_n} \quad n = 1, \dots, N. \quad (\text{B.122})$$

For $\alpha < q_0$, we have that $s_{n+1} - s_{n-1} > 0$. Thus, from (B.121) it must be that

$$\frac{v_{n+1} + v_{n-1}}{v_n} < 2x_* \quad n = 1, 2, \dots \quad (\text{B.123})$$

If $\sqrt{J_n} \geq \sqrt{q_0q_0'}$, then $\Delta_n \leq 2x_*\sqrt{J_n}$. Otherwise, if $\sqrt{J_n} < \sqrt{q_0q_0'}$, by (B.122) it follows that $2x_*\sqrt{q_0q_0'} + 2x_* \left(\sqrt{J_n} - \sqrt{q_0q_0'} \right) < 2x_*\sqrt{q_0q_0'}$. Thence, we obtain

$$\Delta_n \leq 2x_* \max \left\{ \sqrt{q_0q_0'}, \sqrt{J_n} \right\} \quad n = 1, \dots, N. \quad (\text{B.124})$$

Using the same argument made above for J_n in the infinite size limit, we obtain

$$\lambda_{min}^{(\infty)} \geq 1 - 2x_* \max \left\{ \sqrt{q_0q_0'}, \sqrt{\beta\beta'} \right\} \quad (\text{B.125})$$

We compare the latter bound with (B.111) and observe that it is again tight, because we still have $x_* = 1$ for $\alpha \geq \alpha_c$.

In particular we note that, for $\beta \leq l'$, these bounds are tight for all $q_0' < \alpha < q_0$. Within the low beta region, the current profile is non-increasing, thus $q_0 q_0' \geq \beta \beta'$. Consequently, we can discard the second term in the max and obtain equality (5.80).

Case $\alpha < \alpha_c$

We recall that, by definition, $x_* > 1$ for $\alpha < \alpha_c$. For this case, it is possible to prove this useful preliminary result:

$$\lim_{n \rightarrow \infty} \frac{v_{n+1}(x_*)}{v_n(x_*)} = \zeta(x_*) < 1, \quad (\text{B.126})$$

where the last inequality is directly obtained from (5.13). We postpone the proof of this statement to section B.3.3. We choose the sequence w_n as follows

$$w_n \equiv \begin{cases} v_n(x_*) & \text{if } n \leq L \\ v_L(x_*) & \text{if } n \geq M \\ \phi_n v_L(x_*) + \phi_n' v_n(x_*) & \text{if } L \leq n \leq M \end{cases} \quad n = 0, 1, 2, \dots, \quad (\text{B.127})$$

with L and M positive integers such that $L < M < N$ and

$$\phi_n \equiv \frac{n - L}{M - L}. \quad (\text{B.128})$$

One can observe that this definition is a convex linear combination of the previous trial vectors, which are either constant or equal to $v_n(x_*)$. We require that L and M depend on the system size N in such a way that, for $N \rightarrow \infty$, they both tend to infinity, but $L/M \rightarrow 0$ and $M/N \rightarrow 0$. According to (B.115) and (B.116), we see that (B.127) suggests to split the maximum operation over three subsets, namely

$$\max_{n=1}^N \Delta_n = \max \left\{ \max_{n=1}^L \Delta_n, \max_{n=M}^N \Delta_n, \max_{n=L+1}^{M-1} \Delta_n \right\}. \quad (\text{B.129})$$

We now discuss each subset separately.

- (i) For $n = 1, \dots, N$, we can make the approximation $J_n \approx q_0 q_0'$, due to the fact that $L/N \rightarrow 0$. Thus, from (B.115) we can write

$$\Delta_n \approx s_{n+1} - s_{n-1} + \sqrt{\vartheta \vartheta'} \frac{w_{n+1} + w_{n-1}}{w_n} \quad n = 1, \dots, L. \quad (\text{B.130})$$

By the definition (B.127), we have

$$\frac{w_{n+1} + w_{n-1}}{w_n} = \frac{v_{n+1} + v_{n-1}}{v_n} \quad n = 1, \dots, L - 1, \quad (\text{B.131})$$

$$\frac{w_{L+1} + w_{L-1}}{w_L} = \frac{v_{L+1} + v_{L-1}}{v_L} + \frac{1 - v_{L+1}/v_L}{M - L}. \quad (\text{B.132})$$

We send L to infinity using the result (B.126): since v_{L+1}/v_L tends to a finite quantity, whereas $M - L \rightarrow \infty$, the second term on the right hand side of (B.132) can be neglected and (B.131) can be used also for $n = L$. Thence, by (B.130) and (B.121), we obtain

$$\Delta_n \approx 2x_* \sqrt{\vartheta \vartheta'} \quad n = 1, \dots, L. \quad (\text{B.133})$$

- (ii) For $n = M, \dots, N$, the exponentially decaying term $s_{n+1} - s_{n-1}$ can be neglected using the fact that $M \rightarrow \infty$. From (B.115) we can write

$$\Delta_n \approx \sqrt{J_n} \frac{w_{n+1} + w_{n-1}}{w_n} \quad n = M, \dots, N. \quad (\text{B.134})$$

Then, according to (B.127), we have

$$\frac{w_{n+1} + w_{n-1}}{w_n} = 2 \quad n = M + 1, \dots, N, \quad (\text{B.135})$$

$$\frac{w_{M+1} + w_{M-1}}{w_M} = 2 - \frac{1 - v_{M-1}/v_L}{M - L}. \quad (\text{B.136})$$

In our assumption we have $L, M \rightarrow \infty$ and $L/M \rightarrow 0$, thus, using the result (B.126), we realize that $v_{M-1}/v_L \rightarrow 0$. The denominator $M - L$ diverges, so that we can neglect the last term in (B.136) and the previous equation (B.135) can be adopted for $n = M$ as well. Consequently, from (B.134) we get

$$\Delta_n \approx 2\sqrt{J_n} \quad n = M, \dots, N. \quad (\text{B.137})$$

We express J_n by (5.77), keeping in mind that $M/N \rightarrow 0$, to get

$$\max_{n=M}^N \Delta_n \approx 2 \max \left\{ \sqrt{\vartheta \vartheta'}, \sqrt{\beta \beta'} \right\}. \quad (\text{B.138})$$

- (iii) For $n = L + 1, \dots, M - 1$, we can make the approximation $J_n \approx \vartheta \vartheta'$ (left-boundary current), thanks to the fact that $M/N \rightarrow 0$. At the same time, taking the limit $L \rightarrow \infty$, we can neglect the term $s_{n+1} - s_{n-1}$, which decays exponentially. Thus, from (B.115) we get

$$\Delta_n \approx \sqrt{\vartheta \vartheta'} \frac{w_{n+1} + w_{n-1}}{w_n} \quad n = L + 1, \dots, M - 1. \quad (\text{B.139})$$

Using (B.127), we have for all n in the range of interest

$$\frac{w_{n+1} + w_{n-1}}{w_n} = \frac{2\phi_n v_L + \phi_n'(v_{n+1} + v_{n-1}) + \frac{v_{n-1} - v_{n+1}}{M - L}}{\phi_n v_L + \phi_n' v_n}. \quad (\text{B.140})$$

First of all we note that all the variables in the latter equation are positive, then we consider the three terms in the numerator on the right hand side. For the first one, we use the property $x_* > 1$ to write $2\phi_n v_L < 2x_* \phi_n v_L$. As regards the second term, the inequality (B.123) implies $\phi_n'(v_{n+1} + v_{n-1}) < 2x_* \phi_n' v_n$. For the third term, we use (B.123) along with $v_{n+1} > 0$ and we easily obtain that $v_{n-1} - v_{n+1} < 2x_* v_n$. Then, the property (B.126), i.e. the fact that v_n is eventually decreasing, allows us to write $v_n = \phi_n v_n + \phi_n' v_n < \phi_n v_L + \phi_n' v_n$ for all $n > L$. Using these bounds together, we obtain

$$\frac{w_{n+1} + w_{n-1}}{w_n} < 2x_* + \frac{2x_*}{M - L} \quad n = L + 1, \dots, M - 1. \quad (\text{B.141})$$

We plug this inequality into (B.139) and we finally get

$$\Delta_n \lesssim 2x_* \sqrt{\vartheta \vartheta'} \quad n = L + 1, \dots, M - 1. \quad (\text{B.142})$$

At this point we put together (B.133), (B.138), (B.142) into (B.129), and thence into (B.116). In the infinite size limit we obtain

$$\lambda_{\min}^{(\infty)} \geq 1 - 2 \max \left\{ x_* \sqrt{\vartheta \vartheta'}, \sqrt{\beta \beta'} \right\}. \quad (\text{B.143})$$

Comparing this last inequality with (B.111), we conclude that the bound is tight.

B.3.3 Proof of statement (B.126)

We define the sequence

$$d_n \equiv \frac{v_{n+1}(x_*)}{v_n(x_*)} \quad n = 1, 2, \dots. \quad (\text{B.144})$$

The definition is valid because we know that $v_n(x_*)$ is strictly positive for all $n > 0$ and this property entails that d_n is itself strictly positive for all n . From (5.16) we have

$$d_1 = 2x_* - \frac{s_2 - s_0}{\sqrt{\vartheta \vartheta'}}, \quad (\text{B.145})$$

$$d_{n+1} = 2x_* - \frac{s_{n+2} - s_n}{\sqrt{\vartheta \vartheta'}} - \frac{1}{d_n} \quad n = 1, 2, \dots. \quad (\text{B.146})$$

We can reduce the problem to showing that, given two arbitrarily small positive real numbers ε and δ , the inequalities

$$\zeta(x_*) - \varepsilon < d_n < \zeta(x_* - \delta) \quad (\text{B.147})$$

hold at least for n large enough. After that, the proof is easily concluded by sending n to infinity and taking into account the continuity of $\zeta(x)$. In the following we prove separately the lower and upper inequalities.

Lower-bound Let us consider any positive real number ε such that

$$\varepsilon < \zeta(x_*). \quad (\text{B.148})$$

This condition can be satisfied because $\zeta(x_*) > 0$ by construction. In the current hypotheses, we know that s_n is a monotonically increasing sequence, thus

$$\frac{s_{n+2} - s_n}{\sqrt{\vartheta\vartheta'}} > 0 \quad (\text{B.149})$$

for all $n (\geq 0)$. From (B.146) we then have

$$d_{n+1} < 2x_* - \frac{1}{d_n}, \quad (\text{B.150})$$

still for all $n (\geq 1)$. It is also possible to verify that the following inequality,

$$2x_* - \frac{1}{d} \leq \zeta(x_*) + \frac{d - \zeta(x_*)}{\zeta(x_*)^2}. \quad (\text{B.151})$$

holds for any positive real number d . Then, since d_n is positive by construction, from (B.150) and (B.151) we get

$$d_{n+1} < \zeta(x_*) + \frac{d_n - \zeta(x_*)}{\zeta(x_*)^2}. \quad (\text{B.152})$$

Reasoning by contradiction, let us now assume that there exists some $n (\geq 1)$ such that $d_n \leq \zeta(x_*) - \varepsilon$, where d_n is positive because of (B.148). Then, by a repeated use of (B.152) we could argue that

$$d_{n+k} < \zeta(x_*) - \frac{\varepsilon}{\zeta(x_*)^{2k}} \quad (\text{B.153})$$

for any positive integer k . Therefore $d_{n+k} < 0$ for some k , which is a contradiction. We can thus conclude that for any positive ε satisfying (B.148) (and hence in particular for ε arbitrarily close to 0), the inequality

$$d_n > \zeta(x_*) - \varepsilon \quad (\text{B.154})$$

must hold for all $n (\geq 1)$.

Upper-bound We first prove the weaker bound that d_n must be eventually smaller than 1. We know that the term $s_{n+2} - s_n$ decays exponentially for $n \rightarrow \infty$. Consequently, there exists some integer m such that

$$\frac{s_{n+2} - s_n}{\sqrt{\vartheta\vartheta'}} < 2(x_* - 1) \quad (\text{B.155})$$

for all $n \geq m$. Now, if by contradiction we had $d_n \geq 1$ for some $n \geq m$, then (B.146) with (B.155) would imply $d_{n+1} > 1$, and therefore by induction d_n eventually larger than 1. This is clearly in contradiction with the bound $v_n(x_*) \leq C\zeta(x_*)^n$.

Let us now consider any positive real number δ such that

$$\delta < x_* - 1, \tag{B.156}$$

where the latter condition can be satisfied because $x_* > 1$ by hypothesis. Using again the fact that $s_{n+2} - s_n$ decays exponentially for $n \rightarrow \infty$, we can argue that there exists some integer m (depending on δ) such that

$$\frac{s_{n+2} - s_n}{\sqrt{\vartheta\vartheta'}} < \delta \tag{B.157}$$

for all $n \geq m$. From (B.146) we then have

$$d_{n+1} > 2x_* - \frac{1}{d_n} - \delta, \tag{B.158}$$

still for all $n \geq m$. It is also possible to verify that, given that d is a positive real number, the inequality

$$2x_* - \frac{1}{d} \geq d + 2\delta \tag{B.159}$$

holds if and only if

$$\zeta(x_* - \delta) \leq d \leq \frac{1}{\zeta(x_* - \delta)}, \tag{B.160}$$

where (B.156) ensures that $\zeta(x_* - \delta)$ is real (positive and less than 1). Then, since d_n is positive by construction, from (B.158) and the equivalence between (B.159) and (B.160) we have that, given any $n \geq m$, the inequality

$$d_{n+1} > d_n + \delta \tag{B.161}$$

is verified if and only if $d_n \geq \zeta(x_* - \delta)$. We stress the fact that the other condition $d_n \leq 1/\zeta(x_* - \delta)$ required by (B.160) is inherently satisfied because $d_n < 1$ for all $n \geq m$: indeed the definition (B.157) together with (B.156) satisfy (B.155).

Reasoning again by contradiction, let us now assume that there exists some $n \geq m$ such that $d_n \geq \zeta(x_* - \delta)$. As previously argued, this would be sufficient for d_n to verify (B.161), and therefore by induction $d_{n+k} > 1$ for some positive integer k , which is clearly a contradiction. We can thus conclude that for any positive δ satisfying (B.156) (and hence in particular for δ arbitrarily close to 0), the inequality

$$d_n < \zeta(x_* - \delta) \tag{B.162}$$

is verified for large enough n .

Bibliography

- ¹A. Pelizzola and M. Pretti, “Cluster approximations for the TASEP: stationary state and dynamical transition”, *Eur. Phys. J. B* **90**, 183 (2017).
- ²J. de Gier and F. H. L. Essler, “Slowest relaxation mode of the partially asymmetric exclusion process with open boundaries”, *J. Phys. A: Math. Theor.* **41**, 485002 (2008).
- ³M. Dudzinski and G. M. Schütz, “Relaxation spectrum of the asymmetric exclusion process with open boundaries”, *J. Phys. A: Math. Gen.* **33**, 8351 (2000).
- ⁴A. Proeme, R. A. Blythe, and M. R. Evans, “Dynamical transition in the open-boundary totally asymmetric exclusion process”, *J. Phys. A: Math. Theor.* **44**, 035003 (2010).
- ⁵B. Derrida, E. Domany, and D. Mukamel, “An exact solution of a one-dimensional asymmetric exclusion model with open boundaries”, *J. Stat. Phys.* **69**, 667 (1992).
- ⁶G. M. Schütz and E. Domany, “Phase transitions in an exactly soluble one-dimensional exclusion process”, *J. Stat. Phys.* **72**, 277 (1993).
- ⁷B. Derrida, M. Evans, V. Hakim, and V. Pasquier, “Exact solution of a 1D asymmetric exclusion model using a matrix formulation”, *J. Phys. A: Math. Gen.* **26**, 1493 (1999).
- ⁸B. Derrida, “An exactly soluble non-equilibrium system: The asymmetric simple exclusion process”, *Phys. Rep.* **301**, 65 (1998).
- ⁹J. de Gier and F. H. L. Essler, “Bethe Ansatz Solution of the Asymmetric Exclusion Process with Open Boundaries”, *Phys. Rev. Lett.* **95**, 240601 (2005).
- ¹⁰T. Chou, M. K., and Z. R. K. P., “An exactly soluble non-equilibrium system: The asymmetric simple exclusion process”, *Rep. Prog. Phys.* **74**, 116601 (2011).
- ¹¹A. Schadschneider, D. Chowdhury, and K. Nishinari, *Stochastic transport in complex systems - from molecules to vehicles* (Elsevier, Oxford, 2011).
- ¹²C. T. MacDonald, J. H. Gibbs, and A. C. Pipkin, “Kinetics of biopolymerization on nucleic acid templates”, *Biopolymers* **6**, 1 (1968).
- ¹³J. de Gier and F. H. L. Essler, “Exact spectral gaps of the asymmetric exclusion process with open boundaries”, *J. Stat. Mech.*, P12011 (2006).

- ¹⁴N. van Kampen, *Stochastic Processes in Physics and Chemistry* (Elsevier, Amsterdam, 2007).
- ¹⁵A. Parmeggiani, T. Franosch, and E. Frey, “Totally asymmetric simple exclusion process with Langmuir kinetics”, *Phys. Rev. E* **70**, 046101 (2004).
- ¹⁶R. D. Willmann, G. M. Schütz, and D. Challet, “Exact Hurst exponent and crossover behavior in a limit order market model”, *Physica A* **316**, 430 (2002).
- ¹⁷A. Parmeggiani, T. Franosch, and E. Frey, “Phase Coexistence in Driven One-Dimensional Transport”, *Phys. Rev. Lett.* **90**, 086601 (2003).
- ¹⁸T. Antal and G. M. Schütz, “Asymmetric exclusion process with next-nearest-neighbor interaction: Some comments on traffic flow and a nonequilibrium reentrance transition”, *Phys. Rev. E* **62**, 83 (2000).
- ¹⁹S. Katz, J. Lebowitz, and H. Spohn, “Nonequilibrium steady states of stochastic lattice gas models of fast ionic conductors”, *J. Stat. Phys.* **34**, 497 (1984).
- ²⁰G. M. Schütz, *Phase Transitions and Critical Phenomena*, edited by C. Domb and J. L. Lebowitz (Academic Press, San Diego, 2001).
- ²¹L. Neubert, L. Santen, A. Schadschneider, and M. Schreckenberg, “Single-vehicle data of highway traffic: A statistical analysis”, *Phys. Rev. E* **60**, 6480 (1999).
- ²²A. Pelizzola, M. Pretti, and F. Puccioni, “Dynamical Transitions in a One-Dimensional Katz–Lebowitz–Spohn Model”, *Entropy* **21** (2019).
- ²³M. Dierl, M. Einax, and P. Maass, “One-dimensional transport of interacting particles: Currents, density profiles, phase diagrams, and symmetries”, *Phys. Rev. E* **87**, 062126 (2013).
- ²⁴A. Pelizzola, “Cluster variation method in statistical physics and probabilistic graphical models”, *J. Phys. A: Math. Gen.* **38**, R309 (2005).
- ²⁵D. ben-Avraham and J. Köhler, “Mean-field (n, m)-cluster approximation for lattice models”, *Phys. Rev. A* **45**, 8358 (1992).
- ²⁶D. Botto, A. Pelizzola, M. Pretti, and M. Zamparo, “Dynamical transition in the TASEP with Langmuir kinetics: mean-field theory”, *J. Phys. A: Math. Theor.* **52**, 045001 (2018).
- ²⁷R. Corless, G. Gonnet, D. Hare, D. Jeffrey, and D. Knuth, “On the LambertW function”, *Adv. Comput. Math.* **5**, 329 (1996).
- ²⁸Z. Nagy, C. Appert, and L. Santen, “Relaxation times in the ASEP model using a DMRG method”, *J. Stat. Phys.* **109**, 623 (2002).
- ²⁹D. T. Gillespie, “Exact Stochastic Simulation Of Coupled Chemical-Reactions”, *J. Phys. Chem.* **81**, 2340 (1977).
- ³⁰R. B. Lehoucq and D. C. Sorensen, “Deflation Techniques For An Implicitly Re-Started Arnoldi Iteration”, *SIAM J. Matrix Anal. Appl.* **17**, 789 (1996).

- ³¹ARPACK webpage, <https://www.caam.rice.edu/software/ARPACK/>, last accessed on 2019-06-03.
- ³²U. Bilstein and B. Wehefritz, “Spectra of non-Hermitian quantum spin chains describing boundary induced phase transitions”, *J. Phys. A: Math. Gen.* **30**, 4925 (1997).
- ³³W. H. Press, S. A. Teukolsky, W. T. Vetterling, and B. P. Flannery, *Numerical Recipes* (Cambridge University Press, New York, 2007).
- ³⁴R. Bulirsch and J. Stöer, “Fehlerabschätzungen und extrapolation mit rationalen funktionen bei verfahren vom Richardson-typus”, *Num. Math.* **6**, 413 (1964).
- ³⁵R. Bulirsch and J. Stöer, *Introduction to Numerical Analysis* (3rd ed, Springer, New York, 2002).
- ³⁶M. Henkel and G. M. Schütz, “Finite-lattice extrapolation algorithms”, *J. Phys. A: Math. Gen.* **21**, 2617 (1988).
- ³⁷R. P. Agarwal, *Difference equations and inequalities: theory, methods and applications* (CRC Press, Boca Raton, 2000).
- ³⁸D. Botto, A. Pelizzola, and M. Pretti, “Dynamical transitions in a driven diffusive model with interactions”, *Europhys. Lett.* **124**, 50004 (2018).
- ³⁹A. K. Gupta and I. Dhiman, “Asymmetric coupling in two-lane simple exclusion processes with Langmuir kinetics: Phase diagrams and boundary layers”, *Phys. Rev. E* **89**, 022131 (2014).
- ⁴⁰I. Dhiman and A. K. Gupta, “Effect of coupling strength on a two-lane partially asymmetric coupled totally asymmetric simple exclusion process with Langmuir kinetics”, *Phys. Rev. E* **90**, 012114 (2014).
- ⁴¹J. Howard and R. Clark, “Mechanics of motor proteins and the cytoskeleton”, *Appl. Mech. Rev.* **55**, 39 (2002).
- ⁴²R. K. P. Zia, J. J. Dong, and B. Schmittmann, “Modeling Translation in Protein Synthesis with TASEP: A Tutorial and Recent Developments”, *J. Stat. Phys.* **144**, 405 (2011).
- ⁴³M. Ha and M. den Nijs, “Macroscopic car condensation in a parking garage”, *Phys. Rev. E* **66**, 036118 (2002).
- ⁴⁴S. L. Narasimhan and A. Baumgaertner, “TASEP of interacting particles of arbitrary size”, *J. Phys. A: Math. Theor.* **50**, 405001 (2017).
- ⁴⁵T. Midha, A. B. Kolomeisky, and A. K. Gupta, “Effect of interactions for one-dimensional asymmetric exclusion processes under periodic and bath-adapted coupling environment”, *J. Stat. Mech.*, P043205 (2018).
- ⁴⁶T. Midha, L. V. F. Gomes, A. B. Kolomeisky, and A. K. Gupta, “Theoretical investigations of asymmetric simple exclusion processes for interacting oligomers”, *J. Stat. Mech.*, P053209 (2018).

- ⁴⁷F. Alcaraz and M. Lazo, “The Exact Solution of the Asymmetric Exclusion Problem with Particles of Arbitrary Size: Matrix Product Ansatz”, *Braz. J. Phys.* **33**, 533 (2003).
- ⁴⁸J. J. Dong, R. K. P. Zia, and B. Schmittmann, “Understanding the edge effect in TASEP with mean-field theoretic approaches”, *J. Phys. A: Math. Theor* **42**, 015002 (2009).
- ⁴⁹M. Foulaadvand, A. Kolomeisky, and H. Teymour, “Asymmetric exclusion processes with disorder: Effect of correlations”, *Phys. Rev. E* **78**, 061116 (2008).
- ⁵⁰B. Waclaw, J. Cholewa-Waclaw, and P. Greulich, “Totally asymmetric exclusion process with site-wise dynamic disorder”, *J. Phys. A: Math. Theor.* **52**, 065002 (2019).
- ⁵¹P. Greulich and A. Schadschneider, “Single-bottleneck approximation for driven lattice gases with disorder and open boundary conditions”, *J. Stat. Mech.*, P04009 (2008).

This Ph.D. thesis has been typeset by means of the T_EX-system facilities. The typesetting engine was pdfL^AT_EX. The document class was `toptesi`, by Claudio Beccari, with option `tipotesi=scudo`. This class is available in every up-to-date and complete T_EX-system installation.